Study of the $B_s^0 \to (J/\psi)\phi \to \mu^+\mu^- K^+ K^-$ Decay with the CMS Detector at LHC

Dissertation

zur

Erlangung der naturwissenschaftlichen Doktorwürde (Dr. sc. nat.)

vorgelegt der

Mathematisch-naturwissenschaftlichen Fakultät

der

Universität Zürich

von

Kirill Prokofiev

aus

Rußland

Promotionskomitee

Prof. Dr. C. Amsler (Vorsitz)
Prof. Dr. U. Straumann
Dr. Th. Speer

Zürich, 2006

Zusammenfassung

Der Zerfall $B_s^0 \to (J/\psi)\phi \to \mu^+\mu^- K^+K^-$ wird als goldener Übergang bezeichnet, hier können die Teilchen-Antiteilchen Oszillationen im $B_s^0 - \bar{B}_s^0$ System untersucht, die Lebensdauern der leichten und schweren Masseneigenzustände des B_s^0 Mesons gemessen und der Wolfenstein-Parameter η, welcher für die CP-Verletzung im Standardmodell zuständig ist, extrahiert werden. Insbesondere letzterer ist wichtig, da er die Spitze des Unitaritätsdreiecks eingrenzt; eine Abweichung von anderen Messungen wäre ein Hinweis auf neue Physik.

In dieser Arbeit werden die Möglichkeiten für die Rekonstruktion und Selektion von $B_s^0 \to (J/\psi)\phi \to \mu^+\mu^- K^+K^-$ Ereignissen mit dem CMS-Detektor erörtert, wobei ein Schwerpunkt auf die Rekonstruktions- und Fit-Techniken der on- und offline Rekonstruktion dieser Events gelegt wird. Der Einfluss verschiedener Algorithmen auf die Genauigkeit der Ergebnisse wird untersucht.

Insbesondere wurde ein Wechselwirkungspunkt-Rekonstruktionsalgorithmus, welcher auf dem Kalman-Filter basiert, entwickelt und in den Rahmen der globalen Software des CMS-Experiments eingebettet. Aufgrund seiner hohen Leistung ist dieser Algorithmus sowohl für die online wie auch die offline Rekonstruktion des Wechselwirkungspunktes geeignet. Desweiteren wurde eine Bibliothek entwickelt und in den Rahmen der globalen Software des CMS-Experiments eingebettet, welche die Rekonstruktion von Zerfallsreihen und die dadurch eingeschränkte Anpassung von Spuren und Wechselwirkungspunkten ermöglicht. Durch diese kinematischen Einschränkungen wurde die experimentelle Massenauflösung des B_s^0-Mesons von 34 MeV auf 14 MeV verbessert.

Für den High Level Trigger wurde eine Strategie entwickelt und implementiert, die es erlaubt, $B_s^0 \to (J/\psi)\phi \to \mu^+\mu^- K^+K^-$ Ereignisse online zu selektieren. Die Signal- bzw Hintergrundereignisrate des High Level Triggers wird schätzungsweise $(3.4 \pm 1.3) \cdot 10^{-2}$ Hz bzw. $(5.0 \pm 0.7) \cdot 10^{-2}$ Hz betragen. Für eine integrierte Luminosität von 30 fb^{-1} (dies entspricht den ersten Jahren Laufzeit des LHC) ergibt sich eine Ausbeute des Triggers von $(5.1 \pm 1.9) \cdot 10^5$ Ereignissen.

Es wurde eine offline Selektion der $B_s^0 \to (J/\psi)\phi \to \mu^+\mu^- K^+K^-$ Ereignisse entwickelt und implemeniert. Die Auflösung der Zerfallslänge des B_s^0-Mesons wurde zu etwa 30 fb^{-1} abgeschätzt, was eine direkte Messung der $B_s^0 - \bar{B}_s^0$ Oszillationen ermöglichen würde, falls die tatsächliche Oszillationsfrequenz nahe der momentanen unteren Grenze von 14.4 ps^{-1} liegt. Es wurden die kombinierten Selektionseffizienzen für Signal- und Untergrundereignisse (High Level Trigger und offline Selektion) bestimmt, wobei sich eine Signalausbeute von $242'000 \pm 87'400$ Ereignissen bei einer integrierten Luminosität von 30 fb^{-1} für die Kombination von High Level Trigger und offline Selektion ergab.

Letztendlich wurde noch untersucht, ob es möglich ist, die Lebensdauer der leichten und schweren Masseneigenzustände des B_s^0-Mesons aus der Verteilung der Lebensdauer zu bestimmen, wobei sich herausstellte, dass dies mit dieser Methode nicht möglich ist. Jedoch könnten die Lebensdauern durch eine Untersuchung der Winkelverteilung der Teilchen im Endzustand bestimmt werden.

Abstract

The decay $B_s^0 \to (J/\psi)\phi \to \mu^+\mu^- K^+K^-$ is a *golden* transition which allows to study particle-antiparticle oscillation in the $B_s^0 - \bar{B}_s^0$ system, to measure the lifetimes of heavy and light mass eigenstates of the B_s^0 meson and to extract the Wolfenstein parameter η which is responsible for CP violation in the Standard Model. The latter measurement is indeed important, since it allows to constrain the apex of the unitarity triangle. Any discrepancy with other measurements may signal the presence of new physics.

In the current thesis the prospects for the reconstruction and selection of $B_s^0 \to (J/\psi)\ \phi \to \mu^+\mu^- K^+K^-$ events with the CMS detector are discussed. The emphasis is given to the reconstruction and fitting techniques suitable for online and offline reconstruction of these events. The influence of various reconstruction algorithms on the accuracy of the measurement is studied.

In particular, a vertex fitting algorithm based on the Kalman filter was developed and implemented in the framework of the CMS reconstruction software. With its high performance, this algorithm was found to be suitable for both online and offline reconstruction of vertices. Furthermore, a kinematic fitting and decay chain reconstruction library was also developed and implemented in the framework of CMS reconstruction software. This library allows the reconstruction of decay chains and the constrained refit of tracks and vertices. Due to the application of kinematic constraints, the experimental resolution on the mass of the B_s^0 meson improved from 34 MeV to approximately 14 MeV.

A High Level Trigger strategy, suitable for online selection of $B_s^0 \to (J/\psi)\phi \to \mu^+\mu^- K^+K^-$ events was developed and implemented. The rates of the High Level Trigger are estimated to be $(3.4 \pm 1.3) \cdot 10^{-2}$ Hz for the signal and $(5.0 \pm 0.7) \cdot 10^{-2}$ Hz for the background. The trigger event yield for 30 fb^{-1} (corresponding to first several years of the LHC operation) is estimated to be $(5.1 \pm 1.9) \cdot 10^5$.

The offline selection of $B_s^0 \to (J/\psi)\phi \to \mu^+\mu^- K^+K^-$ events was developed and implemented. The resolutions on the proper decay length of the B_s^0 meson was estimated to be around 30 fb^{-1}. This resolution would allow a direct observation of the $B_s^0 - \bar{B}_s^0$ oscillations if the actual oscillation frequency is close to the present lower limit (14.4 ps^{-1}). The combined (High level Trigger + offline selection) selection efficiencies for signal and background event were calculated. The signal event yield for combined High Level Trigger and offline selections for 30 fb^{-1} was estimated to be $242'000 \pm 87'400$.

Finally, the possibility of measuring the proper lifetimes of heavy and light mass eigenstates of the B_s^0 meson from the distribution of its lifetime was investigated. It was concluded that these two lifetimes can not be measured with this method, however they can be extracted from the angular distributions of the final state particles.

Acknowledgments

I would like to express my deep gratitude to my colleagues who helped and supported me during the four years of my PhD. First of all, I would like to thank my supervisors Prof. Dr. Claude Amsler and Dr. Thomas Speer, who were guided and advised me during four years of my PhD. They have introduced me to the CMS Pixel and Silicon Strip Tracker hardware and software communities, which have defined greatly the direction of my current and future research.

Claude constantly supported me in all my scientific activities, providing wise advise on the most critical points of my research. I am especially grateful to him for introducing me to the Silicon Pixel test beam team, which allowed me to gain some hardware experience.

I would like to thank Thomas for guiding, correcting and encouraging me at all stages of my PhD. I am extremely thankful to him for teaching me C++, reconstruction and fitting techniques and introducing me to the field of b-physics. Thomas possesses an outstanding knowledge and professional skills in these fields. This work would have never been possible without his help.

Further thanks go to my colleagues from HEPHY Vienna, Prof. Dr. Rudi Frühwirth and Wolfgang Waltenberger. Rudi, a world-known specialist in the reconstruction and fitting techniques, played undutifully a leading role in the development of the mathematical formalism for vertex reconstruction in CMS. His advise greatly helped me for the development of the Kalman Vertex Fitter, Kinematic fit and decay chain reconstruction library.

It happened that almost at the same time when I started to work under the supervision of Thomas Speer and Claude Amsler, Wolfgang Waltenberger started his PhD under the supervision of Rudi Frühwirth. I want to thank Wolfgang for a number of very helpful discussions we had during the time we were working together in the vertexing group and especially for developing the vertex fast simulation, the Vertex Gun.

I would also like to thank the leader of the CMS vertexing group, Dr. Pascal Vanlaer from ULB Bruxelles. Apart from the general leadership, Pascal is one of the main architects of the CMS vertex reconstruction framework. Working with him allowed me to learn the correct way of designing the reconstruction code.

I should also express my gratitude to all present and former members of the University of Zürich group at CERN, with whom I was working during these four years: Prof. Dr. Henk Pruys, Dr. Christian Regenfus, Dr. Vincenzo Chiochia, Dr. Ian Johnson, Dr. Peter Robmann, Dr. Andrei Dorokhov, Jacky Rochet, Cristoph

Hörmann, Yves Allkofer, Enver Alagoz, Dimitrios Tsirigkas and Lotte Wilke. Without their friendly and professional help, this work would have never been possible.

To my parents, my brother and
my most incredible girlfriend Polina.

Contents

Chapter 1

Physics motivation

1.1 Production of B_s^0 mesons at hadron colliders

The present and the coming generations of hadron colliders provide an excellent laboratory to study the physics of b-flavoured hadrons. The large production cross sections and high luminosities, achievable in hadron colliders allow them to compete with e^+e^- machines, despite the low branching fraction of $b\bar{b}$-pairs production in hadron collisions and low b-tagging efficiencies, caused by the large multiplicity of tracks (see Table 1.1). In addition, the present e^+e^- colliders at SLAC and KEK work at center-of-mass energies of the $\Upsilon(4S)(10.58\text{ GeV})$ resonance, where some of heavy b-flavoured hadrons heavier than $B^{\pm}$ or B_d^0 (such as B_s^0, Λ_b, etc) can not be produced.

These facts make the hadron colliders by far the largest source of the b-flavoured hadrons. After the launch of the Large Hadron Collider (LHC) at CERN, scheduled for 2007, this pp machine with center-of-mass energy of 14 TeV, and luminosities ranging from $2{\cdot}10^{33}\text{cm}^{-2}\text{s}^{-1}$ to $10^{34}\text{cm}^{-2}\text{s}^{-1}$ will become the worlds leading b-physics facility.

	B-factories	LEP	Tevatron	LHC
Prod. mode	$e^+e^- \to \Upsilon(4S) \to b\bar{b}$	$e^+e^- \to Z^0 \to b\bar{b}$	$p\bar{p} \to b\bar{b} + X$	$pp \to b\bar{b} + X$
CM energy	10.58 GeV	91.2 GeV	1.8 TeV	14 TeV
$\sigma(b\bar{b})$	1.25 nb	7.7 nb	$\sim 50\ \mu$b	$\sim 500\ \mu$b
$\sigma(b\bar{b})/\sigma_{tot}$	0.25	0.22	$\sim 6 \cdot 10^{-4}$	$\sim 2 \cdot 10^{-3}$

Table 1.1: The $b\bar{b}$-pairs production at LHC and other accelerators.

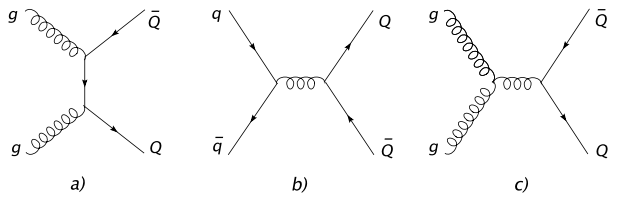

Figure 1.1: Some of the leading order diagrams, describing heavy-flavour production in hadron collisions.

In hadron collisions, heavy quark pairs are produced in the strong interaction of the partons composing the incoming hadrons. The cross section of this process can be estimated in QCD [1]. The overview of the theoretical calculations of the parton distribution functions suitable for the prediction of the heavy quark production at LHC can be found in [2] and [3].

In hadron collisions at the leading order ($\mathcal{O}(\alpha_s^2)$) the heavy quark pairs are mostly produced via gluon fusion $gg \to Q\bar{Q}$ (Fig. 1.1.a,c) and quark-antiquark annihilation $q\bar{q} \to Q\bar{Q}$ (Fig. 1.1.b). The calculation of the heavy flavour production cross section, accounting for the leading order diagrams, can be found, for instance, in [4] and [3]. In order to get a reasonable estimate of the $b\bar{b}$ production cross section at LHC, the next-to-leading order ($\mathcal{O}(\alpha_s^3)$) processes should also be taken into account [2], [3]. At this order, the total cross section of the $b\bar{b}$ production at the center-of-mass energy of 14 TeV is estimated to be approximately 500 μb [1] [3]. The inclusion of the next-next-to-leading order processes in the calculation of the cross section is very complicated, however the prospects for this calculation can be found in [2].

After the $b\bar{b}$-pair is produced in hadron collision, the quark and antiquark undergo hadronization (fragmentation) into b-flavoured hadrons. The probability of the quark Q to fragment into a meson ($Q\bar{q}$) is described by so-called *fragmentation functions*.

The cross section of the production of the given b-flavoured meson in hadron collision can be found by convoluting the QCD cross section with the corresponding fragmentation function. In the case of the CMS experiment at LHC, the value of $BR(\bar{b} \to B_s^0) \simeq 0.107$ is suggested for the branching fraction of the $\bar{b}$ quark fragmentation into the B_s^0 meson[2] [5].

[1] This value of the cross section will be assumed for the $b\bar{b}$ production at LHC hereafter.
[2] This value will be used in the calculations hereafter

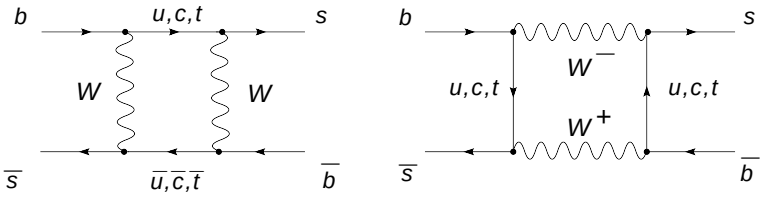

Figure 1.2: Leading order diagrams, contributing to the $B_s^0\bar{B}_s^0$ oscillation.

1.2 Mixing and CP violation in the $B^0 - \bar{B}^0$ system

The process of particle-antiparticle mixing has a fundamental importance in testing the Standard Model and its possible extensions. This phenomenon is induced by the flavour-changing neutral currents, which are forbidden at tree level in the Standard Model. The weak mixing in the system of neutral mesons is responsible for the difference between masses of their mass eigenstates.

The close relation between the processes of weak particle-antiparticle mixing and violation of the CP symmetry was first established after the discovery of the latter in the system of neutral kaons in 1963.

It is natural to expect the same effects to show up in other known systems of neutral mesons, namely $D^0 - \bar{D}^0$ and $B^0 - \bar{B}^0$. However, the situation in the $D^0 - \bar{D}^0$ system is more complicated than in the system of the neutral kaons. The lifetimes of the mass eigenstates are very short ($\tau(D^0_{1,2}) \sim 4 \cdot 10^{-13}$s) and the decay widths are very similar. The oscillation period is expected to be long compared to the lifetime of the eigenstates, and the observation of mixing and CP violation seems thus to be very problematic.

The situation in the $B^0 - \bar{B}^0$ system is much more encouraging. There are two b-flavoured neutral mesons, usually denoted as B^0_d and B^0_s where indices d and s refer to the flavour of the second quark, forming the meson. The phenomenology of the $B^0 - \bar{B}^0$ mixing and its relation to the violation of the CP symmetry together with the methods of extracting physical observables is discussed through the rest of the current chapter.

The B^0_q-mesons ($q = d, s$) are produced in strong interaction in one of the flavour eigenstates B^0_q or $\bar{B}^0_q$, which are not the CP eigenstates. The B^0_q-$\bar{B}^0_q$ mixing occurs mainly through box diagrams (see Fig. 1.2). Due to the mixing effects, the initial state evolves into the time-dependent superposition $|\Psi_q(t)\rangle = a(t)|B^0_q\rangle + b(t)|\bar{B}^0_q\rangle$, satisfying Schrödinger's equation:

$$i\frac{\partial}{\partial t}\begin{pmatrix} a(t) \\ b(t) \end{pmatrix} = \left(M - i\frac{\Gamma}{2}\right) \cdot \begin{pmatrix} a(t) \\ b(t) \end{pmatrix}, \tag{1.1}$$

where $H = M - \frac{i}{2}\Gamma$ is an effective Hamiltonian, and M and Γ are the 2×2 Hermitian mass and decay matrices. The CPT invariance is preserved by requiring $M_{11} = M_{22} \equiv M_0$ and $\Gamma_{11} = \Gamma_{22} \equiv \Gamma_0$. The Hamiltonian (mass) eigenstates are then

$$|B_{\pm}^{(q)}\rangle = \frac{p|B_q^0\rangle \pm q|\bar{B}_q^0\rangle}{\sqrt{|p|^2+|q|^2}}, \tag{1.2}$$

with eigenvalues

$$\lambda_{\pm}^{(q)} = \left(M_0 - \frac{i}{2}\Gamma_0\right) \pm \frac{q}{p}\left(M_{12}^{(q)} - \frac{i}{2}\Gamma_{12}^{(q)}\right), \tag{1.3}$$

where

$$\frac{q}{p} = \sqrt{\frac{M_{12}^* - \frac{i}{2}\Gamma_{12}^*}{M_{12} - \frac{i}{2}\Gamma_{12}}}. \tag{1.4}$$

The deviation of $\left|\frac{q}{p}\right|$ from 1 describes CP violation. In the absence of CP violation, the mass eigenstates are also CP eigenstates: $CP|B_{\pm}^{(q)}\rangle = \pm|B_{\pm}^{(q)}\rangle$. At present, the value of $1 - \left|\frac{q}{p}\right|$ is expected to be of the order of $\sim \mathcal{O}(10^{-3})$ for the B_d^0 system and of the order of $\sim \mathcal{O}(10^{-4})$ for the B_s^0 system respectively [6].

The eigenstates of the Hamiltonian, calculated above, have significantly different masses and decay widths, given by $M_{\pm} = \Re(\lambda_{\pm})$ and $\Gamma_{\pm} = -2\Im(\lambda_{\pm})$ respectively. In the system of the neutral B-mesons the difference of masses of the mass eigenstates is more substantial than the difference of their widths. It is therefore common to denote these eigenstates according to their masses: the B_- state as *heavy* and the B_+ state as *light* [3]. This notation will be used hereafter in the current work.

Taking into account the time evolution of the heavy and light mass eigenstates, the time evolution of the pure B_q^0 or B_q^0 state, produced in the strong interaction at $t = 0$ can be derived:

$$|\Psi(t, B_q^0)\rangle = g_+(t)|B_q^0\rangle + \frac{q}{p}g_-(t)|\bar{B}_q^0\rangle \tag{1.5}$$

$$|\Psi(t, \bar{B}_q^0)\rangle = g_+(t)|\bar{B}_q^0\rangle + \frac{p}{q}g_-(t)|B_q^0\rangle \tag{1.6}$$

The quantities $g_+(t)$ and $g_-(t)$ in Eq. (1.5) and (1.6) are the time-dependent probability amplitudes of the initially produced B_q^0 meson, to be observed at the time t with the same ($g_+(t)$)or opposite ($g_-(t)$) flavour:

$$|g_{\pm}(t)|^2 = \frac{e^{-\bar{\Gamma}_q t}}{2}\left[\cosh\left(\frac{\Delta\Gamma_q}{2}t\right) \pm \cos\left(\Delta m_q t\right)\right], \tag{1.7}$$

[3]Contrary to the system of neutral kaons, where mass eigenstates have similar masses, but substantially different lifetimes. In this system the mass eigenstates are usually denoted according to their lifetimes as "long" and "short".

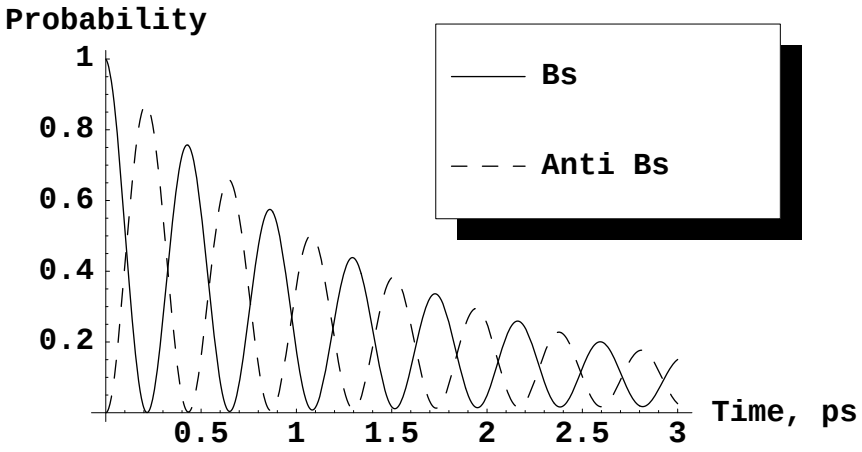

Figure 1.3: Time-dependent probabilities for the produced B_s^0 to be observed as B_s^0 or as $\bar{B}_s^0$.

where

$$\begin{aligned} \Delta m_q &\equiv M_H^{(q)} - M_L^{(q)} = 2|M_{12}^{(q)}| > 0, \\ \Delta\Gamma_q &\equiv \Gamma_H^{(q)} - \Gamma_L^{(q)} = \frac{4\Re(M_{12}^{(q)}\Gamma_{12}^{(q)*})}{\Delta m_q}, \\ \bar{\Gamma}_q &\equiv \frac{\Gamma_H^{(q)} + \Gamma_L^{(q)}}{2} = \Gamma_0^{(q)}. \end{aligned} \tag{1.8}$$

As an example, the probability of the B_s^0 meson, produced at time $t = 0$ to be observed as B_s^0 or $\bar{B}_s^0$ is presented in Fig. 1.3[4].

In the Standard Model, the calculation of the dispersive and absorptive parts of the mixing box diagrams, predicts the following relation between the mixing parameters Δm_q and $\Delta\Gamma_q$ and CKM matrix elements (see Sec. 1.2.2) [6]:

$$\begin{aligned} \Delta m_q &= 2|M_{12}| \sim |(V_{tq}^* V_{tb})^2|, \\ \Delta\Gamma_q &\simeq 2|\Gamma_{12}| \sim \left|\left[(V_{tq}^* V_{tb})^2 + V_{tq}^* V_{tb} V_{cq}^* V_{cb}\mathcal{O}\left(\frac{m_c^2}{m_b^2}\right) + (V_{cq}^* V_{tb})^2\mathcal{O}\left(\frac{m_c^4}{m_b^4}\right)\right]\right|. \end{aligned} \tag{1.9}$$

[4]The lifetimes of heavy and light mass eigenstates as well as the difference of their width, used in this calculation, are taken as the mean values of the recent experimental measurement, reported by the CDF collaboration [7]. The difference between the masses of the eigenstates is taken on the lower limit of currently allowed region (1.10).

It should be noted, that the CDF collaboration found the value of Δm_s to be well above this minimum [7]: $\Delta m_s^{CDF} = 125^{+69}_{-55}$ ps^{-1}, which means that the actual value of the oscillation frequency of the B_s^0-meson may appear to be significantly higher than the one, presented in Fig. 1.3. Due to the large systematic errors, this result should be reconfirmed with higher statistics and possibly other measurements.

Experimentally, the parameters of the $B_q^0 - \bar{B}_q^0$ mixing can be studied in several different ways. One possibility is provided by time-integrated measurements. The time-integrated mixing probability can only be measured with flavour-specific decay channels, where the B_q^0 and $\bar{B}_q^0$ decay to the final states f and $\bar{f}$ respectively, while the cross-over decay modes are forbidden. The semileptonic decays (e.g $B \to l\bar{\nu}X$, $\bar{B} \to \bar{l}\nu X$) are typically used for this purpose. The measurement technique is based on counting of same- and opposite-sign charged lepton pairs from the semileptonic decays.

As the time-integrated probability of the $B_q^0 \to \bar{B}_q^0$ transition saturates toward 1/2 at large values of $x_q = \Delta m_q/\bar{\Gamma}_q$, this measurement is not possible in the $B_s^0 - \bar{B}_s^0$ system. There the large value of x_s implies maximal mixing, making the time-integrated analysis not sensitive to the actual value of x_s [6].

The sensitivity can be obtained from time-dependent analysis, where the oscillation frequencies Δm_q are directly measured from the distributions of the proper lifetime of flavour-tagged B_q^0 candidates. To tag the B_q^0 candidate as mixed or unmixed it is necessary to determine the flavour of both initial and final states. In case of semileptonic decays, the final state is usually tagged by the charge of the final state lepton.

The methods to tag the initial state can be subdivided in two groups. The methods of the first group tag the charge of the b quark contained in the B-meson itself The methods of the second group tag the initial charge of the other b quark, produced in the same event.

At present, the oscillation of the B_d^0 meson is relatively well studied by a number of collaborations at LEP, Tevatron and b-factories. The present world average of the strength of the B_d^0 mixing yields $\Delta m_d = 0.502 \pm 0.007$ ps^{-1} [6].

The study of the mixing and CP violation in the B_s^0 system appears to be more difficult, mainly due to the large value of the Δm_s, resulting in high oscillation frequency and requiring the ultimate detector resolution. The present PDG lower limit for Δm_s is [6] :

$$\Delta m_s > 14.4 \text{ ps}^{-1} \quad \text{at } 95\% \text{ CL.} \tag{1.10}$$

1.2.1 The CP violation and the CKM matrix

In order to include the CP violation effects into the Standard Model, Kobayashi and Maskawa (1973) proposed to introduce the third quark doublet, composed of t (*top*) and b (*bottom*) quarks [8]. The Cabibbo-GIM quark mixing schema is then generalized to three quark generations and d, s and b quarks are assumed to participate in

the weak interaction through their linear combinations:

$$\begin{pmatrix} d' \\ s' \\ b' \end{pmatrix} = \begin{pmatrix} V_{ud} & V_{us} & V_{ub} \\ V_{cd} & V_{cs} & V_{cb} \\ V_{td} & V_{ts} & V_{tb} \end{pmatrix} \begin{pmatrix} d \\ s \\ b \end{pmatrix}. \tag{1.11}$$

By convention, the matrix V is called the *Cabibbo-Kobayashi-Maskawa* (CKM) *quark mixing matrix*. The unitarity condition

$$V_{CKM}^{\dagger} V_{CKM} = I \tag{1.12}$$

guarantees the absence of the flavour-changing neutral currents. The minimal parametrization of the CKM matrix (1.11) consists of three rotation angles, describing the quark mixing, and one phase, accounting for the CP violation effects. The "standard" parametrization, advocated by the Particle Data Group [9], is:

$$V_{CKM} = \begin{pmatrix} c_{12}c_{13} & s_{12}c_{13} & s_{13}e^{-i\delta} \\ -s_{12}c_{23} - c_{12}s_{23}s_{13}e^{i\delta} & c_{12}c_{23} - s_{12}s_{23}s_{13}e^{i\delta} & s_{23}c_{13} \\ s_{12}s_{23} - c_{12}c_{23}s_{13}e^{i\delta} & -c_{12}s_{23} - s_{12}c_{23}s_{13}e^{i\delta} & c_{23}c_{13} \end{pmatrix}, \tag{1.13}$$

where $c_{ij} = \cos\theta_{ij}$, $s_{ij} = \sin\theta_{ij}$ and $i, j = 1, 2, 3$ are the "generation labels". In the limit $\theta_{23} = \theta_{13} = 0$, the CKM matrix reduces to the Cabibbo-GIM quark mixing matrix and the angle θ_{12} is identical to the Cabibbo angle.

The elements of the CKM matrix are free parameters of the Standard Model, hence their values should be determined experimentally by studying the weak decays of relevant quarks. The present 90% confidence limits on the magnitude of the elements of V_{CKM}, taking into account the unitarity constraint are [9]:

$$\begin{pmatrix} 0.9739 \text{ to } 0.9751 & 0.221 \text{ to } 0.227 & 0.0029 \text{ to } 0.0045 \\ 0.221 \text{ to } 0.227 & 0.9730 \text{ to } 0.9744 & 0.039 \text{ to } 0.044 \\ 0.0048 \text{ to } 0.014 & 0.037 \text{ to } 0.043 & 0.9990 \text{ to } 0.9992 \end{pmatrix}. \tag{1.14}$$

The hierarchy of the CKM matrix elements, induced by the observing hierarchy of the mixing angles $1 \gg \theta_{12} \gg \theta_{23} \gg \theta_{13}$ was first used by Wolfenstein in 1983 [10] to propose an approximate parametrization, in which each element is expanded as a power series in the small parameter $\lambda = V_{us}$:

$$V_{CKM} = \begin{pmatrix} 1 - \lambda^2/2 & \lambda & A\lambda^3(\rho - i\eta) \\ -\lambda & 1 - \lambda^2/2 & A\lambda^2 \\ A\lambda^3(1 - \rho - i\eta) & -A\lambda^2 & 1 \end{pmatrix} + \mathcal{O}(\lambda^4), \tag{1.15}$$

where $\rho = \frac{s_{13}}{s_{12}s_{23}} \cos\delta$, $\eta = \frac{s_{13}}{s_{12}s_{23}} \sin\delta$ and $A = s_{23}/\lambda$.

The unitarity of the CKM matrix leads to the set of nine equations, each representing the unitarity condition applied to two rows or columns of the quark-mixing

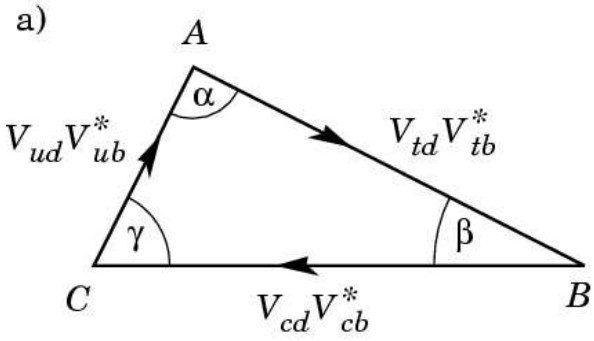

Figure 1.4: Unitarity triangle, corresponding to the orthogonal relation (1.16).

matrix. Of these nine equations, six are representing non-trivial combinations of rows and columns of the CKM matrix are equal to 0. These six relations can be represented by triangles in the complex plane. For instance, for first and last column one gets:

$$V_{ud}V^*_{ub} + V_{cd}V^*_{cb} + V_{td}V^*_{tb} = 0. \tag{1.16}$$

The unitarity triangle described by the expression (1.16) is usually quoted as *the* unitarity triangle (see Fig. 1.4).

Since the combination $V_{cd}V^*_{cb}$ in Eq. (1.16) is real to the highest accuracy and equal to $A\lambda^3$, it is possible to rescale the triangle by dividing all the sides to this quantity. The sides (AC) and (AB) then become equal to $\bar{\rho}+i\bar{\eta}$ and $1-(\bar{\rho}+i\bar{\eta})$ respectively, where $\bar{\rho} = \rho(1-\lambda^2/2)$ and $\bar{\eta} = \eta(1-\lambda^2/2)$. The triangle is then fully defined by two sides (AC) and (AB) or three angles α, β and γ, which values can be extracted from physical observables.

The unitarity triangles are only a graphical representation of the properties of the CKM matrix, however the measurements of the its sides and angles provide an excellent test of the Standard Model. Any discrepancy would signal the contribution of the non-Standard Model processes. Indeed, the unitarity relation yield a triangle only if 3 generations exist [11] and Standard Model provides a correct description of the weak interaction.

In order to test the Standard Model of weak interactions, it is then essential to constrain the position of the apex A in as many as possible different ways. The results of these measurements should agree well with each other and any contradiction been found would indicate the presence of the effects Beyond the Standard Model. The summary of present experimental constraints on the unitarity triangle is shown in Fig. 1.5 [12]. As it will be shown later, the decay $B^0_s \to (J/\psi)\phi$ can be used

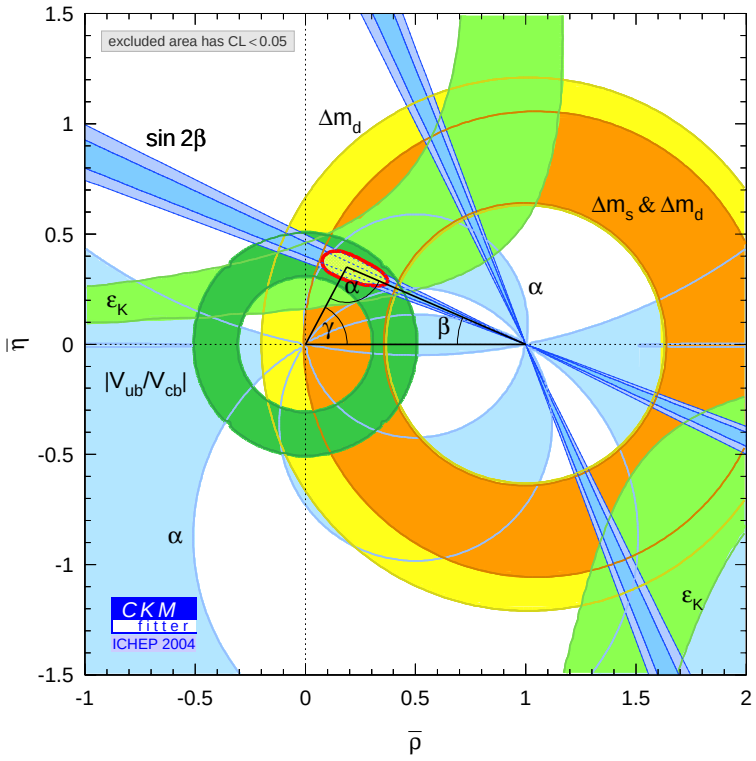

Figure 1.5: Present constraints on the parameters of the unitarity triangle.The constraints presented come from the measurement of the CP violation in the system of neutral kaons ε_K, measurements of the B^0-mixing parameters Δm_s and Δm_d, and the measurement of $\sin 2\beta$ in kaon and B-meson decays. The allowed regions from different measurements are shown in color, whereas the white fields are excluded at 95 % confidence level and the apex A is placed in the preferred region. No significant contradiction between the different constraints is observed so far.

to constrain the Wolfenstein parameter η, fixing the height of the unitarity triangle (Eq. 1.18).

1.2.2 CP violation in the $B^0 - \bar{B}^0$ system

In the decay $B_s^0 \to (J/\psi)\phi$, the CP violation arises through the interference of the $B_q^0 - \bar{B}_q^0$ mixing and decay (see Fig. 1.6). Here the final states f is common to both B_q^0 and $\bar{B}_q^0$. The time dependent asymmetry is then given by:

$$A_f(t) = \frac{\Gamma(\bar{B}_q^0(t) \to f) - \Gamma(B_q^0(t) \to f)}{\Gamma(\bar{B}_q^0(t) \to f) + \Gamma(B_q^0(t) \to f)} \tag{1.17}$$

This asymmetry is only generated if a weak mixing phase arising from $\frac{q}{p}$ is different from the weak decay phase.

Of particular interest is the case where the final state f is an eigenstate of the CP operator. This is the case for the $B_s^0 \to (J/\psi)\phi$ channel, which is the subject of the current thesis.

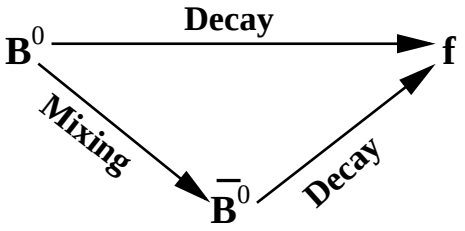

Figure 1.6: The interference between decay and mixing in the system of neutral b-flavoured mesons.

In the $B_s^0 - \bar{B}_s^0$ system, the $B_s^0 \to (J/\psi)\phi$ decay is suitable for the measurement of the Wolfenstein parameter η, fixing the height of the unitarity triangle:

$$A_{CP}(B_s^0 \to D_s^{*+} D_s^{*-}, B_s^0 \to (J/\psi)\phi, t) \simeq \eta_f \sin(2\lambda^2\eta) \sin(\Delta m t). \tag{1.18}$$

An experimental measurement of this asymmetry was not yet reported. As in the Standard Model the value of $2\lambda^2\eta$ is predicted to be $\mathcal{O}(0.03)$, a larger measurement would most probably signal new physics [13].

1.2.3 The $B_s^0 \to (J/\psi)\phi \to \mu^+\mu^- K^+ K^-$ decay

The $B_s^0 \to (J/\psi)\phi$ decay channel followed by $(J/\psi) \to \mu^+\mu^-$ and $\phi \to K^+K^-$ decays, which is the aim of the current study, is a particular case of the B_s^0 decay to the CP eigenstates. This channel is usually refereed to as a *gold-plated* transition, because it allows the investigation of Δm_s, $\Delta\Gamma_s$, $\bar{\Gamma}_s$, Γ_s^H and Γ_s^L, as well as the extraction of the Wolfenstein parameter η, fixing the height of the unitarity triangle.

The $B_s^0 \to (J/\psi)\phi$ decay exhibiting the $b(\bar{s}) \to c\bar{c}s(\bar{s})$ transition is mainly possible through electroweak spectator, QCD and electroweak penguin diagrams, presented in Fig. 1.7. However, the penguin amplitudes are highly suppressed with respect to the spectator amplitude (Fig. 1.7 .(a)) [13]. The decay process is therefore dominated by a single CKM amplitude, providing an excellent laboratory to study the mixing-induced CP violation, where the asymmetry to be investigated is the one given by equation 1.18.

The experimental ways of extracting the physical observables can be subdivided in two groups. The traditional approach consists in the study of the distribution of the lifetime of untagged and tagged reconstructed B_s^0 candidates. The study of the untagged distribution yields lifetimes of the heavy and light mass eigenstates. The practical details of this measurement are discussed in Section 5.2 and Appendix B. The study of tagged distributions of the lifetime provide a possibility of direct observation of the $B_s^0 - \bar{B}_s^0$ mixing process and extraction of Δm_s.

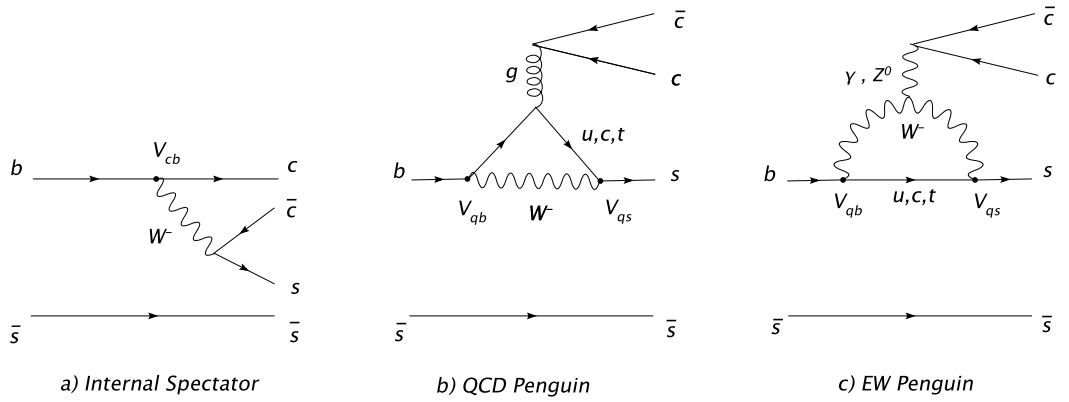

Figure 1.7: Diagrams, contributing to the $B_s^0 \to (J/\psi)\phi$ decay.

The methods of flavour tagging of the B_s^0 candidate can be subdivided in two groups, according to which of two b quarks is tagged. The *opposite side tagging* is performed by measuring the charge of the lepton coming from the semileptonic decay of the opposite B-meson. The *same side tagging* is performed through the identification of the K^- and K^+, following the $b \to \bar{B}_s^0$ and $\bar{b} \to B_s^0$ fragmentation processes respectively.

The time-dependent asymmetry (1.18) yields estimate of the CP violating CKM phase. In all cases, the actual extraction of the physical observables is usually performed using the method of *Maximum Likelihood* [14], allowing one to fit the unbinned experimental measurements according to a given theoretical model.

An alternative way of extracting the mixing parameters and the CP violating Wolfenstein parameter η in the $B_s^0 \to (J/\psi)\phi \to \mu^+\mu^- K^+ K^-$ decay is provided by the study of the angular distributions of the final state. One of the advantages of this method is the possibility of extraction of the CKM phases both with and without tagging [15, 16]. The method of angular analysis also provides a possibility to extract the frequency of particle-antiparticle oscillation from the flavour-tagged sample. This possibility is indeed attractive, since the B_s^0 oscillations are very rapid (See Eq. (1.10) and Sec. 1.2) and the possibility of their direct observation may be limited by the resolution of the detector.

Two main ideas, forming the basis of the method of the angular analysis, can be summarized as follows:

- The mixing in the $B_s^0 - \bar{B}_s^0$ system gives rise to the mass eigenstates B_s^L and B_s^H with lifetimes which are expected to differ by about 10 to 30%. To a good approximation, CP violation can be neglected ($\frac{q}{p} = 1$) in calculating heavy

and light mass eigenstates, in which case they correspond to the odd and even CP eigenstates respectively. The final state of the decay then represents an admixture of the CP-eigenstates.

- The J/ψ and ϕ are massive neutral vector mesons ($J^{PC} = 1^{--}$) with the same (even) CP parity. The spectrum of zero-angular-momentum states of the $(J/\psi)\phi$ system consists of states with orbital angular moments: $L = 0$ (CP-even), $L = 1$ (CP-odd) and $L = 2$ (CP-even). To disentangle the different CP eigenstates, the decay amplitude can be decomposed into independent components, corresponding to the the linear polarization states of the final state vector mesons. The polarization states can be longitudinal ($A_0(t)$), or transverse to the direction of motion of final state vector mesons. In case of transverse polarization, the states can be parallel ($A_\parallel(t)$) or perpendicular ($A_\perp(t)$) to each other [17]. The CP-odd ($A_\perp(t)$) and CP-even ($A_0(t)$, $A_\parallel(t)$) components of decay amplitude have different angular dependencies. In general form of the differential decay rate of the B_s^0 decay can be written as: $\frac{d^2\Gamma(B_s(t))}{d\Theta dt} = \sum_i b^{(i)}(\alpha, t)g^{(i)}(\Theta)$, where $g^{(i)}(\Theta)$ are the angular distributions of the final state components, Θ denotes generically decay angles and functions $b^{(i)}(\alpha, t)$ are the time evolutions of the physical observables. The quantity α denotes generically all the kinematics independent physical parameters.

In case of the $B_s^0 \to (J/\psi)\phi$ decay, time evolutions of the physical observables are bilinear combinations of decay amplitudes:

$$\begin{aligned} &|A_0(t)|^2, \qquad |A_\parallel(t)|^2, \qquad |A_\perp(t)|^2, \\ &\Re(A_0^*(t)A_\parallel(t)), \quad \Im(A_\parallel^*(t)A_\perp(t)) \quad \text{and} \quad \Im(A_0^*(t)A_\perp(t)). \end{aligned} \tag{1.19}$$

These quantities are functions of $\bar{\Gamma}$, Γ_H, Γ_L, Δm_s and CP-violating Wolfenstein parameter η [18].

The explicit calculation of the time evolution of the observables (1.19) is performed in [18] and [17]. The resulting differential decay rates, corresponding to the tagged and untagged $B_s^0 \to (J/\psi)\phi \to \mu^+\mu^- K^+K^-$ samples are presented in the Appendix A (see Eq. (A.1) and (A.2)).

The usual way of extracting the physical observables from the differential decay rates is the use of unbinned likelihood fit. In this case, the equations (A.1) and (A.2) can be used as probability density functions.

The alternative solution is provided with the method of weighting functions. The central idea of this method is to find a weighting function $w^{(i)}$, which projects out

the physical observable $b^{(i)}$, being convoluted with the differential decay rate. The processes of extraction of different physical observables are therefore completely decoupled. The possible sets of weighting functions, suitable to extract the physical observables (1.19) in both tagged and untagged cases, can be found in [18]. As this method will not be used in the present thesis, interested readers are referred to [18].

Chapter 2

The CMS experiment at LHC

2.1 The Large Hadron Collider at CERN

The Large Hadron Collider (LHC) is a new accelerator facility of the European Laboratory for Particle Physics (CERN), located near the town of Geneva, Switzerland. The LHC accelerator is designed to perform proton-proton and heavy ions ($^{208}\mathrm{Pb}^{82+}$) collisions at center-of-mass energies of 14 TeV and 1148 TeV respectively. After its launch, scheduled for the year 2007, the LHC will become the world leading facility for high-energy hadron physics.

Since two beams with particles of equal charge are to collide in LHC, dipole magnetic fields of opposite polarity are required for both beams. The LHC beams are therefore separated, each having its own acceleration ring, superconducting dipole magnets and vacuum chambers. The beams share only the short fractions of the beampipe in the experimental areas.

The accelerator rings are set up in the underground tunnel which previously hosted the Large Electron-Positron Collider (LEP) of CERN. The underground tunnel is 27 km long (approximately 8.6 km in diameter), extending on the territory of France and Switzerland (see Fig. 2.1). In addition to the underground infrastructure inherited from LEP, new experimental halls, cooling towers, and tunnels intended to host the beam transfer lines have been constructed. The underground layout of the Large Hadron Collider with respect to the existing structures, inherited from the LEP accelerator is presented in the Fig. 2.2.

The event rate at the LHC can be estimated using the relation:

$$R = \mathcal{L}\sigma, \tag{2.1}$$

where σ is the cross section of the events under study. The proportionality factor $\mathcal{L}$ in Eq. (2.1), called *luminosity*, represents the technical characteristics of the collider,

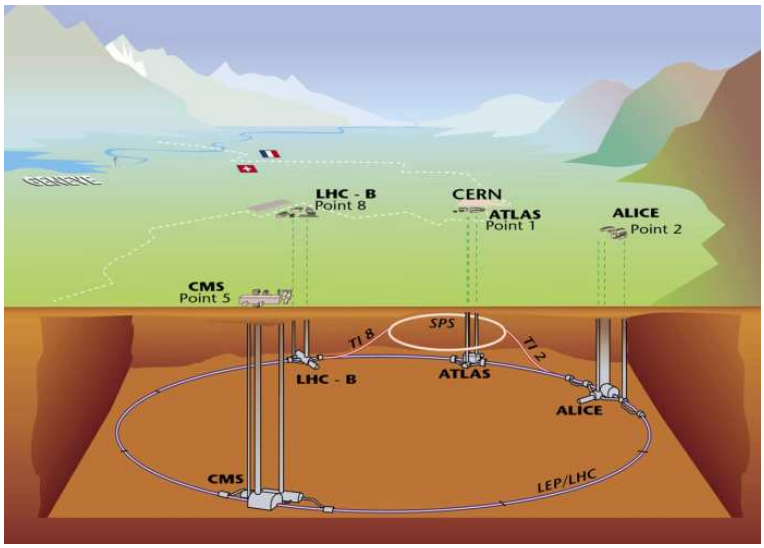

Figure 2.1: The Large Hadron Collider at CERN.

depending on the beam parameters such as number of particles per bunch, revolution frequency, transverse beam profiles, beam-to-beam crossing angles and others. In *pp* collisions at LHC, the maximal luminosity of $2 \cdot 10^{33}$ cm^{-2}s^{-1} during the phase-I (first several years of operation) and of 10^{34} cm^{-2}s^{-1} during the phase-II of the accelerator is intended to be achieved [19]. The main technical properties of the LHC accelerator, when working at peak luminosity in *pp* collision mode, are summarized in Table 2.1.

The LHC accelerator ring will be supplied with protons from the injector chain, composed of presently existing CERN accelerators, upgraded to meet the requirements of LHC in terms of intensity and number of bunches. The acceleration chain starts with the linear accelerator (LINAC), accelerating protons to an energies of 50 MeV. The particles are then injected into the Proton Synchrotron Booster (PSB), and later into the Proton Synchrotron (PS) ring. After the PSB-PS cycle, the protons have an energy of 25 GeV and the particle bunches, suitable for the use in the LHC, are formed. The last part of the injector chain is the Super Proton Synchrotron (SPS), which accelerates proton bunches up to 450 Gev and injects them into the LHC ring [19].

The total amount of time taken by the injection system to fill the LHC accelerator is estimated to be approximately 16 minutes. The minimal time required for ramping up the LHC magnets from 450 GeV to the collision energy of 7 TeV is approximately 20 minutes. The same amount of time is required to ramp the magnets down after the beam abort. The total LHC turnaround time can therefore be estimated to

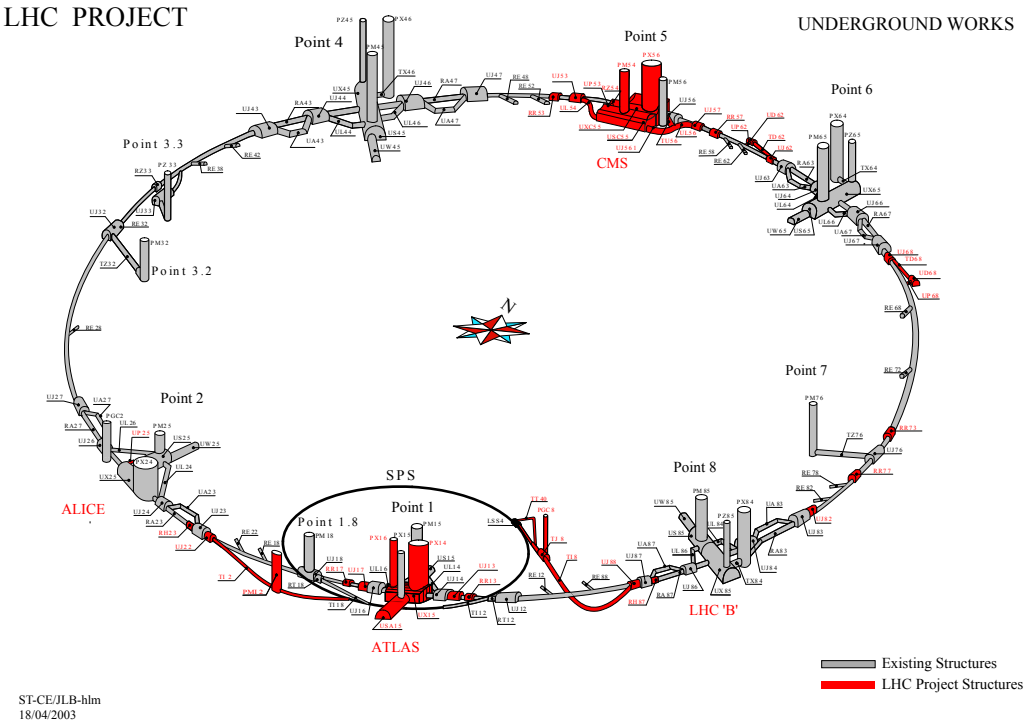

Figure 2.2: Underground layout of the Large Hadron Collider at CERN.

be of approximately 70 minutes. The integrated luminosity per run can be then calculated using the following relation:

$$L_{\text{int/run}} = \mathcal{L}\tau_L \left[1 - e^{-\frac{T_{\text{run}}}{\tau_L}}\right],$$

where T_{run} is the total length of the luminosity run, $\mathcal{L}$ is the peak luminosity value and τ_L is the luminosity lifetime. These and other technical properties of the Large Hadron Collider at CERN are summarized in the Table 2.1. Assuming that the machine can be operated during 200 days a year, the total integrated luminosity between 80 and 120 fb^{-1} can be achieved, depending on the actual turnaround time.

At present, there are four experiments, in preparation for working at the LHC environment in the proton-proton collisions mode. Two of them, CMS [20] and ATLAS [21], are the general-purpose detectors, designed to work at the peak luminosities mentioned above. The main goals of these two collaborations is the exploration of the limits of the Standard Model: searches of Standard Model and Supersymmetric Higgs bosons, supersymmetric partners of the Standard Model particles and high precision physics of t and b quarks.

Proton energy at Injection (GeV)	450
Proton energy at Collision (GeV)	7000
Number of particles per bunch	$1.15 \cdot 10^{11}$
Number of bunches	2808
Bunch spacing (ns)	25
Stored energy per beam (at Collision) (MJ)	362
Total pp cross section (mb)	100.0
Inelastic pp cross section (mb)	60.0
Events per bunch crossing (high luminosity mode)	19.02
Energy loss per turn due to synchrotron radiation (eV)	$6.71 \cdot 10^3$
Total luminosity lifetime τ_L (hours)	14.9

Table 2.1: Technical properties of the Large Hadron Collider at CERN, relevant to the pp high luminosity mode.

The other two experiments, scheduled to work in proton-proton collision mode are LHC-b[22] and TOTEM[23]. The LHC-b experiment is dedicated for the b-physics studies at the luminosity of 10^{32} cm^{-2}s^{-1}. The TOTEM collaboration intends to study the elastic low-angle scattering of protons at luminosity of $2 \cdot 10^{29}$ cm^{-2}s^{-1}.

The LHC accelerator will also run with collisions between beams of lead ($^{208}\mathrm{Pb}^{82+}$) ion. The heavy ion collisions will be principally studied at specialized ALICE [24] experiment, with CMS and ATLAS also having a heavy ion programs.

2.2 The CMS Detector

The Compact Muon Solenoid (CMS) is a multipurpose particle detector designed to study proton-proton collisions at the Large Hadron Collider at CERN. The overall design of the detector is motivated by the variety of the physics signatures foreseen:

- The major goal of the CMS is the search for Standard Model and Supersymmetric Higgs bosons in proton-proton collisions at high luminosity. In Fig. 2.3 the branching fractions of the different decay channels of the Standard Model Higgs boson as function of mass are presented. Depending on the mass of the Higgs boson, the following channels can be regarded as possible candidates for

the discovery [25]:

$$H(115\text{ GeV}) \to \gamma\gamma,\ H(120\text{ GeV}) \to ZZ^* \to 4l,$$
$$H(500\text{ GeV}) \to WW \to ll\nu\nu,\ H(800\text{ GeV}) \to l\nu \text{ jet jet}.$$

The Supersymmetric Higgs bosons can be searched in the channels with the same final states, however the channels involving the decays of SUSY Higgses to $\tau\bar{\tau}$ and $b\bar{b}$ pairs are also important.

- The other important topic to study with CMS is the search for the supersymmetric partners of the Standard Model particles. If Supersymmetry is indeed realized in our world, CMS might be able to detect the decays of squarks and gluinos. To achieve this goal, final states with numerous jets and hard leptons should be studied.

- Taking the advantage of working at the low luminosity ($\mathcal{L} = 2 \cdot 10^{33}$ cm$^{-2}s^{-1}$) mode during the first several years of the LHC operation, the CMS collaboration plans a number of studies in the field of b-physics. Here the most important topics are the study of the oscillation of the neutral b-flavoured mesons, study of the CP violation in B-decays, measurement of the parameters of the unitarity triangle. In addition to the $B_s^0 \to J/\psi(\to l^+l^-)\phi(\to K^+K^-)$ channel, discussed in this thesis, decays $B_d^0 \to J/\psi(\to l^+l^-)K_s(\to \pi^+\pi^-)$ (extraction of the angle β of the unitarity triangle), $B_d^0 \to \pi^+\pi^-$ (extraction of angle α of the unitarity triangle) and others will also be studied.

- Finally, the LHC environment provides an excellent laboratory to study the physics of the top quark. Even in the low luminosity phase of the accelerator, $t\bar{t}$ pairs will be produced with a rate of about one per minute [25]. The top quark was discovered at Tevatron in 1994 [26, 27], nevertheless its mass is still known with a relatively large uncertainty. The precise measurement of the top mass becomes therefore one of the major goals of the LHC. This measurement can be performed investigating $t \to Wb$ and similar decay channels.

In order to be able to detect efficiently the variety of physics signatures listed above, the design of the CMS detector should allow precise measurements of the photons, muons and electrons over a large energy range. Special care should be taken for the efficient detection of the soft muons coming from the b-decays[1]. The detector

[1]The efficient detection of the muon pairs, coming from the $B \to J/\psi(\to \mu^+\mu^-)X$ decays, is of great importance for the b- and t-physics studies. These muons have a transverse momentum of few GeV, to be compared for instance with the muons, coming from the Higgs decay, where momenta of several tens of GeV are typical. The CMS detector should therefore provide an efficient detection of muons in the wide range of energies and transverse momenta.

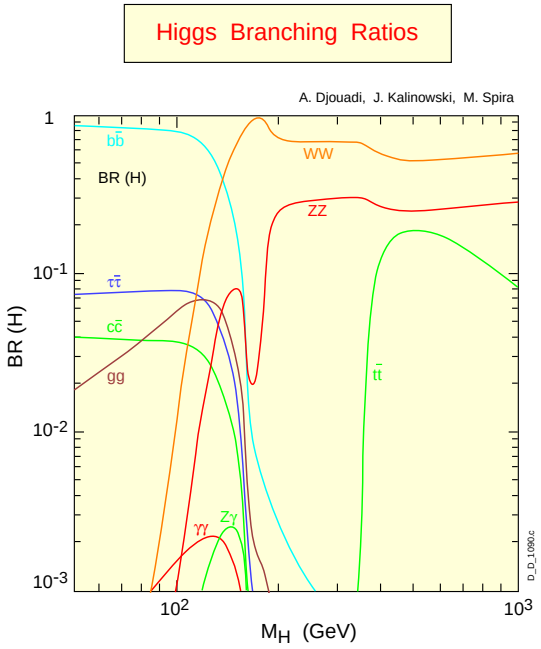

Figure 2.3: Decay branching fractions of the Standard Model Higgs boson as a function of its mass.

should also provide a possibility of the precise reconstruction of charged tracks over a large range of transverse momenta. Accounting for the large multiplicity of charged particles in the hadron collisions and high luminocity of the LHC, the detector should be granular enough in order to minimize the probability of the pile up particles be in the same detector unit as interesting object. In addition, the identification of the b-decays, which is equally important for Higgs, t- and b-physics, requires the reconstruction of secondary vertices with a very high space resolution.

2.2.1 Geometry and general layout

The general layout of the CMS detector is presented in Fig. 2.4. The choice of the magnet system was the starting point of the CMS detector design. A superconducting solenoid of 13 m length and inner diameter of 5.9 m with a uniform magnetic field of 4 T was chosen. The magnetic flux is returned via 1.8 m thick iron yoke (in yellow), which is instrumented with the muon chambers (in red). The return yoke is composed of the barrel part with the pseudorapidity[2] coverage of $|\eta| < 1.5$ and two end caps, extending the coverage up to $|\eta| < 3.0$.

The central tracker and the calorimeters are located inside the inner coil of the solenoid. The central tracker of CMS ([28], [29]) is composed of two parts: the pixel

[2]The pseudorapidity is a measure of the polar angle θ, defined as $\eta = -\log(\tan\frac{\theta}{2})$.

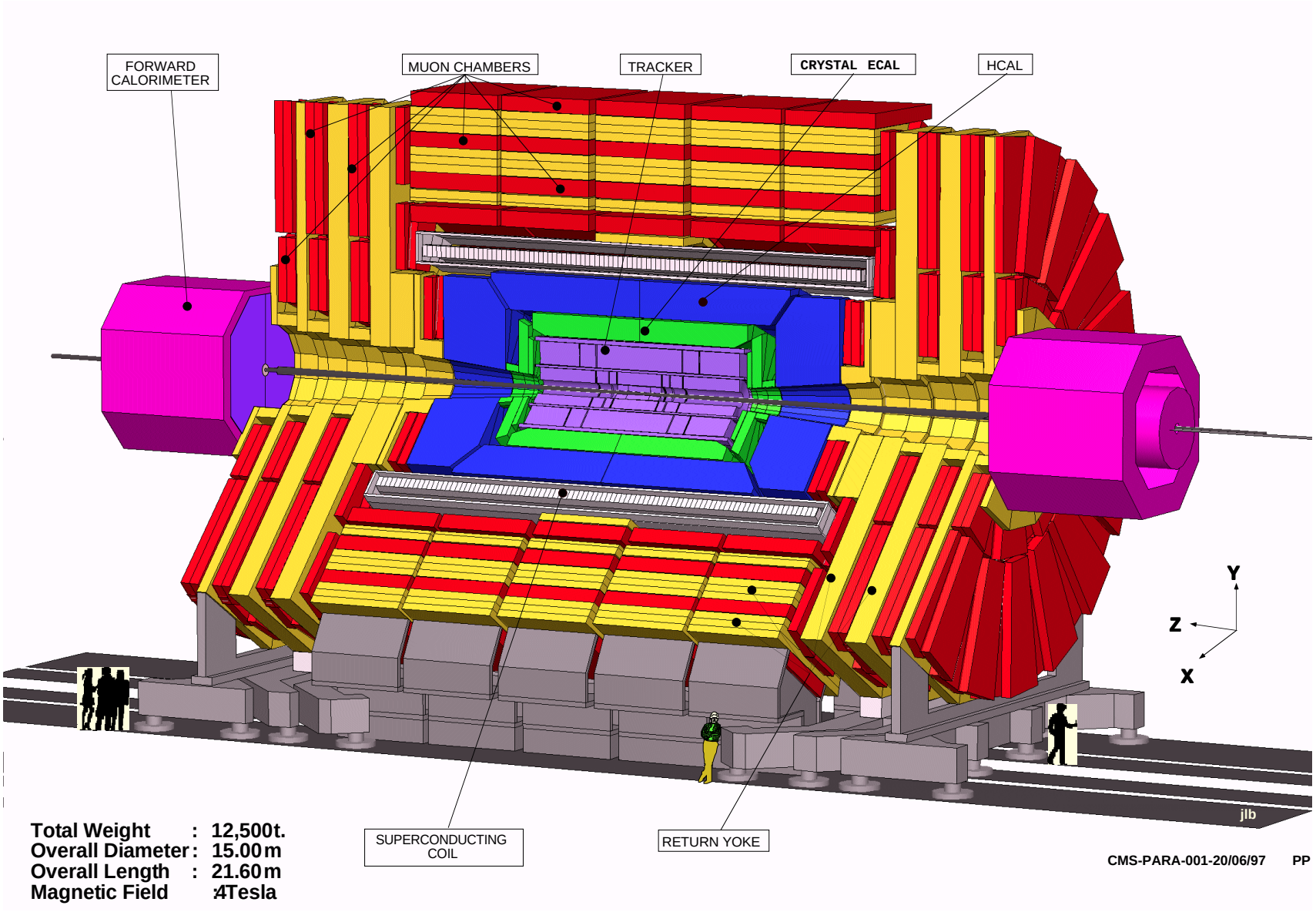

Figure 2.4: General layout of the CMS detector at the Large Hadron Collider at CERN.

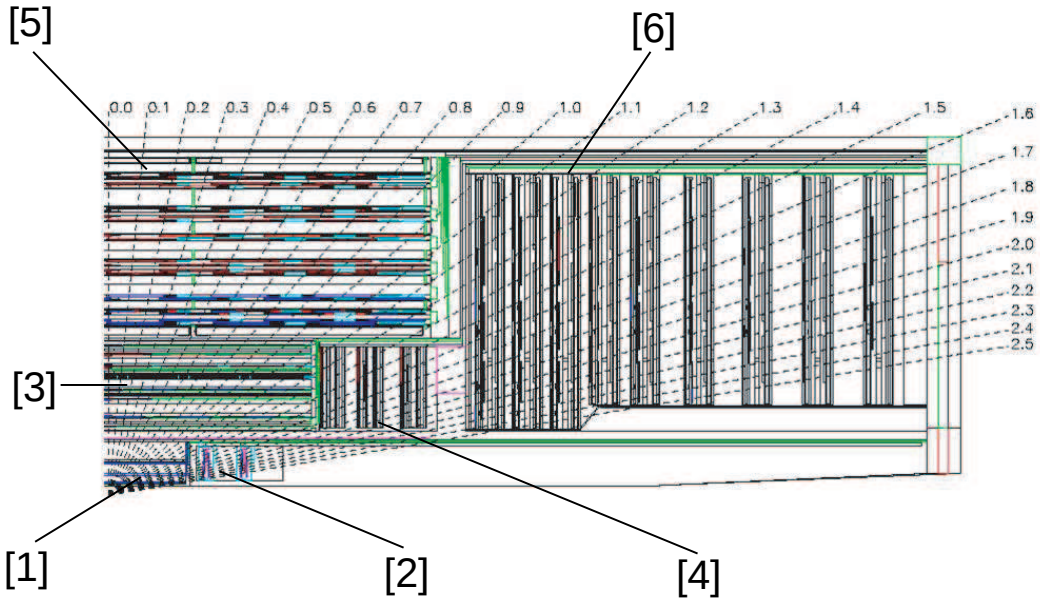

Figure 2.5: Longitudinal cross section of the first quarter of the CMS central tracker. [1] Pixel Barrel, [2] Pixel End Caps, [3] Tracker Inner Barrel (TIB), [4] Tracker Inner Disks (TID), [5] Tracker Outer Barrel (TOB), [6] Tracker End Caps (TEC).

detector and the silicon microstrip tracker. The longitudinal layout of one quater of the CMS tracker, including Silicon Pixel and Silicon Strip detectors is presented in Fig. 2.5. The pixel detector is housed in a cylindrical volume of 1 m length and 30 cm diameter centered around the interaction point. The detector consists of three barrel layers, placed at radii of 4.4 cm, 7.3 cm and 10.2 cm with respect to the beam axis and two pairs of end cap disks, located at $|z| = 34.5$ cm and 46.5 cm. The pseudorapidity coverage of the pixel detector is $|\eta| < 2.2$.

The Silicon Strip Tracker (SST) covers the radial region between 20 and 110 cm. It is is subdivided in four parts. The barrel region ($|z| < 120$ cm) is split into Inner Barrel (TIB), composed of four cylindrical layers, and an Outer Barrel (TOB), made of six layers. The TIB is completed with 3 pairs of disks (TID), while the TOB is enclosed by nine End-Cap (TEC) disks ($120 < |z| < 280$), each made of seven rings.

The Silicon Strip Tracker of the CMS is surrounded by the Electromagnetic Calorimeter (ECAL). The CMS ECAL [30] is composed of 75848 lead tungsten ($PbWO_4$) crystals, arranged in a barrel, covering the central pseudorapidity region of $|\eta| < 1.48$ and two end caps, extending the angular coverage up to $|\eta| < 3$. The barrel crystals with the tapered shape (2.2×2.2 cm^2) front face and 23 cm length are positioned at a radius of 129 cm with respect to the beam axis. In the end caps,

crystals with 2.47×2.47 cm^2 face and 22 cm length are positioned at the distance of 3.17 m from the interaction point along the beam line.

The last part of the detector hosted inside the inner coil of the superconducting solenoid is the Hadron Calorimeter (HCAL) [31]. The HCAL consists of the central barrel (HB) and two end caps (HE), covering the $|\eta| < 3.0$ pseudorapidity range. The central barrel is 9 m long, one meter thick and has an inner diameter of 6 meters. The end caps have am inner diameter of 0.6 m, outer diameter of 8 m and thickness of 1.8 meters along the z direction. Both HB and HE are made of wedges of brass and scintillator. Since the barrel part of the HCAL is only only 6.5 interaction length thick, additional scintillators (HO) are installed inside the muon barrel system, outside the coil of the solenoid. This part of the HCAL uses the coil of the material of the solenoid as additional absorber.

The design of the Hadronic Calorimeter is completed with a pair of Very Forward Hadron Calorimeters (HF) intended to measure the forward jets. The HF are located at $z = \pm 11$ m from the interaction point and extend the pseudorapidity coverage of the HCAL from $|\eta| < 3.0$ to $|\eta| < 5.0$ (see Fig. 2.4).

The transverse cross section of the barrel part of the CMS detector is presented in Fig. 2.6. The principle of detection of charged and neutral particles in the various subdetectors is shown. The properties of the different components of the CMS detector are discussed in more details in the following sections. Emphasis will be given to the subdetectors used in this analysis, in particular to the pixel detector which is built by our group in collaboration with other institutes.

2.2.2 The CMS Pixel Detector

The pixel detector is the innermost component of the CMS experimental setup. The CMS pixel detector[3] consists of three cylindrical barrel layers and two pairs of end cap disks, placed from both sides of the barrel, which provides 3 hit coverage over the pseudorapidity region of $|\eta| \leq 2.4$ (see Fig 2.7). Both barrel planes and disks are composed of planar detector elements, which have the sandwich structure presented in Fig. 2.8. Plaquettes of arrays of pixel detectors are bump-bonded to readout chips.

As mentioned above, cylindrical barrel layers of the pixel detector will be located at radii of several cm from the beam line. The innermost layer is thus expected to be exposed to a fluence[4] of $3 \cdot 10^{14}$ n_{eq}/cm^2 per year during the high luminocity

[3]Build by PSI, CERN, ETHZ, the Universities of Zurich, Basel, HEPHY Vienna, FNAL and other institutes.

[4]All particle fluences are normalized to 1 MeV neutrons (n_{eq}/cm^2).

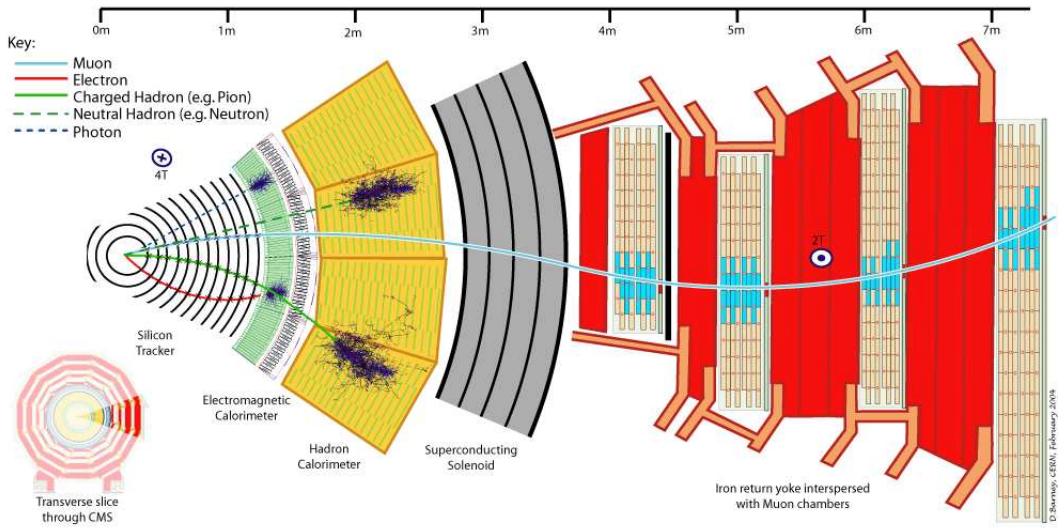

Figure 2.6: Transverse cross section of the CMS barrel. The detection principle of neutral and charged particles is shown.

run of the LHC. The second and third layers will be exposed to the fluence of $1.4 \cdot 10^{14}$ n_{eq}/cm^2 and $0.6 \cdot 10^{14}$ n_{eq}/cm^2 per year respectively.

The pitch size of individual silicon sensor diode is 100 μm $\times$ 150 μm. A schematic cross section of the silicon sensor diode is presented in Fig. 2.9. The sensors are made of an n-doped bulk silicon wafer of approximately 300 μm thickness. One side of the wafer is implanted with acceptor impurities at typical densities of 10^{14} cm^{-3} (designated as $p+$ in Fig. 2.9). The other side of the wafer is implanted with an array of donor implants of high density (the doping density is similar to the $p+$ implants and designated as $n+$ in Fig. 2.9). The $n+$ implants are metalized and bump-bonded to the readout chip. A negative high voltage is applied to the $p+$ implanted backplane, while the $n+$ implants are kept at the ground potential. If the depletion voltage is high enough, the free charges are swep out of the sensor, leaving a non-zero electric field across the detector. When a charged particle crosses the detector volume, an average of 25000 to 30000 electron-hole pairs are created. The holes then drift towards the $p+$ implants on the backplane, while the electrons move toward $n+$ implants, creating a signal which is read out from the metalized parts.

A well-known problem of silicon detectors where the charge is collected from $n+$ structures implanted into n-type bulk is the pixel cross-talk [32]. In the barrel and end cap parts of the CMS pixel detector, the channel-to-channel isolation is performed in two different ways. In the end cap detectors, the $n+$ implants are surrounded by $p+$ implant rings (*p-stop technology*). For the barrel region, sensors

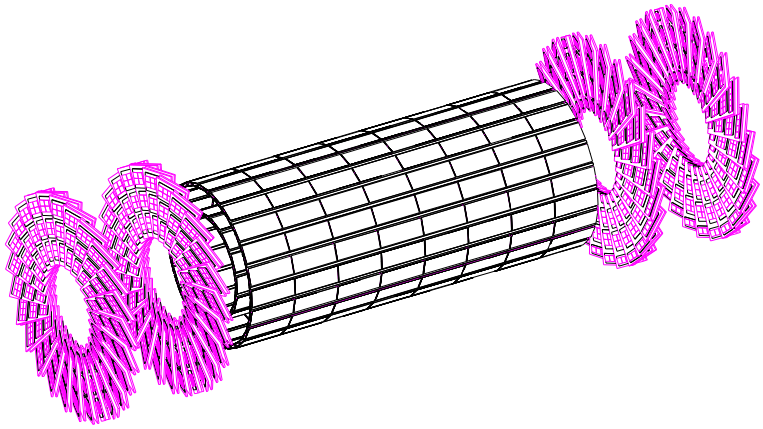

Figure 2.7: General layout of the CMS Silicon Pixel Detector.

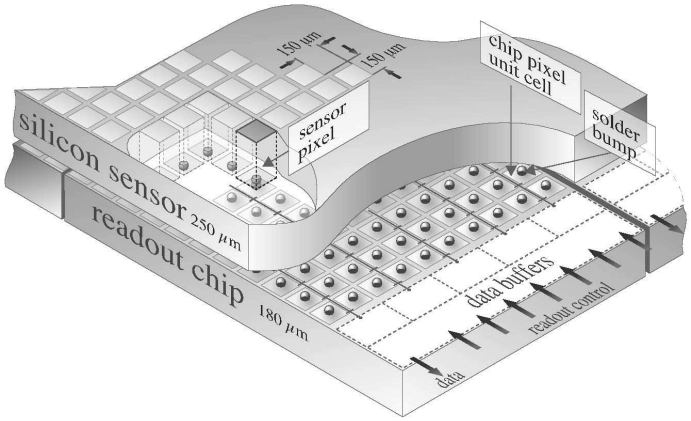

Figure 2.8: General structure of a detector element of CMS Silicon Pixel Detector.

with a uniform medium dose of p-impurities, covering the whole front surface of a detector unit (*p-spray technology*) were chosen (see Fig. 2.10).

2.2.3 Pixel beam tests at CERN

In the years 2002, 2003 and 2004 a series of pixel beam tests was performed at CERN by our group. The aim of the study was to estimate the spatial resolution of the sensors to be used in the barrel region of CMS pixel detector and to study the Lorentz drift and efficiency of charge collection in irradiated silicon devices.

The measurement was performed on both p-spray and p-stop sensors. All the test devices had 22×32 pixels with a sensitive area of 2.75×4 mm^2 and a thickness of 280 μm. Some of the devices were irradiated in a 24 GeV proton beam at CERN PS. These sensors received total particle fluences of $3.3 \cdot 10^{14}$, $8.1 \cdot 10^{14}$ and

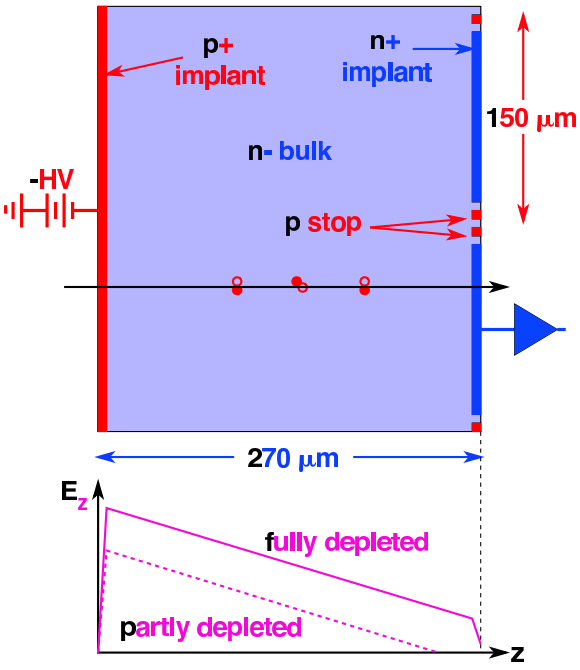

Figure 2.9: Schematic layout of the individual silicon pixel sensor for CMS. The bottom figure shows the variation of the electric field before irradiation.

$1.1 \cdot 10^{15}$ n_{eq}/cm^2. The irradiation was performed at the room temperature, while after the irradiation, the sensors were kept at $-20°$ C. Finally, the sensors were bump bonded to non-irradiated readout chips of type PSI30/AC30 [33].

The beam tests were performed at the H2 beam line of the CERN SPS accelerator, using 150-225 GeV pions. A silicon beam telescope [34] was used for precise determination of the particle hit position in the pixel detector (see Fig. 2.11). The beam telescope consists of four modules, each consisting of two perpendicularly oriented 300 μm thick single-sided silicon detectors with a strip pitch of 25 μm. The resulting resolution of the telescope is around 1 μm. The pixel sensor with the readout chip was mounted on a rotating support positioned between the second and the third module of the beam telescope. A trigger signal was generated by a silicon PIN diode. The whole setup was placed in an open Helmholtz magnet with a 3 T magnetic field parallel to the beam. The pixel sensors were cooled down to $-30°$C by means of the water cooled Peltier elements.

The angle of deflection of the charge carriers in a magnetic field from their drift path along the lines of electric field is called the Lorentz angle (Θ_L). In the beam test, the Lorentz angle in the pixel sensors was measured using the grazing angle method, illustrated in Fig. 2.12 . The particle beam, oriented parallel to the magnetic field

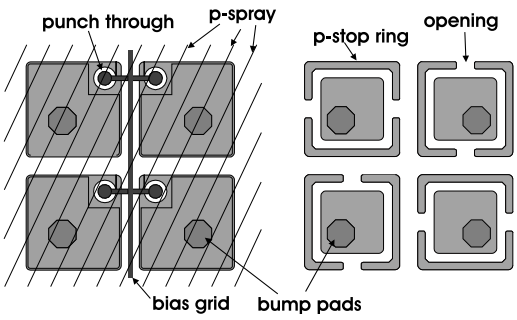

Figure 2.10: P-spray (left) and p-stop (right) designs of the CMS pixel silicon sensors.

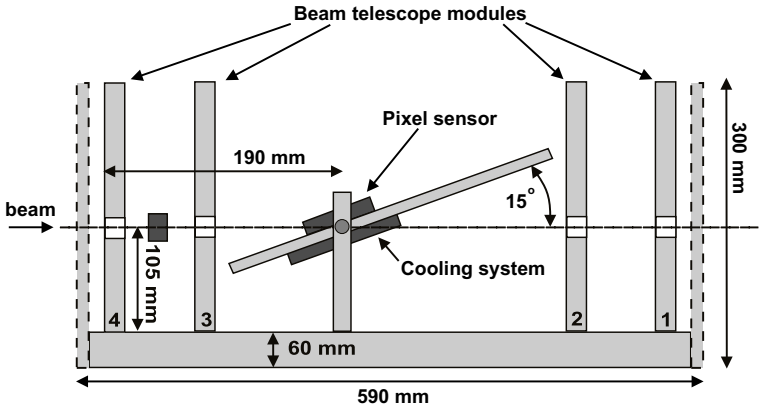

Figure 2.11: A schematic view of the silicon strip beam telescope, used in the pixel beam tests at CERN.

hits the pixel surface at the shallow angle of 15°. The value of the Lorentz angle was obtained by studying the projection of the track on the surface of the silicon pixel detector: $\tan\Theta_L = \tan\beta/\tan\alpha$. A measurement without magnetic field was used to correct for the detector misalignment with respect to the beam. The measured values of the Lorentz angle, for both irradiated and non-irradiated sensors extrapolated to a 4 T magnetic field are presented in Fig. 2.13. A strong dependence of the Lorentz angle on the bias voltage, which is only weakly affected by the irradiation or the design of the sensor, was observed. For a non-irradiated devices the Lorentz angle of 26° can be reached at a bias voltage of 100 V, while the irradiated sensors should be operated at higher bias voltages, where the Lorentz angle drops to roughly 10°. In addition, the values of the Lorentz angle measured at the temperature of −20° C are $1-2$° C larger than those measured at 10° C due to the increase of mobility of the charge carriers at lower temperatures.

The second part of the beam test measurements was dedicated to the estimation of the charge collection efficiency in the non-irradiated and irradiated sensors. In

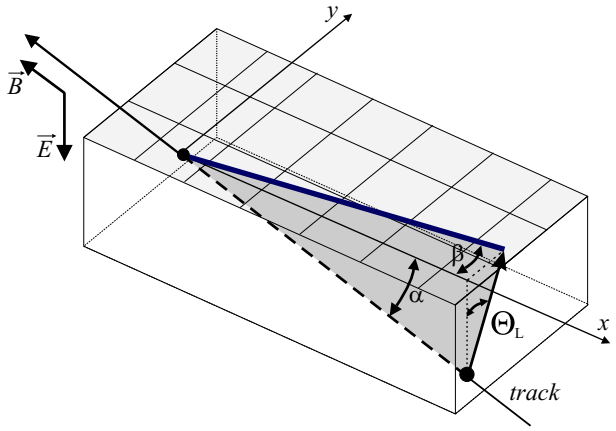

Figure 2.12: The defection of the charge carriers from their drift path due to the presence of magnetic fields, definition of the Lorentz angle and grazing angle method, used for measurement of the Lorentz angle in the beam test.

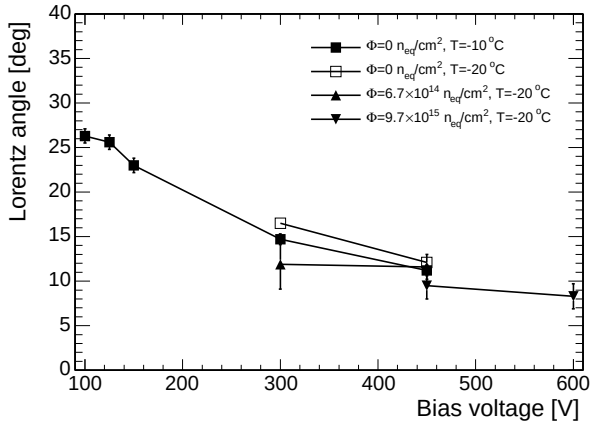

Figure 2.13: Lorentz angle as a function of bias voltage applied for 4 T magnetic field.

the non-irradiates sensors, the charge is collected uniformly across the whole sensor depth. After the irradiation, the efficiency of the charge collection decreases due to charge trapping and partial depletion of the sensor. The measurements were performed using the grazing angle method in the absence of magnetic field. The total collected charge for the p-spray design at different irradiation doses as a function of the bias voltage is shown in Fig. 2.14. The collected charge grows with the bias voltage and then reaches a plateau. It can be seen that higher irradiated sensors should be operated at higher bias voltages to enhance the charge collection efficiency.

The signal over noise ratio was also measured for the different irradiation fluences and bias voltages. The signal was defined as the average signal recorded by a hit pixel, while the standard deviation of the gaussian distribution of the signal recorded

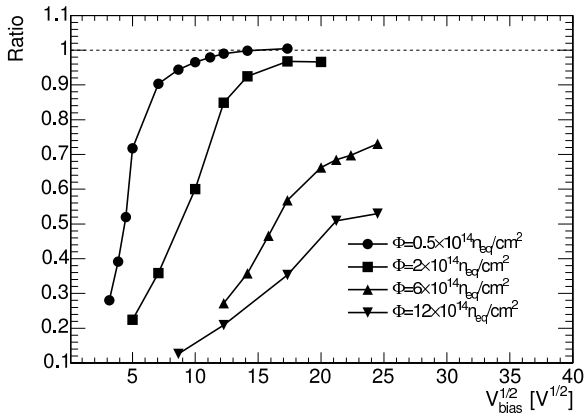

Figure 2.14: Total collected charge as function of square root of bias voltage for different irradiation doses. All the data are normalized to the charge collected in non-irradiated sensory at bias voltage of 150 V.

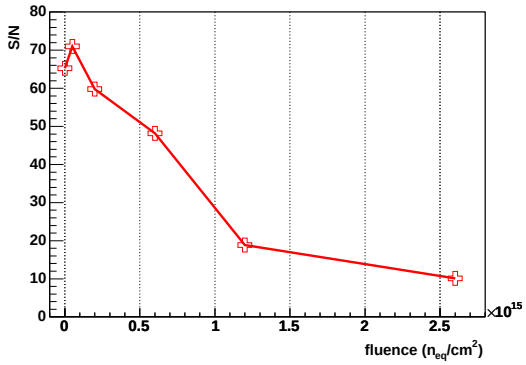

Figure 2.15: Signal to noise ratio measured with the p-spray type sensor as a function of irradiation fluence.

between spill gaps was taken as noise. The measurements were performed with tracks perpendicular to the surface of the sensor in the absence of magnetic field. In Fig. 2.15 the pixel over noise ratio averaged over the whole pixel area as a function of irradiation fluence is presented. It can be seen that even after high irradiation fluences, the signal over noise ratio stays relatively high. The highest irradiation fluence measured ($26 \cdot 10^{14}$ n_{eq}/cm^2) lies in the range of those foreseen for the LHC upgrade. At this point the signal over noise ratio drops to roughly 10 and the hit detection efficiency will probably be too low for an efficient particle tracking [35].

The dependence of charge collection on the inter-pixel position was also investigated with tracks perpendicular to the detector plane without magnetic field. The average charge, collected in the hit pixel as a function of hit position for both irra-

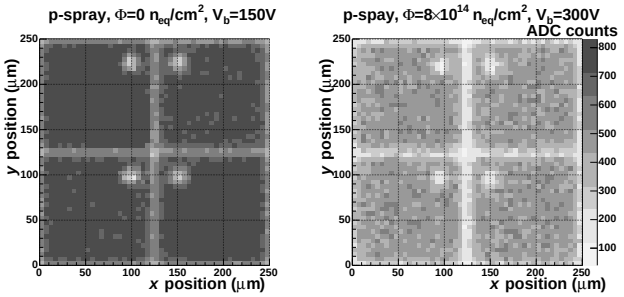

Figure 2.16: Charge collected in the non-irradiated (left) and irradiated (right) p-spray pixel sensor as function of the position of the hit.

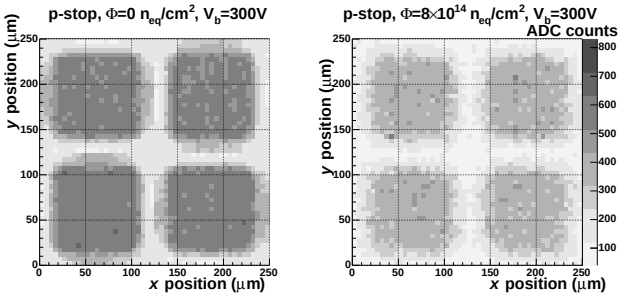

Figure 2.17: Charge collected in the non-irradiated (left) and irradiated (right) p-stop pixel sensor as function of the position of the hit.

diated and non-irradiated p-stop and p-spray sensors is shown in Fig. 2.16 and 2.17.

It can be noticed that the average pixel signal decreases after the irradiation and the area with reduced charge collection increases in case of p-stop design.

Finally, the space resolution of the silicon pixel sensors was measured for sensors with a pitch size of 125×125 μm and results were extrapolated for sensors with 100×150 μm pitch, intended to be used at CMS [36]. The position resolution was obtained comparing the position of the hit, reconstructed with the pixel detector with the one predicted with the beam telescope. In Fig. 2.18, the predicted spatial resolution of the CMS pixel sensors along the direction of the Lorentz drift is presented for different irradiation fluences and bias voltages. The predicted spatial resolution along the direction perpendicular to the Lorentz drift for different values of irradiation fluence and bias voltage is shown in Fig. 2.19. It can be seen that the spatial resolution in the direction of the Lorentz drift lies in the region 10 to 20 μm, depending on the irradiation dose. After irradiation corresponding to 4 years of operation of the LHC, the resolution is still below 20 μm and depends on the polar angle only weakly. The spatial resolution in the direction transverse to the Lorentz drift varies in the range of 20 to 40 μm and weakly depends on the irradiation dose.

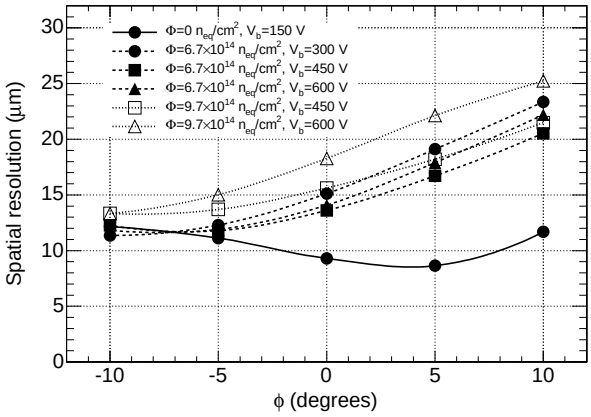

Figure 2.18: The predicted spatial resolution of the CMS pixel sensors along the direction of Lorentz drift as a function of the angle between the incident track and the direction normal to the detector surface.

2.2.4 The CMS Silicon Strip Tracker

The CMS Silicon Strip Tracker (SST) (see Fig. 2.5) is made of 15148 modules distributed over 10 barrel layers (TIB and TOB) and 12 TID and TEC disks. Most SST modules are single sided: the barrel and disk modules have the readout strips oriented along the z and radial directions respectively, allowing the readout of the $r\phi$ coordinate. To provide a measurement of the z coordinate, the first and the second layer of the TIB and the TOB, as well as the first two rings of the TID and rings 1, 2 and 5 of the TEC are instrumented with two sets of single-sided detectors, glued back-to-back with a stereo angle of 100 mrad.

Each SST module consists of a carbon fiber frame that supports the silicon detector and the readout electronics. The main characteristics of the SST modules can be summarized as follows [37]:

- Radiation resistance with no significant performance degradation after 10 years of the operation in the LHC environment.
- Shaping time of approximately 25 ns in order to reduce the electronics pile-up.
- High space granularity to ensure a robust and efficient pattern recognition: occupancy below 1%, corresponding to the strip length of approximately 10 cm.
- A pitch of 80 μm to 205 μm, depending on the detector region, to ensure the target momentum resolution ($\sim 1-2\%$ p_t at ~ 100 GeV/c).

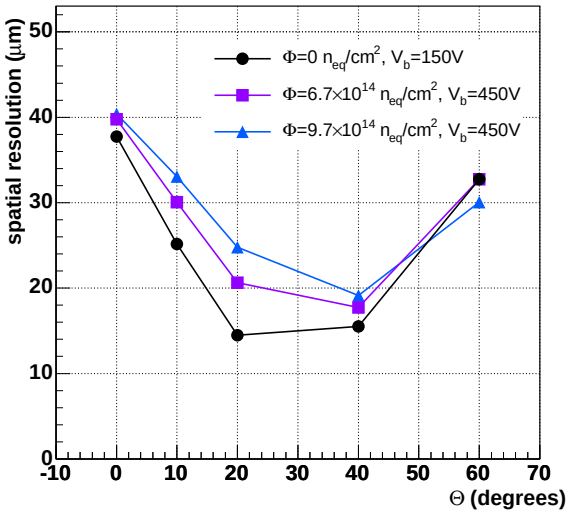

Figure 2.19: The predicted spatial resolution of the CMS pixel sensors in the direction transverse to the Lorentz drift as a function of the angle between the incident track and the detector surface.

All the SST detectors are p+-on-n microstrip sensors with AC readout. The $p+$ strip and $n+$ back plane implants are made on n-type silicon bulk.

One of the key factors influencing the resolution of the CMS SST is the material budget (thickness of the detector in radiation lengths). Despite the optimization efforts taken, the contributions from active material, support structures, electronics and services are still substantial. The material budget as a function of pseudorapidity η is shown in Fig. 2.20. This is the result of a detailed simulation of the tracker performed with the GEANT4. The parametrization of trajectories, strategies of track reconstruction in CMS and expected resolutions are discussed in Sec. 3.2.

2.2.5 The Muon Chambers

Since the study of the $B_s^0 \to (J/\psi)\phi$ decay channel relies on the identification of the $\mu^+\mu^-$ pairs, the CMS muon system is briefly discussed in the current section. The CMS muon system (see Fig. 2.21) uses three different types of gaseous detectors to detect muons and measure their trajectories. The choice of the detector technology has been driven by the large surface to cover and by the different background environments in the different regions of the CMS detector. One of the main background sources are low energy electrons, which follow the capture of slow neutrons in the material near or inside the muon chambers. These neutrons originate from hadronic cascades starting elsewhere in the detector or in the accelerator itself. According to

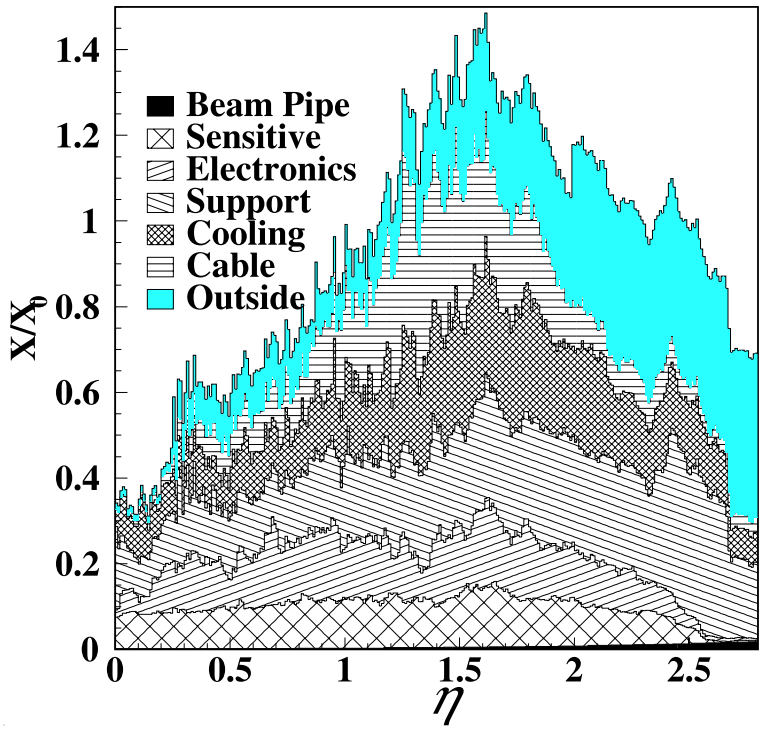

Figure 2.20: Material budget of the CMS Silicon Strip Tracker as a function of pseudorapidity.

the simulations performed [38], the end-cap muon chambers are mostly affected by the background.

In the barrel region ($|\eta| < 1.2$), where the neutron induced background is negligible and the muon rate is below (1 Hz/cm^2), Drift Tube chambers (DT) are used. In the end cap regions, where both muon rate and the neutron background is high ($R(\mu) \leq 10$ Hz/cm^2, $R(n,\gamma) \sim 10$ Hz/cm^2), Cathode Strip Cambers (CSC) are used [39]. Finally, Resistive Plate Chambers (RPC), dedicated to the trigger are used in both barrel and end caps up to $|\eta| < 2.1$. The general layout of the CMS muon chambers is presented in Fig. 2.21.

The reconstruction of muon tracks in the CMS muon detector is performed using the Kalman filter algorithm. The initial trajectory seeds are taken form the output of the L1 trigger or created internally from correlated patterns of hits inside muon chambers. The overall resolution of the CMS muon system, defined as $\frac{\sigma_{1/p_t}}{1/p_t}$ reaches 10% in the barrel region ($|\eta| < 0.8$), 15% in the overlap region ($0.8 < |\eta| < 1.2$) and 16% in the end caps ($1.2 < |\eta| < 2.1$) [39][5].

[5]The resolutions are estimated for the muons coming from the $W \rightarrow \mu\nu$ decay. The quoted values include the information of the muon chambers only, information from the central tracker is not included.

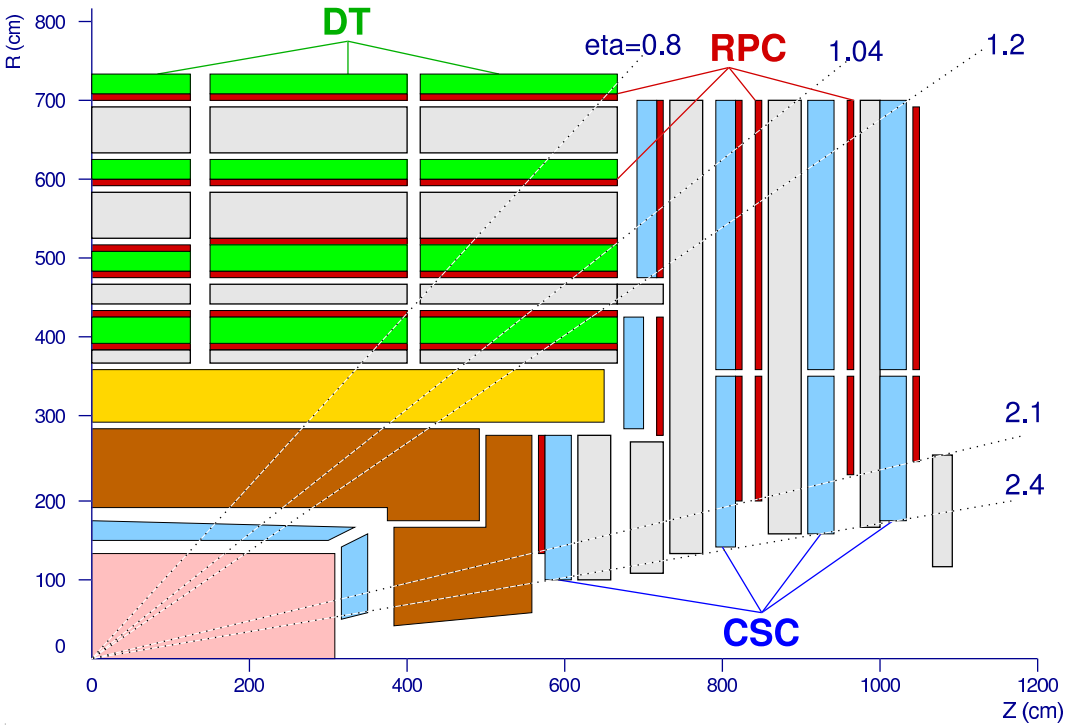

Figure 2.21: General layout of the CMS muon chambers (Longitudinal cross section). DT = Drift Tubes, RPC = Resistive Plate Chambers, CSC = Cathode Strip Chambers.

2.2.6 Event trigger architecture and performance

As described in Sec. 2.1, the bunch crossing frequency of the Large Hadron Collider is 40 MHz. At the high luminosity of 10^{34} cm^{-1}s^{-1} each of these crossings will result in some 20 proton-proton interactions, producing approximately 1 Mb of raw data. This data flow is significantly higher than the present data storage capabilities [40], which is of the order of $\mathcal{O}(10^2)$ Mb/s for magnetic tapes.

The CMS Collaboration has chosen a two-step trigger and data acquisition system, designed to inspect the detector output at full bunch crossing frequency and to store the selected events at the maximal allowed storage rate of 100 Hz. The schematic layout of the CMS DAQ/Trigger system is presented in Fig. 2.22. The first level trigger (L1) is a hardware trigger designed to reduce the rate of accepted events to less than 100 kHz. It is based on the identification of muons, electrons, photons, jets and missing transverse energy. The second level trigger or HLT (High Level Trigger) is a software trigger, designed to reduce the maximum L1 output rate of to the final output rate of 100 Hz. The High Level Trigger software is supposed to run on a dedicated computing farm composed of commercial processors. On average, the High Level Trigger is given approximately 200 ms to make a decision on any

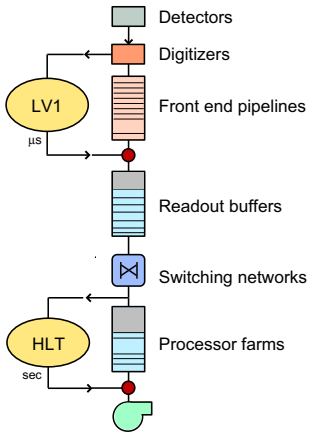

Figure 2.22: Data flow in the DAQ/Trigger.

particular event. The bandwidth of 100 Hz should be shared between all the channels of interest. The complete description of the CMS online software architecture and performance can be found in [40]. A possible HLT strategy suitable for selection of the $B_s^0 \to (J/\psi)\phi \to \mu\mu KK$ decay channel is discussed in Sec. 4.2.

Chapter 3

Event reconstruction and kinematic fitting techniques

> The faculty of re-solution is possibly much invigorated by mathematical study, and especially by that highest branch of it which, unjustly, and merely on account of its retrograde operations, has been called, as if par excellence, analysis.
>
> *Edgar Allan Poe, The Murders In The Rue Morgue (1841)*

As shown in the previous chapters, the observation of mixing and CP-violation in the system $B_s^0 - \bar{B}_s^0$ system requires a high resolution on the parameters of the B_s^0 meson reconstructed in the detector. The present average value of the mean lifetime of the B_s^0 meson is $\tau_s = 1.461 \pm 0.057$ ps [41]. The observation of the mean lifetime with an accuracy of 10% requires a resolution of approximately 44 μm on the proper decay length ($c\tau$ in the rest frame of the B_s^0 meson). The mean energy of the B_s^0 mesons produced at the LHC can be estimated as approximately 24.5 GeV (see Sec. 4.1). The mean flight path of the B_s^0 meson in the frame of the CMS detector can be therefore estimated as approximately 1.9 mm.

The present experimental lower limit on the difference of masses of heavy and light mass eigenstates of the B_s^0 meson is $\Delta m > 14.4$ ps^{-1} at 95% C.L. [6]. However recent experimental results suggest this value to be even larger [7]. For a mass difference of 14.4 ps^{-1}, the period of oscillation can be estimated as $T = 0.43$ ps, which corresponds to the flight path of $L^{\rm pr} = 130\mu$m in the rest frame of the B_s^0 meson or approximately $L^{\rm lab} = 560$ μm in the detector frame. In this case the resolutions of 13 μm on the proper decay length and of 56 μm on the flight path in the detector frame is required to observe the $B_s^0 - \bar{B}_s^0$ oscillations directly with a

precision of 10%. Obviously, for higher mass differences and hence faster oscillations, a higher accuracy is required.

The experimental resolution of the reconstructed parameters depends equally on the resolution of the detectors and the accuracy with which these parameters are reconstructed from the detector information. The choice of algorithms for track and vertex reconstruction is crucial. The result of the reconstruction may be improved significantly, applying an appropriate set of kinematic constraints.

In the current chapter, a review of the reconstruction and kinematic fitting techniques relevant for the study of the $B_s^0 \to (J/\psi)\phi \to \mu^+\mu^- K^+ K^-$ decay channel is given and their main properties are discussed. Emphasis will be given to vertex reconstruction method using the Kalman filter and kinematic fitting using Least Mean Squares with Lagrange multipliers, to which a major contribution was done during the current study.

3.1 Simulation and reconstruction software of CMS

The CMS software packages relevant for further discussion of development and implementation of the reconstruction and kinematic fitting techniques are the following:

- **PYTHIA** [42]: It is a Monte Carlo event generator, dedicated to the simulation of the Standard Model processes as well as a large variety of processes beyond the Standard Model. PYTHIA can be regarded as the default event generator in CMS. It was exclusively used for production of all the Monte Carlo data samples mentioned hereafter[1].

- **OSCAR** [44, 45] (Object oriented Simulation for CMS Analysis and Reconstruction): It is the C++ application for detector simulation. OSCAR takes the output of the event generator as input and traces particles through the CMS detector. Based on the Geant4 [46] simulation toolkit, it provides a comprehensive description of passage of particle through matter and contains the most detailed description of the detector currently available.

- **ORCA** [47] (Object oriented Reconstruction for Cms Analysis): It is the reconstruction package responsible for the complete chain of event reconstruction from data acquisition to physics analysis. ORCA is used for both online (High Level Trigger) and offline reconstruction and selection of events.

[1]The $B_s^0 \to (J/\psi)\phi \to \mu^+\mu^- K^+ K^-$ events were produced with the dedicated SIMUB [43] generator, which uses PYTHIA for production and fragmentation of the $b\bar{b}$ pairs.

3.2 Track reconstruction at CMS

Due to the complexity of the CMS tracker, which consists of thousands of detector units, and the large multiplicity of tracks in high-energy *pp* collisions at the LHC, the choice of a single algorithm for track reconstruction in CMS may be problematic. It is more likely that in a highly complex experimental environment such as the CMS tracker, several different track reconstruction algorithms, each optimized for a specific task may be needed.

The basic algorithm for track reconstruction in CMS is a combinatorial search using the Kalman filter [48] technique (denoted hereafter as Combinatorial Kalman Filter - CKF). However, due to the flexibility of the CMS track reconstruction framework, more advanced algorithms such as a Deterministic Annealing Filter or a Multi Track Filter (see [40] and references therein) were successfully implemented as well. In addition, a Gaussian-Sum Filter was developed for the reconstruction of electrons, where a non-Gaussian distribution of energy loss due to bremsstrahlung is considered [49].

3.2.1 Kalman filter technique

The Kalman filter [48] is mathematically equivalent to a global Least Mean Squares (LMS) minimization, which is the optimal estimator when the model is linear and all random noise is Gaussian. In that case, the estimator is unbiased and has minimum variance, residuals and pulls of estimated quantities have Gaussian distributions. For non-linear models or non-Gaussian noise, it is still the optimal linear estimator.

Contrary to a global LMS minimization [14], where the parameters of the trajectory are estimated globally, on a preselected set of hits, in the Kalman filter measurements are added sequentially. The Kalman filter allows therefore for the inclusion of the material effects, such as energy loss and multiple scattering. It also integrates track fitting with track finding, allowing for a decision, whether particular hit belongs to the current track. Since the total χ^2 of this recursive fit is equal to the sum of the χ^2 contributions of the individual steps[2], the latters can be used to test whether a measurement follows the model. The possibility to remove unwanted measurements from the estimate is also provided with the so-called *reverse* filter.

The global LMS fit requires a single inversion of the full covariance matrix of all measurements of dimension $(n_{\text{meas}} \cdot n_{\text{param}} \times n_{\text{meas}} \cdot n_{\text{param}})$, where n_{meas} is the total number of measurements and n_{param} is the number of parameters describing each

[2]The step of the Kalman filter is defined as the update of the estimate with a single measurement.

measurement[3]. Contrary to that, a fit with the Kalman filter requires inversion of the covariance matrix of a single measurement at each step. The size of this matrix is $(n_{\text{param}} \times n_{\text{param}})$ [4]. As the CPU time required for a matrix inversion scales as n^3, where n is the dimension of the matrix, the Kalman filter is clearly computationally more efficient than a Global LMS.

In the Combinatorial Kalman Filter the reconstruction of the trajectory of the charged particle is subdivided in the four following steps: *trajectory seeding*, *trajectory building*, *trajectory cleaning* and *trajectory smoothing*.

At the seeding step of the track reconstruction, the initial trajectory parameters and their errors are estimated. In the Tracker, trajectory seeds are generated in the Pixel and/or Silicon Strip detector[5]. First, a pair of inner detector planes is selected and all the hits in the outer plane are reconstructed and stored (see Fig. 3.1). Then,

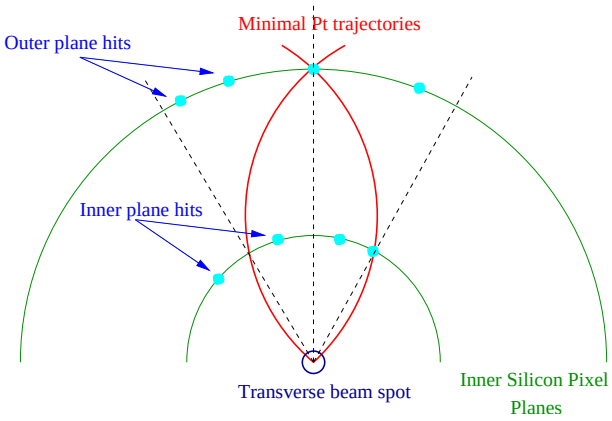

Figure 3.1: Trajectory seeding using the inner layers of CMS Tracker.

for each of the outer hits, the hits in the inner plane, compatible with a minimum transverse momentum and transverse size of the beam spot, are found. Using this information (transverse beam profile and a pair of reconstructed hits) the parameters of trajectories (trajectory states) are estimated. Large uncertainties are added to these parameters in order not to bias the further fit.

At the trajectory building step, the reconstructed trajectory candidates are propagated to the next surface of the detector according to the equations of motion

[3]For instance, the reconstruction of track using 5 hits, each described by 2 coordinates in a detector plane requires the inversion of the covariance matrix of the size (10×10).

[4]Here the reconstruction of track using 5 hits requires 10 inversions of covariance matrices of dimension (2×2).

[5]An exception should be made for the case of muon or electron reconstruction, where the information from the muon chambers or electromagnetic calorimeter is used.

of a charged particle in a magnetic field, accounting for energy losses and multiple scattering (see [40] and references therein). After that, hits compatible with the propagated trajectory state are searched in this surface in a narrow window around the crossing point. The actual size of the search window is defined by the uncertainty on the momentum of the trajectory and uncertainties arising from the multiple scattering during the propagation of the trajectory. For each reconstructed hit compatible with the trajectory, a new trajectory candidate is created by updating the current trajectory candidate with this hit using the Kalman filter. Several new trajectory candidates can thus be formed. This sequence of propagating candidates to the next detector planes, updating them with compatible hits and creating new candidates, is then applied till the end of the detector. To avoid bias, all trajectory candidates are grown in parallel.

In addition, to account for detector inefficiencies, so-called *invalid hit* is added to every trajectory. The trajectory is then propagated to the next plane and a fixed χ^2 penalty is added to the total χ^2 of the trajectory candidate. In order to speed up the reconstruction process, only a limited number of trajectory candidates are propagated. It is easy to see that due to the combinatorial approach to trajectory finding, a number of trajectory candidates will share a significant number of hits (for instance, trajectories splitting on the last surface of the detector only). At the cleaning step an obtained set of trajectory candidates is cleaned for ambiguities, using the number of identical hits as a criterion[6].

At the last (smoothing) step of track reconstruction, the information from the last surface of the detector is propagated back to the seed, updating states of trajectory on each surface with the full knowledge. After the smoothing step, a final set of consistent trajectories is obtained.

3.2.2 Reconstruction efficiency and resolutions

To study the quality of the track reconstruction with the Combinatorial Kalman Filter, the following trajectory parametrization can be used: $(p_t, d_0, z_0, \phi, \cot\theta)$, where p_t is the transverse momentum, d_0 and z_0 are transverse and longitudinal coordinates of the point of closest approach of track with respect to the beam axis, and ϕ and θ represent the azimuthal and polar angles of track at this point (see Fig. 3.2). The resolutions of these trajectory parameters are presented in the Fig. 3.3 and 3.4.

[6]The cut of 50% of identical hits is normally used for this purpose

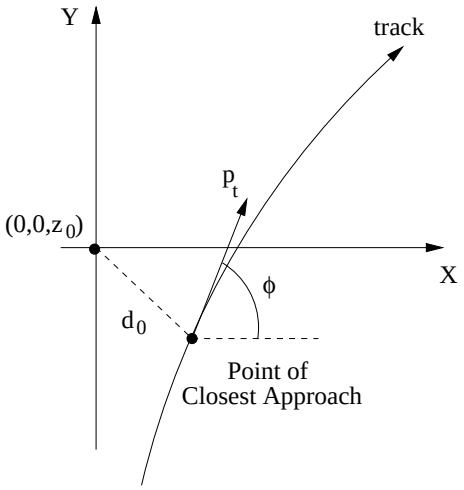

Figure 3.2: Trajectory parametrization used to study the quality of the track reconstruction with Combinatorial Kalman Filter.

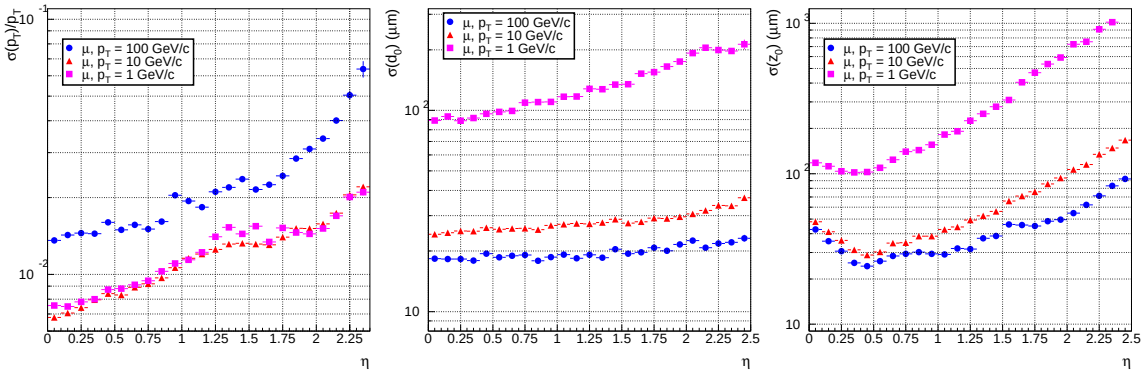

Figure 3.3: Resolutions on the parameters of the muon trajectories, reconstructed in the using Combinatorial Kalman Filter as a function of pseudorapidity. **Left:** transverse momentum. **Middle:** transverse impact parameter. **Right:** longitudinal impact parameter.

In the case of muons with $p_t = 100$ GeV, a resolution of $1 - 2\%$ can be obtained for the transverse momentum in the central region of the tracker ($|\eta| < 1.7$). The degradation of the resolution around $|\eta| = 1.0$ is due to the gap between the barrel and end cap of the tracker. The degradation in the region $|\eta| > 1.1$ is due to the lower hit resolution in the forward tracker rings and due to the lower lever arm with respect to the barrel layers. The resolution on the transverse momentum of the muons with lower p_t is dominated by multiple scattering and reflects the amount of material in the tracker [40].

At high momenta, the d_0 and z_0 resolutions are nearly constant, dominated by the hit resolution of the first hits in the pixel detector. At lower momenta, the resolutions are degraded by multiple scattering.

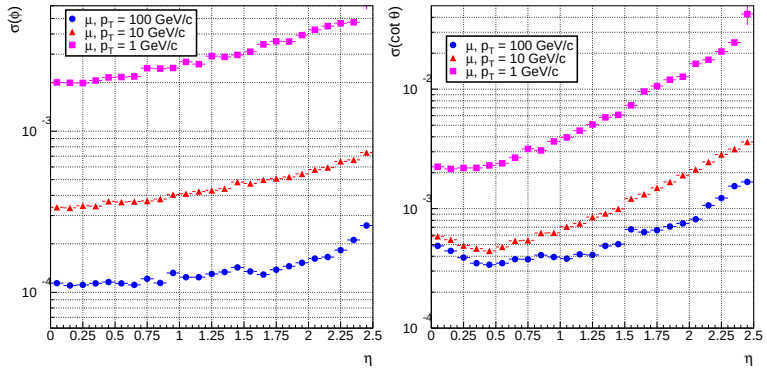

Figure 3.4: Resolutions on the parameters of the muon trajectories, reconstructed in the using Combinatorial Kalman Filter as a function of pseudorapidity. **Left:** azimuthal angle. **Right:** polar angle.

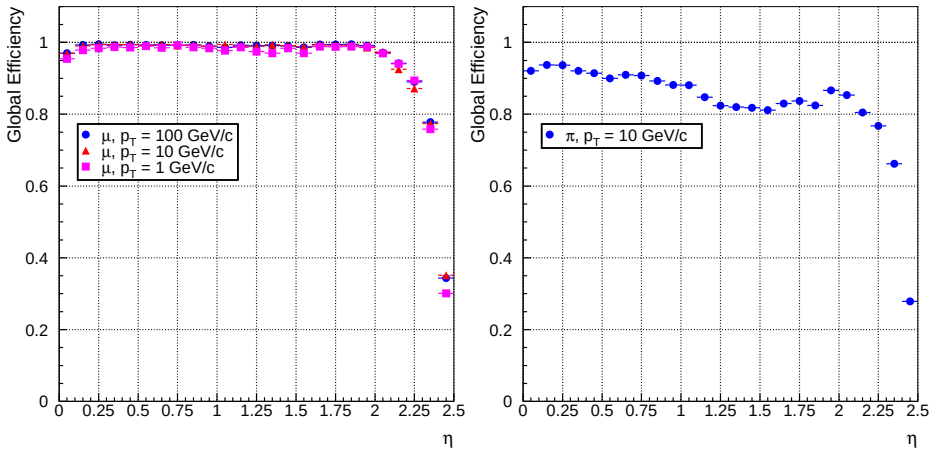

Figure 3.5: Global efficiency of track reconstruction with Combinatorial Kalman Filter as a function of pseudorapidity. **Left:** muons. **Right:** pions.

The global efficiency of reconstruction of muon tracks with the CKF is presented in the Fig. 3.5 (left). It can be seen that the reconstruction is fully efficient for muon tracks of all p_t in almost the full coverage of the tracker. The reconstruction efficiency degrades in the very forward region of due to the lack of coverage of the end cap disks.

For comparison, the global reconstruction efficiency of pion tracks with with the CKF is presented in Fig. 3.5 (right). The reconstruction efficiency of pions with the transverse momentum of 10 GeV reaches 80% to 90% in the barrel region and degrades rapidly in the end caps. The difference in the reconstruction efficiencies of muons and pions of the same transverse momentum is due to the hadronic interaction of pions with the material of detector. The efficiency of reconstruction of pion tracks

degrades significantly for pions with lower momenta. For instance, 20% of 1 GeV pions do not reach the outer layer of the tracker.

3.3 Vertex reconstruction at CMS

A precise reconstruction of primary and secondary vertices is equally important for both online (high-level trigger) and offline reconstruction and selection of events. The task of vertex reconstruction can be subdivided in two parts:*vertex finding* and *vertex fitting*. The task of vertex finding is to decide whether a particular set of tracks belongs to the same vertex. The vertex fitting deals with estimation of the vertex position from a set of trajectories and refit of these trajectories with the knowledge of vertex.

The basic algorithm for vertex finding in CMS is the so-called *Principal Vertex Reconstructor* [40]. It is a recursive vertex finding algorithm, which fits all the tracks to a common vertex, removes incompatible tracks and searches for additional vertices in the set of tracks discarded in the previous iteration. This technique is based on the vertex fitting with the Kalman filter algorithm and rejects incompatible tracks according to a fixed χ^2 cut.

During the year 2002, we have developed a vertex fitting algorithm using the Kalman Filter technique and implemented it in the ORCA reconstruction program (called hereafter Kalman Vertex Fitter - KVF) [50]. The details mathematical of the mathematical approach, implementation and results are presented in the next section. A brief discussion of the other algorithms for vertex fitting implemented in CMS reconstruction program is given in the Sec. 3.3.2.

3.3.1 Kalman Vertex Fitter

As stated above, in a vertex fit the unknown vertex position is to be estimated from a set of reconstructed tracks. The parameter vectors p_k and covariance matrices v_k (for tracks $k = 1, ..., n$) describing the tracks to be fitted to a common vertex are considered as the *virtual measurements*, obtained in a track reconstruction phase. The quantities to be estimated (the *state vector*) are the vertex position x and, for each track, its momentum q_k at the vertex. Initially, the state vector consists only of the prior information on the vertex position x_0 and its covariance matrix C_0.

The dependence of the track parameters on the state vector (x, q_k) is given by the so-called *measurement equation*:

$$p_k = h_k(x, q_k) + \epsilon_k, \tag{3.1}$$

where h_k is the functional dependence of track parameters on the state vector[7] and ϵ_k is the measurement error: $cov(\epsilon_k) = V_k$.

As the track model is usually non-linear, a first-order Taylor expansion of h_k at some convenient point $(x_e, q_{k,e})$ is used:

$$h_k(x_k, q_k) \simeq h_k(x_{k,e}, q_{k,e}) + A_k(x_k - x_e) + B_k(q_k - q_{k,e}) = c_{k,e} + A_k x + B_k q_k, \quad (3.2)$$

where $A_k = [\partial h_k/\partial x]_e$ and $B_k = [\partial h_k/\partial q_k]_e$ are the derivative matrices at the expansion point.

As mentioned above, the Kalman filter is an iterative fit, i.e. the estimate of the vertex is updated with one track at the time. The Kalman filter describes how to add a new track k to the vertex already fitted with $k-1$ tracks [48]. The smoothing step of the fitter consists of refitting the parameters of the input tracks with the knowledge of their common vertex. The mathematical details of this procedure can be found in [48, 51].

A simplified version of the Kalman filter for vertex fitting is proposed in [52] and [53], where the trajectories are approximated by straight lines in the vicinity of the vertex (so-called *Linear Vertex Fitter* - LVF). This approach simplifies the algorithm and in principle reduces the amount of mathematical operations required in the fitting procedure. It does not nevertheless allow the input tracks to be refitted with the additional constraint of the vertex. This simplified algorithm was developed and implemented in ORCA [53].

In order to fully use the features, provided by the Kalman filter, we developed a new Kalman Vertex Fitter where the trajectories are no longer linearized. Here the charged track is represented by a helix, which makes the model formally more precise.

The track model

It should be noted that the Kalman filter is parametrization-independent, i.e. it does not depend on a specific parametrization of data. In the current implementation of the KVF, the description of the trajectory in the neighborhood of the vertex is provided by the so-called "perigee" parametrization [52]. The trajectory is described by 5 parameters, defined at the point of the closest approach of the trajectory (in the transverse plane) to a reference point. These parameters are (see Fig. 3.6):

[7] The mathematical formulation of the Kalman filter does not depend on the particular parametrization chosen for the track model. The particular case of use of the helix parametrization is discussed below.

- ϵ_p: signed transverse distance of the point of the closest approach. By convention, the sign is positive if the reference point is at the left of the point of closest approach.

- z_p: longitudinal distance of the point of closest approach.

- θ: polar angle of the momentum vector at the point of closest approach.

- ϕ_p: azimuthal angle of the momentum vector at the point of closest approach.

- ρ: signed transverse curvature of trajectory. The sign of transverse curvature is equal to the sign of electric charge of the particle.

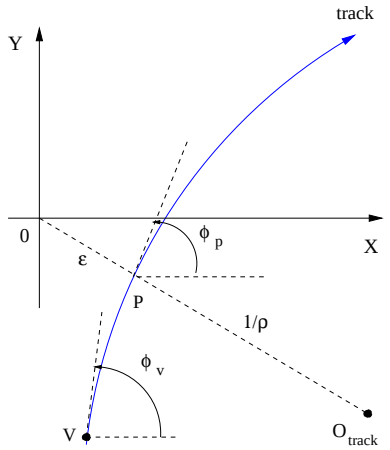

Figure 3.6: A "perigee" parametrization of helix [52].

With this parametrization, the equation of motion of a charged particle in a solenoidal magnetic field parallel to the z-axis are:

$$\begin{aligned} x(\phi) &= x_r + \epsilon_p \sin\phi_p + \rho^{-1}(\sin\phi - \sin\phi_p), \\ y(\phi) &= y_r - \epsilon_p \cos\phi_p - \rho^{-1}(\cos\phi - \cos\phi_p), \\ z(\phi) &= z_r + z_p + \frac{\phi - \phi_p}{\rho}\cot\theta, \end{aligned} \tag{3.3}$$

where $\vec{r_r} = (x_r, y_r, z_r)$ is the reference point and the parameter ϕ is the azimuthal angle of the momentum vector at the considered position. In this case, $\rho = -0.29979q \cdot B_z/p_t = h/R_h$, where R_h is the radius of the helix, h is the sign of the curvature and B_z is the longitudinal component of the magnetic field.

The dependence of the track parameters ($\vec{p} = (\rho, \theta, \phi_p, \epsilon, z_p)$) on the position of the vertex $\vec{r_v} = (x_v, y_v, z_v)$ and momentum of the track at the vertex $\vec{q_v} = (\rho, \theta, \phi_v)$ (the measurement equation for the perigee parametrization) is then:

$$\begin{aligned} \epsilon &= \rho^{-1} - hS, \\ \phi_p &= -h \cdot \mathrm{sign}(X) \cdot \mathrm{acos}\frac{hY}{S}, \end{aligned}$$

$$\phi_p = \begin{cases} \mathrm{asin} - \frac{hX}{S} & \text{if } hY > 0 \\ \pi - \mathrm{asin} - \frac{hX}{S} & \text{if } hY < 0 \end{cases} \tag{3.4}$$

$$z_p = z_v - z_p - \frac{\phi_v - \phi_p}{\rho} \cot\theta,$$

where $X = x_v - x_r - \rho^{-1}\sin\phi_v$, $Y = y_v - y_r + \rho^{-1}\cos\phi_v$ and $S = \sqrt{X^2 + Y^2}$. The parameters θ and ρ are constant along the helix.

In a homogeneous magnetic field, the equations 3.4 are exact, i.e. no approximations or expansions are done, and can easily be understood geometrically, bearing in mind that X (resp. Y) is the distance between the reference point and the center of rotation of the helix on the x-axis (resp. y-axis). S is the distance between the reference point and the center of rotation of helix in the transverse plane.

For neutral particles the trajectory is a straight line. In the perigee parametrization, the transverse curvature is replaced with the inverse of the transverse momentum of the particle ($1/p_T$).

Expansion and choice of reference point

After the track model is built, an first-order Taylor expansion of the dependence of the track parameters on the vertex position and momentum of the track at the vertex should be performed at some expansion point (x_e, q_e) (see Eq. (3.2)). The result of calculation of Jacobians $A = \frac{\partial(\rho,\theta,\phi_p,\epsilon,z_p)}{\partial(x_v,y_v,z_v,)}$ and $B = \frac{\partial(\rho,\theta,\phi_p,\epsilon,z_p)}{\partial(\rho,\theta,\phi_v)}$ can be found in [50].

The expansion point (x_e, q_e) should be chosen such that the approximation errors due to the Taylor expansion are small. Moreover, in order to minimize the propagation errors, the expansion point should be chosen reasonably close to the vertex. In the current implementation we have chosen the expansion point to be the point of closest approach of tracks to the reference point.

As mentioned above, the Kalman filter requires an initial estimate of vertex state. In case an initial guess on the vertex position and its covariance matrix is present, this information can be included in the fit as a *prior* knowledge. This prior position is

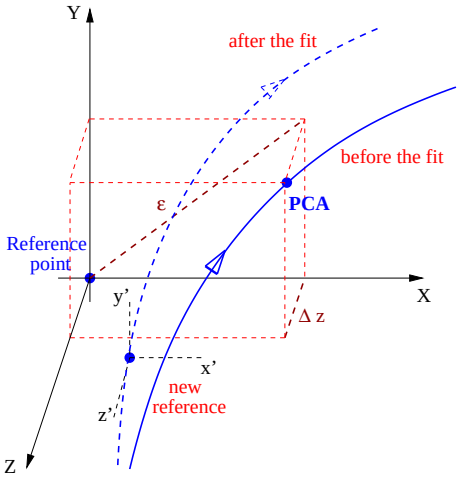

Figure 3.7: Vertex fitting and smoothing of the tracks.

then used as the reference point in the first iteration of the fit. If no such information is provided, the reference point is deduced by an algorithm provided by the user. In case several iterations have to be performed to reach the convergence, for each new iteration, the position of the vertex found in the previous iteration is used as reference point.

After the convergence is reached, the parameters of the input tracks can (optionally) be refitted with the knowledge of the vertex position. The process and the result of the iterative vertex fit with smoothing are described schematically in Fig. 3.7. The details of actual implementation of the Kalman Vertex Fitter in the ORCA reconstruction program can be found in [50].

Results

The properties of the Kalman Vertex Fitter were tested using Monte Carlo generated samples of the decays $H^0 \rightarrow Z^*Z \rightarrow 4\mu$ (with Higgs masses of 130 GeV/c^2 and 500 GeV/c^2), $B_s^0 \rightarrow (J/\psi)\phi$ and $B_s^0 \rightarrow \mu\mu$. The resolutions on the coordinates of reconstructed vertices and the execution time of the algorithms were estimated and compared to those obtained with the linear KVF.

It was noticed that the resolutions of the coordinates of the primary and secondary vertices, are nearly identical for both LVF and KVF, and dominated by the quality of track parameters. However, the typical CPU time of the KVF is almost twice smaller than the typical time of the linear fit [50]. This was traced to the fact that in case of linear model, the track parameters were computed at the point of closest approach *in three dimensions* to the linearization point, whereas in case of Kalman

Vertex Component	σ (μm)	Mean (μm)	95% coverage (μm)	Pull	$P(\chi^2)$
Primary x	44.1	0.531	176	1.11	0.436
Primary z	54.3	0.73	223	1.07	0.436
Secondary x	54.8	0.232	164	1.08	0.485
Secondary z	73.8	-0.699	470	1.08	0.485

Table 3.1: Resolutions, coverages, pulls and χ^2 probabilities of the $B_s^0 \to (J/\psi)\phi$ primary and secondary vertices reconstructed with Kalman Vertex Fitter.

Vertex Fitter the *transverse* point of closest approach was used. Indeed, while the problem of finding the 3D point of closest approach has no analytical solution and corresponding numerical algorithms are very slow, such an analytical solution exists for the transverse point of closest approach. In addition, the LVF does not allow for the smoothing of the input tracks and thus for the calculation of the full track-to-track covariance matrix. The latter quantity is required for kinematic fitting (see below). Accounting for all these facts, the decision was taken to use the use the KVF as a base method for vertex reconstruction in CMS.

The results of the reconstruction of primary and secondary vertices of $B_s^0 \to (J/\psi)\phi \to \mu\mu KK$ decay with Kalman Vertex Fitter are summarized in the Tab. 3.1. There the mean values and widths of distributions of residuals and pulls are presented. The 95% coverages[8] of distributions of residuals and the probabilities of the χ^2 of fits are also quoted.

The corresponding distributions of residuals, pulls and χ^2 probability are shown in Fig. 3.8-3.11. The resolutions on the x and z coordinates of the secondary vertex are ~ 55 and 74 μm respectively. The distributions of pulls are of Gaussian shape with a standard deviation close to 1, indicating correct estimation of errors [48]. The distributions of the probability of the χ^2 are flat over the whole range, as expected for gaussian-distributed data [14], with a significant peak at very low probabilities. This effect is due to the non-gaussian tails in the distributions of track parameters pulls [50]. It should be noted that in a physics analysis, the candidates with a low χ^2 probability, while having perfectly reconstructible tracks and vertices, would be rejected. The average CPU time of the Kalman Vertex Fitter is ~ 0.25 ms per track,

[8]The coverage is one of characteristics describing a goodness of the fit. The 95% coverage represents the half-width of the symmetric interval covering 95% of the residual distribution. It allows also to estimate the amount of tails in a distribution, since for the Gaussian distribution the 95% coverage corresponds to twice the standard deviation.

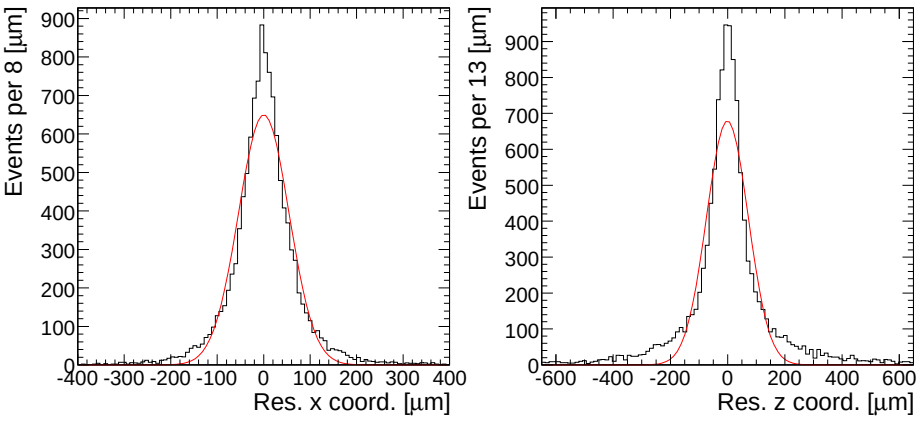

Figure 3.8: Distribution of coordinate residuals (**left:** x, **right:** z) of the $B_s^0 \to (J/\psi)\phi$ secondary vertex, reconstructed with the Kalman filter method.

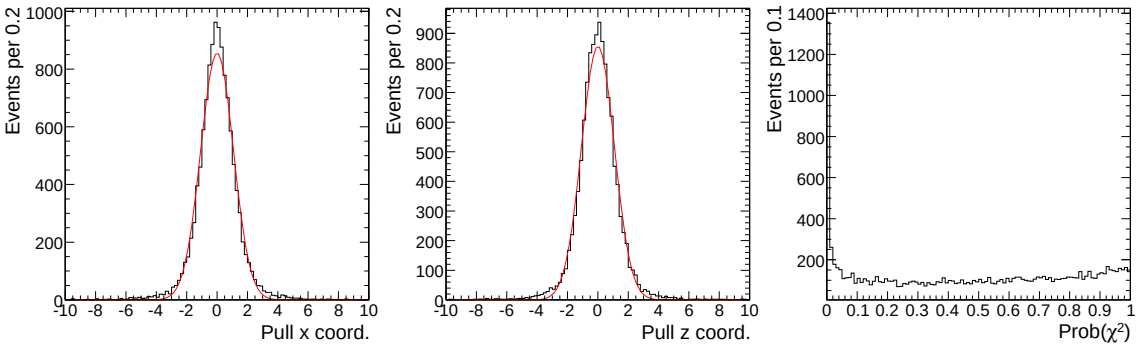

Figure 3.9: Distribution of coordinate pulls (**left:** x, **middle:** z) and χ^2 probability (**right**) of the $B_s^0 \to (J/\psi)\phi$ secondary vertex, reconstructed with the Kalman filter method.

which makes the use of this algorithm possible for both offline reconstruction and high level trigger. The complete description of performed test and obtained results can be found in [54].

3.3.2 Other techniques

Apart from the Kalman Vertex Fitter discussed in the previous section, several other techniques suitable for vertex reconstruction were developed and implemented in ORCA. For instance, the Adaptive Vertex Fitter (AVF) [54] was implemented. This technique incorporates both vertex fitting and vertex finding. The AVF is an iterative re-weighted fit which down-weights tracks according to their reduced χ^2 distance to the vertex. The track weights are computed according to the following

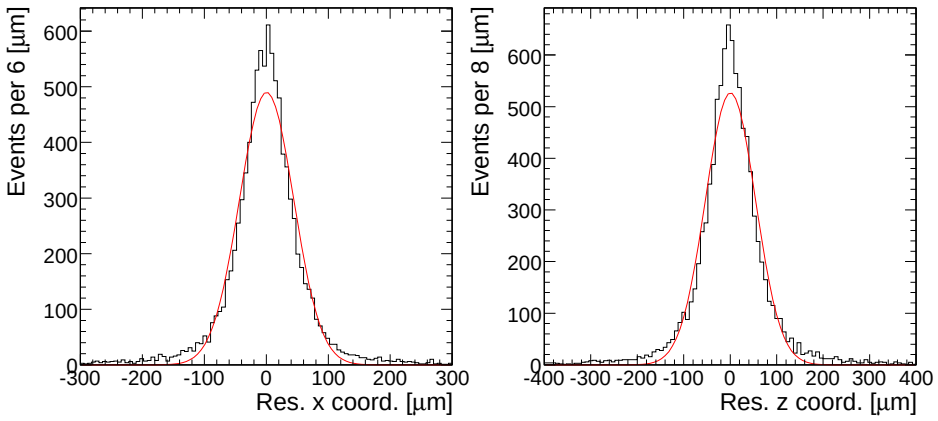

Figure 3.10: Distribution of coordinate residuals (**left:** x, **right:** z) of the $B_s^0 \to (J/\psi)\phi$ primary vertex, reconstructed with the Kalman filter method.

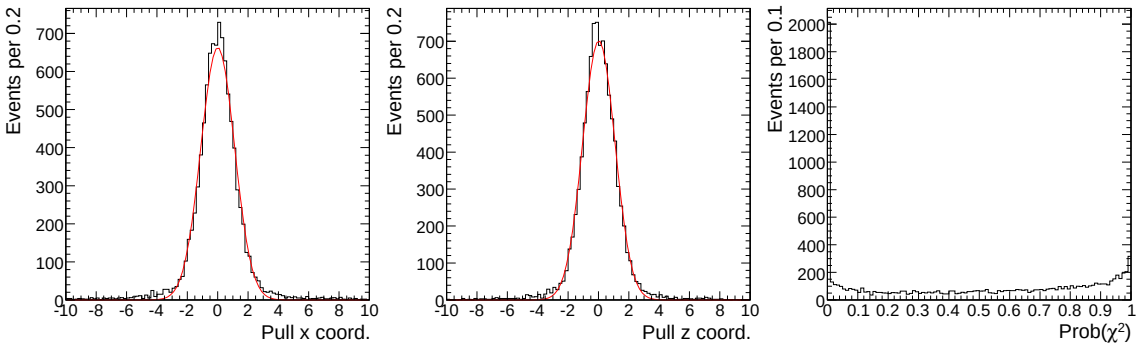

Figure 3.11: Distribution of coordinate pulls (**left:** x, **middle:** z) and χ^2 probability (**right**) of the $B_s^0 \to (J/\psi)\phi$ primary vertex, reconstructed with the Kalman filter method.

function:

$$w(\chi^2) = \frac{1}{1 + e^{-\frac{\chi^2_{\text{cutoff}} - \chi^2}{2T}}}, \tag{3.5}$$

where χ^2_{cutoff} is the distance where the weight function drops to 0.5 and T is the temperature which controls the sharpness of the drop (see Fig. 3.12). The down-weighted tracks are then used for the vertex fit (for instance, using Kalman filter-based algorithm). After the fit, the weights are recomputed and the vertex is refit until convergence. In order to avoid falling into local minima, an annealing schedule is introduced: at each iteration step, the initially high temperature T is lowered by a factor $r \leq 1$ [55].

It can be seen that contrary to the Kalman Vertex Fitter, the result of the AVF fit is not sensitive to the outliers. Another advantage of the AVF is that the track weights can be fractional (soft assignment) and they vary in the course of the fit. No

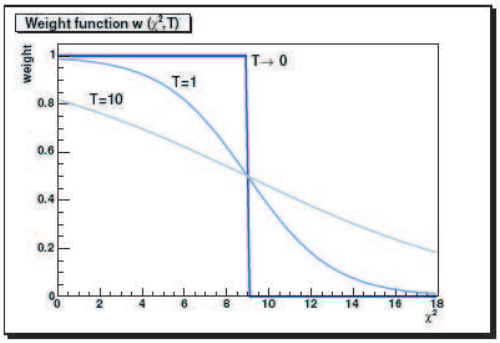

Figure 3.12: Weight functions of the Adaptive Vertex Fitter.

prior estimate of the contribution of tracks or on the fraction of outliers is required.

By default, the AVF is used with the Kalman filter, however, it is not tied to that particular algorithm. For instance, it has been shown that good result can also be obtained with the Gaussian-Sum Filter [54].

Another approach to vertex reconstruction is provided with the Principle Vertex Fitter which uses a Kalman filter to make a hard assignment of tracks to a vertex. The tracks which are incompatible with vertex, according to the χ^2 value, are removed and the vertex is refit. The procedure is repeated until the compatibility of all remaining tracks is above a given threshold. Contrary to the Adaptive Fitter, the tracks are not down-weighted (they all have the the weight of 1), and once rejected, a track can not be included in the vertex again [54].

Finally, the Gaussian-Sum Filter for vertex reconstruction (GSF) was developed and implemented in ORCA [54]. This method allows to perform the vertex fitting taking into account the non-Gaussian distribution of measurement errors. Here, the distributions of the errors of both measurements and state vector have to be modeled by mixtures of multi-variate Gaussian probability density functions [56]. The core of the distribution is described by the main component of the mixture and the tails are modeled with one or several additional Gaussians.

The fit procedure of the GSF is a weighted sum of several Kalman filters and it is implemented as a series of Kalman filters run in parallel. During the fit, when the track is added to the vertex, each component of the vertex state is updated with each component of the track state. The number of components of the estimated vertex rises therefore exponentially and should be limited to an acceptable number. This is achieve by clustering components, which are close, pair-wise, until the desired number of components is reached [56].

A complete description of vertex reconstruction methods implemented in the ORCA reconstruction program can be found in [55]. The results of comparison of all available algorithms in terms of their resolutions, CPU timing, χ^2 probabilities and vertex finding efficiencies is presented in [54].

3.4 Decay chain reconstruction and kinematic fitting

Kinematic fitting is the application of the conservation or geometric laws governing particle production or decay to improve the experimental resolution of the measurements [57]. In particular, the application of kinematic constraints (usually energy and momentum conservation) to the reconstructed data allows one to test decay hypothesis and find unknown parameters.

The Kinematic fitting is especially important in b-physics studies, where the highest possible resolution on the position of the secondary vertex as well as precise determination of the mass and momentum of both decayed b-flavoured meson and reconstructed final state are crucial.

In the current section, the development and implementation in the CMS reconstruction framework of the Kinematic fit and decay chain reconstruction library are presented.

The $B_s^0 \to (J/\psi)\phi \to \mu^+\mu^- K^+ K^-$ decay, which is the subject of the current study is used as an example. In this channel, the set of kinematic constraints to apply during the reconstruction of the parameters of the decayed B_s^0 meson can be the following:

- All four final state tracks ($\mu^+\mu^- K^+ K^-$) should come from the B_s^0 decay vertex, since the intermediate J/ψ and ϕ mesons have insignificant lifetimes of the order of 10^{-21} s and 10^{-22} s respectively.

- Due to the small natural width of the J/ψ meson (91 KeV), the invariant mass of two final state muons can be constrained to be equal to the mass of the J/ψ meson (3.096 GeV).

- The momentum of the B_s^0-meson, reconstructed at the decay position should point in the direction opposite to the primary interaction vertex, where the B_s^0 was produced.

The vertex constraint can be applied using one of the vertex reconstruction algorithms described in Sec. 3.3. Constraints on the invariant mass of the two muons and on the reconstructed momentum of the B_s^0 meson can be applied using one of the kinematic fitting methods discussed below.

As the reconstruction proceeds from the observed final state ($\mu^+\mu^-K^+K^-$) to the initial decaying state (the B_s^0 meson) by applying a set of constraints on the different components of the decay chain, only the calculated parameters of the initial decayed state will reflect all constraints applied through the reconstruction procedure. It is then desirable to propagate this knowledge down the decay chain to the final state particles and refit these with the full set of constraints. In full analogy with the smoothing step of the Kalman filter (see Sec. 3.3.1), this operation is supposed to improve the experimental resolution on the reconstructed parameters of the final state.

The value of the reduced χ^2 and number of the series of the constrained fits tests of the applicability of a decay hypothesis. Thus, the reconstruction of the decay chain through a series of kinematic fits becomes a powerful tool for background rejection.

In order to benefit from the above-mentioned advantages of this reconstruction method, I developed a kinematic fit and decay chain reconstruction library (KF) and implemented it in the CMS reconstruction framework. This library has the following features:

- The KF package allows the reconstruction of decay trees from the final state to the mother state according to the decay hypothesis provided by the user.
- The KF is designed to be applied to one hypothesis of final state tracks. In case different competing hypotheses exist (combinatorial problem), a collection of decay trees, each representing one hypothesis can be created.
- The application of arbitrary (user-defined) constraints is made possible during all stages of reconstruction
- The possibility of using as input reconstructed objects other than tracks reconstructed in the central tracker (such as reconstructed muons or jets) is also foreseen.

The details of implementation and mathematical algorithms used are described in the next sections. The description of the software structure can be found in [58] and [59].

3.4.1 Introduction to constrained fitting

The mathematical approach based on Least Mean Squares minimization (LMS) is presently the most widely used technique for constrained fitting. Sequential methods such as the Kalman filter and global methods (global minimization with Lagrange multipliers, global minimization with penalty functions, etc.) are the most common methods in high energy physics experiments.

Sequential algorithms are in general more flexible, allowing step by step update of estimated quantities, and are significantly faster than global ones, reducing CPU time by factorizing the inversion of covariance matrices [48]. However, only a limited number of problems can be solved using this approach, as it requires the initial data to be uncorrelated (joint measurement covariance matrix being block-diagonal), and the analytical solution is different for each different constraint.

The mathematical technique most widely used in kinematic fitting is the LMS with Lagrange multipliers. This method allows to constrain certain parameters to precise values ("hard" constraint: particle has a given mass, given momentum vector, etc...). Soft, or inequality constraints (particle mass lies in a certain region, is distributed according to the given p.d.f. etc...), can be imposed using other methods, such as LMS with penalty functions [14].

Least Mean Squares minimization with Lagrange multipliers

Consider a set of n experimental measurements $y = y_1, y_2, \ldots, y_n$ with their associated covariance matrix V_y, where diagonal terms $(V_1, \ldots, V_n)$ correspond to the covariance matrices of individual measurements. Suppose these measurements are subject subject to the set of k constraint equations $H_i(y) = 0$ $(i = 1, \ldots, k)$, denoted hereafter in the following vector form: $\vec{H}(y) = 0$. These equations are in general nonlinear. In the LMS method, in order to obtain a set of improved measurements y^{ref}, the following function should be minimized [9]:

$$\chi^2 = (y^{\text{ref}} - y)^T V_y^{-1} (y^{\text{ref}} - y), \tag{3.6}$$

with the constraint equations:

$$\vec{H}(y^{\text{ref}}) = 0. \tag{3.7}$$

[9] The vector notation $y = \begin{pmatrix} y_1 \\ \ldots \\ y_n \end{pmatrix}$ and $y^{\text{ref}} = \begin{pmatrix} y_1^{\text{ref}} \\ \ldots \\ y_n^{\text{ref}} \end{pmatrix}$ is assumed hereafter.

The constraint equations are then linearized (first-order Taylor expansion) around some starting point y_{exp}. The following linear form is then obtained:

$$\left.\frac{\partial \vec{H}}{\partial y}\right|_{y_{\text{exp}}} (y^{\text{ref}} - y_{\text{exp}}) + \vec{H}(y_{\text{exp}}) = D\delta y + d = 0, \tag{3.8}$$

where D is the matrix of derivatives of constraint equations with respect to parameters of the measurements and d is the vector of values of constraint equations at y_{exp}:

$$D = \begin{pmatrix} \left.\frac{\partial H_1}{\partial y_1}\right|_{y_{\text{exp}}} & \cdots & \left.\frac{\partial H_1}{\partial y_n}\right|_{y_{\text{exp}}} \\ \vdots & \ddots & \vdots \\ \left.\frac{\partial H_k}{\partial y_1}\right|_{y_{\text{exp}}} & \cdots & \left.\frac{\partial H_k}{\partial y_n}\right|_{y_{\text{exp}}} \end{pmatrix}, \quad d = \begin{pmatrix} H_1(y_{\text{exp}}) \\ \vdots \\ H_k(y_{\text{exp}}) \end{pmatrix} \quad \text{and} \quad \delta y = y^{\text{ref}} - y_{\text{exp}}.$$

Multiplying the linearized constraint equation (3.8) by an (unknown) Lagrange multiplier λ [14], and adding it to Eq. (3.6), the following χ^2 is to be minimized [57]:

$$\chi^2 = (y^{\text{ref}} - y)^T V_y^{-1} (y^{\text{ref}} - y) + 2\lambda^T (D\delta y + d) \to \min. \tag{3.9}$$

By minimizing this function with respect to y^{ref} and λ, the improved measurements and their joint covariance matrix are obtained. The problem has a unique solution $(y^{\text{ref}}, \lambda)$ [57]:

$$\begin{aligned} y^{\text{ref}} &= y - V_y D^T \lambda \\ \lambda &= (D V_y D^T)^{-1} (D\delta y_{\text{exp}} + d) \end{aligned} \tag{3.10}$$

where $\delta y_{\text{exp}} = y - y_{\text{exp}}$. The covariance matrix of refitted parameters can be obtained through the error propagation:

$$V_y^{\text{ref}} = V_y - V_y D^T (D V_y D^T)^{-1} D V_y. \tag{3.11}$$

Iterations are performed, taking each time the result of the previous step as the linearization point, performed or the residuals of the constraint equations are below the certain value.

When the functions H_i are linear in y, an exact solution (3.7) is obtained after the first iteration. If the constraint equations are highly nonlinear, the choice of the starting point is crucial. Therefore, for the fit to converge, the starting point should be chosen in the vicinity of the probable solution and the constraint equations should be well approximated with their linear version in this region.

It may be worth to note that some constraints may be nonlinear in one parametrization and become linear in another. It is also an interesting fact that the initial parametrization of the input data does not play any role in the formalism described above, The input data and the constraint equations must be defined in the same reference frame, but the user can choose the frame which is the most convenient for the problem at hand (e.g. the frame in which the constraint equations are linear).

3.4.2 Details of the implementation of the kinematic fit library

In the kinematic fit and decay chain reconstruction library, two different techniques of constrained fitting are used:

- The Kalman Vertex Fitter is used for vertex fitting without further constraints.
- The method of LMS minimization with Lagrange multipliers is used to refit the reconstructed parameters of the particles without vertex reconstruction and to reconstruct vertices with simultaneous application of constraints.

This choice of fitting algorithms seems to be natural for the set of constraints to apply during the reconstruction of the $B_s^0 \to (J/\psi)\phi \to \mu^+\mu^- K^+ K^-$ decay chain (see Sec. 3.4). However, due to the high modularity of both decay chain reconstruction and kinematic fitting parts of the library, other algorithms can be included without much difficulty.

The implementation of the kinematic fit and decay chain reconstruction library consists of two independent parts, related to the reconstruction of decay chain and constraint fits respectively. The description of the reconstruction of decay chain can be found in sec. 3.4.3. The strategies of constraint fitting and their implementation are discussed in Sec. 3.4.4, 3.4.5 and 3.4.6.

3.4.3 Reconstruction of decay chain

During the kinematic fit, a decay is reconstructed from "bottom" to "top" i.e. from the final state (for example, charged tracks reconstructed in the tracker) to the mother state (the B_s^0 meson in our example). Since the CMS detector has no particle identification system to distinguish between kaon and pion trajectories (muons can however be identified using muon chambers), a mass hypothesis should be assigned for each particle before the kinematic analysis. When different competing hypotheses are present(e.g. combinatorial problem), the χ^2 of the fit can be used as a selection criteria.

The description of the decay chain is based on the following conceptual components[10]: *KinematicParticle*, *KinematicVertex* and *KinematicTree*. The first two store the information about particles and vertices, and the latter one stores the hierarchy of every particle and vertex in the decay and provides a navigation mechanism between these. Each of the components mentioned above is implemented in a separate C++ class.

KinematicTree

The *KinematicTree* class describes a decay chain hypothesis. The class contains pointers to all particles and vertices forming the decay chain and allows the user to navigate between them. Several trees can be merged by constraining their top particles to the same vertex. A new tree object, containing all available information will then be created.

In Fig. 3.13 a possible structure of the reconstructed decay tree for the $B_s^0 \to (J/\psi)\phi \to \mu^+\mu^- K^+ K^-$ decay is shown. The tree is reconstructed from final state tracks to the mother particle. Every tree component caches pointers to its previous states and constraints applied, as well as the pointer to the current tree the component belongs to.

The internal structure of the tree is based on a graph library. The graph is a private data member of the *KinematicTree* class. It has reference-counted *KinematicParticles* as edges and reference-counted *KinematicVertices* as nodes. The navigation in the tree is handled by an internal graph library pointer, which is a private data member of the *KinematicTree* class. The actual graph structure of the class is hidden from the user, and a set of public methods allows the user to navigate in the tree and access the relevant information.

KinematicParticle

This class represents a particle in the decay chain. The *KinematicParticle* stores the parameters describing the particle (reconstructed trajectory parameters and assigned or reconstructed mass), the corresponding covariance matrix, the charge, the χ^2 and the number of degrees of freedom assigned to the current particle during previous stages of the reconstruction. Every object of the class also stores the last constraint applied and the state of the particle before that constraint had been applied.

[10]Each of these components is implemented in the separate C++ class with the corresponding name. See [58] for software implementation details.

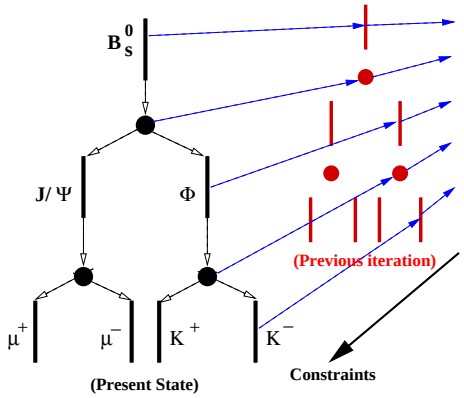

Figure 3.13: A possible reconstructed tree of $B_s^0 \to (J/\psi)\phi \to \mu^+\mu^- K^+ K^-$ decay. Every tree component "remembers" its state before the last refit.

A *KinematicParticle* can be created by assigning a mass hypothesis to a reconstructed trajectory using the provided *KinematicParticleFactory*. It is also created by the kinematic particle vertex fitters when fitting several trajectories to the same vertex and calculating the decayed state.

Parametrization of the particle

The state of the particle is described by 7 parameters (quasi-cartesian parametrization): a reference position in the global frame (x, y, z) , the momentum at this point (p_x, p_y, p_z) and the mass of the particle m (calculated as a result of previous fits or assigned by the user). This parametrization is exclusively used when deriving constraint equations. The vector of 7 parameters and their joint (7×7) covariance matrix are cached in the *KinematicState* class.

In case the particle is created by assigning a mass hypothesis to the reconstructed track, a negligible error should be assigned to the mass hypothesis in order to fill the corresponding diagonal element of the covariance matrix and avoid singularities.

Since the Kalman vertex fit is used as a part of the library, an "extended" perigee parametrization is also provided. The first five parameters are identical to the usual perigee parameters described in the Sec. 3.3.1, and the sixth parameter is the mass of the particle. This parametrization can not be used for the derivation of constraint equations, however it may be used in a subsequent analysis.

KinematicVertex

This class stores the vertex information needed for the kinematic fit: position, covariance matrix, χ^2 and number of degrees of freedom. As the *KinematicParticle*,

the *KinematicVertex* contains references to its previous states (vertex parameters before application of additional constraints). A *KinematicVertex* is always produced as a result of a vertex fit of a set of *KinematicParticles*.

3.4.4 Factorization of constraints and reconstruction strategies

Two different strategies can be used when reconstructing a decay chain using the Kinematic fit. The most intuitive way is to refit the input data with all the constraints and to find all unknown parameters in a single fit (*Global strategy*). For example, the parameters of the decayed B_s^0 meson can be calculated after a single fit where the two muon and two kaon tracks are constrained to come from a single vertex, and requiring the invariant mass of the two muons to be equal to the mass of the J/ψ and the sum of the momenta to point towards the primary vertex.

However, a different strategy can be used. The two final state muons can first be fit to a vertex, reconstructing thus the J/ψ parameters at this vertex, then constraining the mass of this intermediary state to be equal to the mass of the J/ψ. After that, the J/ψ and the 2 kaons would be fit to a vertex, reconstructing the B_s^0 parameters at this vertex, and the pointing constraint would finally be applied on the B_s^0. Here, the application of the set of constraints in a single fit is substituted with a series of individual fits, applying the constraints one by one on individual, reconstructed particles (*Sequential strategy*).

This approach is possible due to a remarkable property of the LMS-based algorithms: the result of the simultaneous application of the set of constraints is mathematically equivalent to their sequential application. The result of a global fit with a set of constraints is therefore equal to the result of a series of sequential fits, where each constraint is applied individually. The corresponding theorem can be found in [57] (general formulation and application to constraint fitting) and [60] (proof).

The usage of the sequential fits becomes especially important when working with unstable particles with significant lifetimes, were reconstructed states are to be propagated inside the detector. This method has nevertheless one drawback. As the fit proceeds from the final state to the initial state by applying different constraints on the different decays of the chain in succession, only the initial state (e.g the B_s^0 in our example) will reflect all constraints applied throughout the fit. Propagating this knowledge down the decay chain to the final states and refitting these with the full set of constraints is not straightforward, the mathematical aspects of this procedure are however discussed below.

In order to test the advantages of both the global and the sequential strategies, different mathematical algorithms were implemented. For the Global fit, a vertex fit with simultaneous application of additional constraints was implemented. For the Sequential fit, where the constraints are applied to an already reconstructed particle, a particle refit (for single or multiple particles) without vertex reconstruction was developed. The application of both strategies to the reconstruction of the B_s^0 decay is discussed below.

3.4.5 Sequential strategy

As can be seen from the example given above, the implementation of sequential strategy requires the following tools: a vertex fitter without simultaneous application of additional constraints, an algorithm calculating the parameters of decayed particle and a mechanism to refit the parameters of the particle without vertexing. The mechanism, propagating the applied constraints down the reconstructed decay chain is also desirable.

In the current implementation of the sequential strategy, the vertex fit is performed using the Kalman Filter (c.f. Sec 3.3.1). The algorithms, suitable for calculation of the the parameters of a decayed particle, refit of the parameters of the particle without vertexing and down propagation of constraints are discussed in the current section.

Calculation of decayed particle parameters

The kinematic fit and decay chain reconstruction library allows the user to calculate the parameters of the decayed particle and their covariance matrix from the parameters and covariance matrices of decay products. This calculation is performed via the following steps: reconstruction of the decay vertex from the decay products, refit of the parameters of the decay products with the vertex constraint, calculation of the full refitted covariance matrix of all the refitted parameters, calculation of the parameters of the decayed particle and its covariance matrix. The calculation of the momentum of the decayed particle is done by summing the momenta of the refitted decay products at the vertex position. The covariance matrix of the new particle is calculated from the full particle-to-particle covariance matrix taking all correlations into account. A set of Jacobians was developed to calculate each block of the covariance matrix (position, momentum and position-momentum correlation) and the mathematical technique is in general identical to the one used in [61].

Refit of particle parameters without vertexing

If no vertex reconstruction is required, the refit of a set of N^{track} particles is straightforward in the LMS with Lagrange multipliers formalism discussed above. As the $(x, y, z, p_x, p_y, p_z, m)$ quasi-cartesian parametrization is used, the input vector of parameters will have dimension $7 \cdot N^{track}$. The covariance matrices of each track (of dimension (7×7)) can come from previous fits or be created, using the covariance matrix of the reconstructed track and assigning a negligible error to the mass hypothesis, as discussed in 3.4.2.

The particles to refit are supposed to be uncorrelated, and their joint $(7 \cdot N^{track} \times 7 \cdot N^{track})$ covariance matrix is supposed to be block diagonal. In principle, the mathematical approach presented above does not distinguish between correlated and uncorrelated measurements and the framework can easily be extended to work with correlated particles if needed.

Once refitted, all parameters of all tracks will be correlated, i.e. their joint covariance matrix will not be block-diagonal anymore. As it was briefly mentioned in the previous section, the global LMS minimization algorithm behaves differently when applying constraints of linear and nonlinear type.

Linear constraints

An implementation of the linear constraints is straightforward in the formalism discussed above. For instance, constraining the mass of the single particle to the value M^{fix} in the 7-parametrization discussed above, results in the following linear equation:

$$H_1(y) = m - M^{\text{fix}} = 0. \tag{3.12}$$

The matrix of derivatives D and the vector of values d taken at some expansion point y^{exp} are:

$$D = \frac{\partial H(y^{exp})}{\partial y} = \begin{pmatrix} 0 & 0 & 0 & 0 & 0 & 0 & 1 \end{pmatrix} \tag{3.13}$$

and

$$d = H_1(y^{exp}) = m - M^{\text{fix}}. \tag{3.14}$$

Here the matrix D and the vector d consist respectively of a single row and a single element. In case several constraint equation should be satisfied in a single fit (for instance, constraining the direction of the momentum of a particle would require a set of two constraint equations), the number of rows in the corresponding matrix of derivatives and the vector of values will be equal to the number of constraint equations.

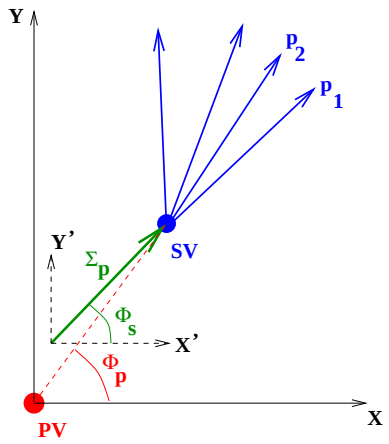

Figure 3.14: The B_s^0 momentum and decay vertex reconstructed from decay products (transverse plane). The momentum vector is not aligned with primary-secondary vertex direction.

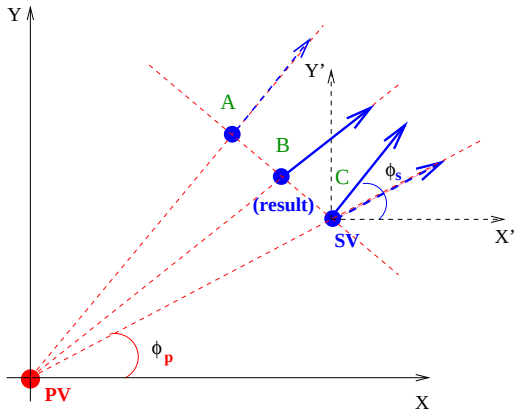

Figure 3.15: Possible solutions for the alignment problem. **A:** vertex shift along direction perpendicular to the primary-secondary vertex vector. **C:** rotation of the momentum vector. **B:** solution taken by LMS minimization, partly incorporating both possibilities.

Nonlinear constraints

As it was mentioned before, care should be taken when nonlinear constraints are to be implemented in the framework. This will be illustrated with the example of the "pointing" constraint. In this constraint, the vector pointing from the primary to the secondary vertex and the reconstructed momentum vector of the B_s^0 are required to be parallel. This goal may be achieved in two different ways: either the secondary vertex is shifted, aligning the momentum vector with the direction to the primary vertex, or the momentum vector itself is rotated. If the constraint equations allow for both possibilities, the LMS based algorithm finds an optimum between the two, using partly each of them. The sketches in Fig. 3.14 and 3.15 illustrate this idea.

Naming the angles under which the secondary vertex is seen from the primary vertex (ϕ_p, θ_p) and the angles of the B_s^0 momentum at the secondary vertex (ϕ_s, θ_s) (all angles are defined in the global frame), the following equation is proposed to fulfill our requirements [11] :

$$\tan\frac{\phi_p}{2} - \tan\frac{\phi_s}{2} = \frac{1-\cos\phi_p}{\sin\phi_p} - \frac{1-\cos\phi_s}{\sin\phi_s} = \frac{\sin\frac{\phi_p-\phi_s}{2}}{\cos\frac{\phi_p}{2}\cos\frac{\phi_s}{2}} = 0 \qquad (3.15)$$

[11] This equation was chosen mostly because of the simplicity of calculation of the derivatives in the quasi-cartesian frame. Taking partial derivatives of the identical constraint equation $\phi_p - \phi_s = 0$ in this frame would require a much more complex mathematical apparatus.

This equation has roots at $\phi_p - \phi_s = 0 + 2\pi \cdot k$ and singular points in ϕ_p or $\phi_s = \pi + 2\pi \cdot k$, where k is a positive integer. This equation works well in the area of definition of the azimuthal angle, except for the singular points. When both ϕ_p and ϕ_s are close to π, the value of the equation is close to 0. The situations when one of the angles is equal to π and the other one is far away should be excluded. These events are very rare and represent no physical interest, and since the total χ^2 of such a fit would be very large and these events would be rejected by the χ^2 probability cut. Similar equation can be derived for the polar angle. In the quasy-cartesian frame (see Sec. 3.4.2) it is easy to rewrite those equations in terms of the momentum of the B_s^0 meson and coordinates of the vertices:

$$\begin{aligned} H_\phi &= \frac{1 - \frac{dx}{\sqrt{dx^2+dy^2}}}{\frac{dy}{\sqrt{dx^2+dy^2}}} - \frac{1 - \frac{p_x}{\sqrt{p_x^2+p_y^2}}}{\frac{p_y}{\sqrt{p_x^2+p_y^2}}} = 0 \\ H_\theta &= \frac{1 - \frac{\sqrt{dx^2+dy^2}}{\sqrt{dx^2+dy^2+dz^2}}}{\frac{dz}{\sqrt{dx^2+dy^2+dz^2}}} - \frac{1 - \frac{\sqrt{p_x^2+p_y^2}}{\sqrt{p_x^2+p_y^2+p_z^2}}}{\frac{p_z}{\sqrt{p_x^2+p_y^2+p_z^2}}} = 0, \end{aligned} \tag{3.16}$$

where (d_x, d_y, d_z) is the vector pointing from the primary to the secondary vertex ($dx = x_s - x_p$, $dy = y_s - y_p$, $dz = z_s - z_p$) and $(x_s, y_s, z_s, p_x, p_y, p_z, m)$ are the parameters of the particle at the secondary vertex. The derivation of the matrix of derivatives becomes then straightforward:

$$\frac{\partial H_\phi}{\partial x_s} = \frac{dx}{dy\sqrt{dx^2+dy^2}} - \frac{1}{dy} \qquad \frac{\partial H_\phi}{\partial y_s} = \frac{1}{\sqrt{dx^2+dy^2}} - \frac{\sqrt{dx^2+dy^2}}{dy^2} + \frac{dx}{dy^2}$$

$$\frac{\partial H_\phi}{\partial z_s} = 0 \qquad \frac{\partial H_\phi}{\partial p_x} = -\left(\frac{p_x}{p_y\sqrt{p_x^2+p_y^2}} - \frac{1}{p_y}\right)$$

$$\frac{\partial H_\phi}{\partial p_y} = -\left(\frac{1}{\sqrt{p_x^2+p_y^2}} - \frac{\sqrt{p_x^2+p_y^2}}{p_y^2} + \frac{p_x}{p_y^2}\right) \qquad \frac{\partial H_\phi}{\partial p_z} = 0$$

$$\frac{\partial H_\phi}{\partial m} = 0 \qquad \frac{\partial H_\theta}{\partial x_s} = \frac{dx}{dz}\left(\frac{1}{\sqrt{dx^2+dy^2+dz^2}} - \frac{1}{\sqrt{dx^2+dy^2}}\right)$$

$$\frac{\partial H_\theta}{\partial y_s} = \frac{dy}{dz}\left(\frac{1}{\sqrt{dx^2+dy^2+dz^2}} - \frac{1}{\sqrt{dx^2+dy^2}}\right) \qquad \frac{\partial H_\theta}{\partial z_s} = \frac{\sqrt{dx^2+dy^2}-\sqrt{dx^2+dy^2+dz^2}}{dz^2} + \frac{1}{\sqrt{dx^2+dy^2+dz^2}}$$

$$\frac{\partial H_\theta}{\partial p_x} = -\frac{p_x}{p_z}\left(\frac{1}{\sqrt{p_x^2+p_y^2+p_z^2}} - \frac{1}{\sqrt{p_x^2+p_y^2}}\right) \qquad \frac{\partial H_\theta}{\partial p_y} = -\frac{p_y}{p_z}\left(\frac{1}{\sqrt{p_x^2+p_y^2+p_z^2}} - \frac{1}{\sqrt{p_x^2+p_y^2}}\right)$$

$$\frac{\partial H_\theta}{\partial p_z} = -\left(\frac{\sqrt{p_x^2+p_y^2}-\sqrt{p_x^2+p_y^2+p_z^2}}{p_z^2} + \frac{1}{\sqrt{p_x^2+p_y^2+p_z^2}}\right) \qquad \frac{\partial H_\theta}{\partial m} = 0$$

It seems to be obvious that the quasi-Cartesian parametrization is not the best choice for the derivation of an angular-dependent constraints. It would be more natural in this case to select a parametrization where the constraint equations become linear with respect to the angles (extended perigee, for instance). A further

improvement of the discussed library would therefore be the development of a frame-independent version, using the advantage of the algorithm being parametrization-independent (see Sec. 3.4.1).

Down propagation of constraints

As discussed before, in case of sequential reconstruction, only the initial state (the top particle of the reconstructed tree) reflects all the constraints applied through the fit. The mechanism to propagate this knowledge "down" the reconstructed tree is not yet implemented in the current version of the kinematic fit and decay chain reconstruction library.

For instance, let us consider a reconstructed $B_s^0 \to (J/\psi)\phi \to \mu^+\mu^- K^+ K^-$ decay tree, similar to this, presented in the Fig. 3.13. Here the parameters of the B_s^0 meson were calculated at the reconstructed vertex of J/ψ and ϕ mesons [12]. After the pointing constraint, new parameters are obtained for the B_s^0 meson. The momentum of B_s^0 meson is no longer equal to the sum of momenta of J/ψ and ϕ and the position of the secondary vertex in which the momentum of the B_s^0 is defined differ from the position of the fitted vertex of J/ψ and ϕ (see Sec. 3.4.5). This situation is somewhat analogous to the one appearing in Kalman filter without smoothing: only the last estimate (here the parameters of the B_s^0 meson) includes all the constraints applied through in fits. The estimates obtained in the next-to-last step of the reconstruction include everything but the last constraint (the parameters of the J/ψ and ϕ meson were smoothed with their common vertex, but not with the information obtained after the pointing constraint) and so on.

A solution for this problem can be analogous to smoothing step of the Kalman filter. The "down" propagation of the information can be performed through a series of constrained fits, were at every step the parameters of the daughter particles are constrained in the following way:

- The sum of the momenta of the daughter particles is fixed to be equal to the momentum of the mother particle.

- The trajectories of daughter particles are forced to pass through the secondary vertex in which the mother particle is defined.

[12] Both J/ψ and ϕ mesons have insignificant lifetimes (see Sec. 3.4), therefore it is not necessary to reconstruct their parameters in order to reconstruct the B_s^0meson. However, this reconstruction makes a good example of properties of kinematic fitting

Using this strategy, the parameters of the final state particles can be updated with the information obtained at the later stages of the reconstruction.

As it was mentioned above, once the particles are fitted to a vertex, their parameters become correlated both with the vertex position and with parameters of other particles, and the joint covariance matrix have a size of $(3 + 7 \cdot N^{particles} \times 3 + 7 \cdot N^{particles})$. If the "down" propagation of constraints is planned, this full covariance matrix should be stored with every vertex and used when updating the daughter states with the information from the mother state.

Finally, the problem of "down" propagation of constraints can be fully avoided in the Global strategy (see next section). Here, all the parameters can be refitted in a single step, applying all constraints simultaneously. However, in this case, the constraints to apply on the parameters of the mother state should be expressed in terms of the parameters of the final state particles. For instance, in case of $B_s^0 \to (J/\psi)\phi \to \mu^+\mu^- K^+ K^-$ decay, the pointing constraint for the B_s^0 meson should be expressed in terms of momenta of final state muons and kaons.

Mathematically, both approaches (Sequential strategy with "down" propagation of constraints and Global strategy) should lead to the same result within the precision of computation. An advantage of the Sequential approach is the fact that it can be also used to reconstruct decays, where the intermediate particles have significant lifetimes and should be propagated through the detector (for instance, decays containing a D^0 meson as intermediate state). In this case, the use of the Global strategy seems to be difficult.

3.4.6 Global strategy

As mentioned above, the global strategy deals with application of the constraints during the vertex fit. This approach is possible with LMS with Lagrange multipliers. In the current section the development of vertex constraints and application of additional constraints during the vertex fit are discussed.

Vertex constraint

In case of vertex fitting using the LMS with Lagrange multipliers, the number of fit parameters should be increased to $3+7 \cdot N^{\text{tracks}}$ with respect to the fit without vertexing. The first 3 parameters stand for the unknown coordinates of the vertex position (x_v, y_v, z_v). A set of special constraint equations should also be implemented. The total number of parameters becomes then $3 + 7 \cdot N^{track}$ and the joint covariance matrix of all the measurements has a dimension of $(3 + 7 \cdot N^{track}) \times (3 + 7 \cdot N^{track})$.

As the coordinates of the vertex are not known apriori, a reasonable guess has to be taken. As usual, the point of closest approach can be taken. As the elements of the covariance matrix pertaining to the vertex coordinates are also unknown, it is natural to use very large values, as suggested in [14] and [48] and successfully implemented in [50]. As a nearly infinite error, or negligible weight, is assigned to the apriori knowledge, this technique is called the "Huge error method" [57].

The vertex constraint equations (2 per particle) force the trajectories of the particles to pass trough an unknown point. In the perigee parametrization, this amounts to setting both both transverse and longitudinal impact parameters with respect to the unknown reference point to zero. The equations of motion of charged particle in the magnetic field should be used. A brief description of this procedure can be found in [57]. As the resulting constraint equations are highly nonlinear, the iterative procedure described in Sec. 3.4.1 should be applied.

In general, the result of vertex fitting using LMS minimization with Lagrange multipliers mechanism is mathematically identical to the Kalman filter [48]. Both algorithms were implemented in ORCA, showing the same result in terms of resolution of the reconstructed position of primary and secondary vertices. Despite the possibility of adding arbitrary constraints into the vertex fitting problem (Sec. 3.4.6), LMS minimization with Lagrange multipliers has also some serious disadvantages, as will be outlined below.

Additional constraints during vertex reconstruction

An application of additional constraints during the vertex reconstruction is possible using LMS with Lagrange multipliers by adding additional lines into the D matrix of derivatives. The vertex constraint introduces $2 \cdot N^{\text{track}}$ lines into the D matrix (two equations per track: longitudinal and transverse impact parameters), and N^{add} additional lines are added for the constraints. The size of vector of values changes accordingly.

As an example of this approach, a constraint requiring the first two tracks from the set to have a given invariant mass during the vertex fit was developed. The actual constraint equations were derived using the equations of motion of a charged particles in a magnetic field. Using an appropriate parametrization, this approach can also be extended to the neutral particles if needed.

Suppose we have two reconstructed particles with 7-parameters vectors

$$q_1 = (x_1, y_1, z_1, p_{1z}, p_{1y}, p_{1z}, m_1) \tag{3.17}$$

and

$$q_2 = (x_2, y_2, z_2, p_{2z}, p_{2y}, p_{2z}, m_2) \tag{3.18}$$

and charges e_1 and e_2, which we want to constraint to have a squared invariant mass M^2. Since these are charged particles in a magnetic field, all operations have to be performed at their common vertex (x^v, y^v, z^v).

The constraint equation is simply an energy conservation law:

$$H_1 = E^2 - \vec{P}^2 - M^2, \tag{3.19}$$

where E is the sum of the energies ($E = e_1 + e_2 = \sqrt{\vec{p_1}^2 + m_1^2} + \sqrt{\vec{p_2}^2 + m_2^2}$) and $\vec{P}$ is the sum of the momenta at the vertex ($\vec{P} = \vec{p_{1v}} + \vec{p_{2v}}$). For the calculation of the total momentum, the equations of motion in the solenoidal magnetic field are needed :

$$\begin{aligned} p_x^v &= p_x - a(y_v - y) \\ p_y^v &= p_y + a(x_v - x) \\ p_z^v &= p_z \end{aligned}$$

where $a = -0.29979Bq$ is the factor relating the transverse momentum of the charged particle to the transverse curvature of its trajectory, B is the z-component of the magnetic field in Tesla, and q is the charge of the particle. Taking the partial derivatives of equation 3.19 with respect to the vertex position and the parameters of the particles, the line to add to the D matrix is obtained:

$$\begin{array}{ll} \frac{\partial H_1}{\partial x^v} = -2(p_{1y}^v + p_{2y}^v)(a_1 + a_2) & \frac{\partial H_1}{\partial y^v} = 2(p_{1x}^v + p_{2x}^v)(a_1 + a_2) \\ \frac{\partial H_1}{\partial z^v} = 0 & \frac{\partial H_1}{\partial x_1} = 2a_1(p_{2y}^v + p_{1y}^v) \\ \frac{\partial H_1}{\partial y_1} = -2a_1(p_{1x}^v + p_{2x}^v) & \frac{\partial H_1}{\partial z_1} = 0 \\ \frac{\partial H_1}{\partial p_{1x}} = 2(1 + \frac{e_2}{e_1})p_{1x} - 2(p_{1x}^v + p_{2x}^v) & \frac{\partial H_1}{\partial p_{1y}} = 2(1 + \frac{e_2}{e_1})p_{1y} - 2(p_{1y}^v + p_{2y}^v) \\ \frac{\partial H_1}{\partial p_{1z}} = 2(1 + \frac{e_2}{e_1})p_{1z} - 2(p_{1z}^v + p_{2z}^v) & \frac{\partial H_1}{\partial m_1} = 2m_1(1 + \frac{e_2}{e_1}) \end{array}$$

and similarly for the second particle. This populates the first three elements of the line with the derivatives with respect to the vertex position, the next seven with derivatives with respect to the parameters of the first particle and the following seven with derivatives with respect to the parameters of the second particle. The vector of values d should be extended by 1 element.

Note about calculation of the covariance matrix

As it was mentioned in the Sec. 3.4.1, the calculation of the full covariance matrix in the formalism of LMS minimization with Lagrange multipliers is done using the standard method of error propagation:

$$V_y^{\text{new}} = V_y^{\text{old}} - V_y^{\text{old}} D^T (D V_y^{\text{old}} D^T)^{-1} D V_y^{\text{old}}, \tag{3.20}$$

where V^{old} is initial covariance matrix. The two matrices that are subtracted are of the same order of magnitude. When using the "huge error method", the first three diagonal elements, representing the vertex coordinates, are typically in the order of 10^6 cm^2 and the difference between the elements might be smaller than 10^{-10} cm^2. Due to the numerical precision, this can lead to significant errors in the calculations of the covariance matrix. Moreover, the precision of the algorithm becomes dependent on the value of the initial error. While the idea of the huge error method is to introduce an uncertainty on the first hypothesis of the unknown parameters as large as possible in order not to bias the fit, too large error terms might create numerical instabilities [13].

The Kalman filter used when only the vertex fit is performed does not suffer from this problem, as it is formulated as an information filter [48], where weight matrices are used instead of covariance matrices and the fit is performed iteratively. However, not every constrained minimization problem can be formulated in terms of the information filter, since it can not be derived generically for an arbitrary constraint.

Using the weight matrices instead of the covariance matrices, such that instead of subtracting errors, weights are added, is not straightforward. Indeed, combinations of V_y^{old} and of the D matrices, which are arbitrary due to the possibility of using different constraints, are not protected from being singular.

In order to avoid this problem, an adequate choice has to made for the initial covariance matrix according to the experimental conditions and the constraints imposed. For instance, in a pure vertex fit, initial diagonal elements of $\sigma^2_{\text{init}} = 10^4$ cm^2 do not seem to influence the fit in any way, and the error components returned are the same as for Kalman filter with $\sigma^2_{\text{init}} = 10^6$ cm^2.

[13] This problem is relevant for all the algorithms using the LMS minimization with Lagrange multipliers with the current mathematical approach.

3.5 Results for the $B_s^0 \to (J/\psi)\phi \to \mu^+\mu^- K^+K^-$ decay

In this section different strategies (see Sec. 3.4.4) for the reconstruction of the decay $B_s^0 \to (J/\psi)\phi \to \mu^+\mu^- K^+K^-$ using the kinematic fit are compared in terms of resolution on the reconstructed mass of the B_s^0 meson and coordinates of its decay vertex.

All the plots in this section are produced using the sample of 39000 signal events. The detailed description of this data sample can be found in Sec. 4.1. On the generator level, the p_t of the final state muon and kaon tracks are required to be above 2.0 GeV/c and 0.5 GeV/c respectively. No further selection cuts are applied.

For every event the simulated muons and kaons were extracted from the Monte Carlo information. The corresponding signal tracks were reconstructed in the tracker using the version **8.7.3** of ORCA (see Sec. 3.1). The parameters of the B_s^0 meson was then reconstructed using four following strategies

1. **Kalman filter:** The first strategy is the simplest: it includes only the reconstruction of the vertex using the Kalman filter and the parameters of the B_s^0 are calculated at the secondary vertex from the refitted final state tracks. No further constraint is applied. The results of this algorithm will be used as a baseline for comparison throughout the rest of this section.

2. **Global strategy:** The parameters of the decaying B_s^0 meson are calculated after fitting the two muon and two kaon tracks to the same vertex, requiring the invariant mass of the two muons to be equal to the mass of the J/ψ.

3. **Global strategy with pointing:** Same as 2), but with the pointing constraint (see Sec. 3.4.5).

4. **Sequential strategy with one neutral particle propagation:** Two final state muons are fitted to a vertex, reconstructing thus the J/ψ at this vertex. The mass of the J/ψ is then constrained to be equal to its world-average value. The J/ψ and the 2 kaons are then fitted to a common vertex, reconstructing thus B_s^0 meson at this vertex. The pointing constraint is finally applied to the B_s^0.

Wherever the pointing constraint is applied, the position of the primary vertex is taken from the Monte Carlo information.

Strategy, Reconstructed Component	50%	90%	95%
Kalman, B_s^0 mass (MeV)	24.00	72.97	97.26
Kalman, x-coordinate (μm)	33.9	118.8	172.1
Kalman, z-coordinate (μm)	51.0	289.7	487.6
Global, B_s^0 mass (MeV)	9.26	29.98	42.04
Global, x-coordinate (μm)	34.3	119.7	171.9
Global, z-coordinate (μm)	51.6	303.0	491.8
Global with pointing, B_s^0 mass (MeV)	9.61	33.70	56.75
Global with pointing, x-coordinate (μm)	26.0	125.8	274.5
Global with pointing, z-coordinate (μm)	47.8	372.7	782.7

Table 3.2: Coverages of different strategies of kinematic fitting.

The coverages (see Sec. 3.3.1) for the mass of the B_s^0 meson and x and z coordinates of the secondary vertex, reconstructed with different kinematic fit strategies are presented in the Table 3.2. The distributions of residuals and pulls are presented in the next sections. Unless significant non-Gaussian tails are present, the distributions are fitted with a single Gaussian function and a standard deviation of this function is quoted as resolution. In the case of significant tails, the sum of two Gaussians, one to describing the core and one describing the tails of the distribution is used. The standard deviation of the core Gaussian is then quoted as the resolution.

3.5.1 Kalman filter

In Fig. 3.16 (left) the distribution of the residuals of the invariant mass of the reconstructed B_s^0 meson is shown[14]. The mean of the Gaussian fit is approximately 15.5 MeV higher than the world-average mass of the B_s^0, and the standard deviation is about 34 MeV.

It is believed that this bias arises from inhomogeneities of the magnetic field not properly taken into account during the track reconstruction. In Fig. 3.16 (middle) distribution of the residuals of the invariant mass of J/ψ where this effect can also

[14]Hereafter the residuals of the invariant mass are calculated as the difference between the value of the reconstructed mass and its corresponding world-average value: 5.3696 GeV for the B_s^0, 3.097 GeV for J/ψ and 1.019 GeV for ϕ [41].

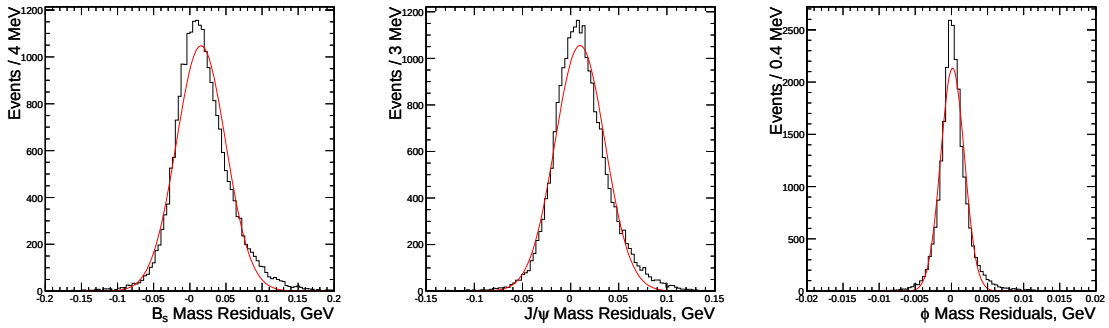

Figure 3.16: Distributions of the mass residuals for the Kalman filter method. **Left:** B_s^0-meson, **middle:** J/ψ-meson, **right:** ϕ-meson.

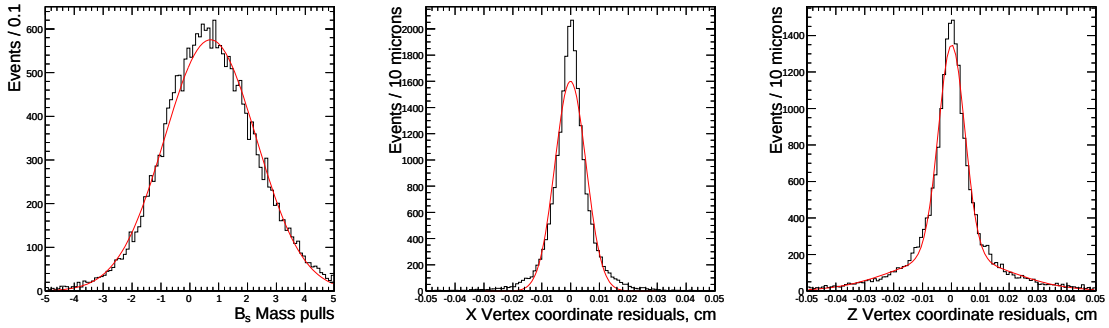

Figure 3.17: Distributions of the B_s^0 mass pulls (**left**) and vertex coordinate residuals (**middle:** x, **right:** z) for the Kalman filter method.

be seen is presented. The mean of the distribution of the J/ψ mass is some 10 MeV higher than the world-average, whereas the ϕ mass distribution is well centered (Fig. 3.16 (right)).

In Fig. 3.17 (left), the distribution of the pulls of the B_s^0 mass is presented. The distribution is well modeled by a Gaussian with a standard deviation of 1.6, the uncertainty on the mass of the reconstructed B_s^0 being underestimated [48]. This effect comes from the underestimation of uncertainties on the transverse curvature, when reconstructing muons with the Combinatorial Track Finder [58].

The distributions of the residuals and pulls of the longitudinal and transverse coordinates of the reconstructed decay vertex are presented in Fig. 3.17 and 3.18 respectively. The resolutions on the transverse coordinate is 54 μm. Contrary to the Sec. 3.3.1 the distribution of residuals for the longitudinal coordinate is fitted with a double Gaussian function. The standard deviation of the core Gaussian is approximately 45 μm. The errors of both coordinates are reasonably well estimated.

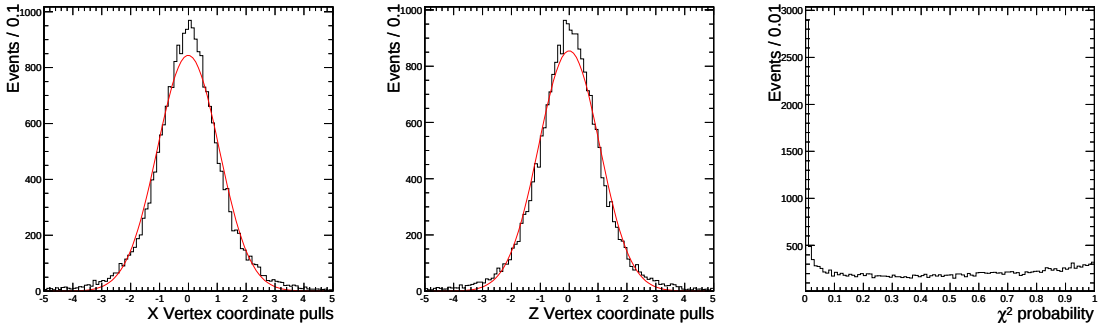

Figure 3.18: Distributions of the vertex coordinate pulls (**left:** x, **middle:** z) and χ^2 probability of the fit (**right**) for the Kalman filter method.

The distribution of the χ^2 probability of the Kalman fit is presented in Fig. 3.18 (right). For each event the number of degrees of freedom is equal to 4. The probability distribution is flat over the whole range with a peak at low values. This is due to the fact that the residuals of the track parameters are not exactly Gaussian-distributed and have significant tails. This problem is discussed in more details in [50], [56] and Sec. 3.3.

3.5.2 Global strategy

The distributions of the residuals and pulls of the invariant mass and χ^2 probability of the fit for the B_s^0 meson, reconstructed with a global strategy is presented in Fig. 3.19. The mass resolution is 14 MeV and the distribution is more centered (approximately 4 MeV shift) with comparison to the Kalman filter. The distribution of the mass pulls has the same shape and width as with the Kalman filter. The total χ^2 probability distribution (for 5 degrees of freedom in this case) has the same shape as in the Kalman case, as is expected, since both methods are LMS-based and both expect the measurements errors to be Gaussian-distributed. The resolution on the x and z vertex position are roughly the same as with the Kalman filter.

It can also be noted (see Tab. 3.2), that the global strategy with J/ψ invariant mass constraint improves the coverage on the mass of the B_s^0 meson with respect to the Kalman fit. The coverages on the x and z coordinates of the reconstructed vertex stay in the same range.

3.5.3 Global strategy with pointing

The pointing constraint changes both the direction of the momentum and the position of the secondary vertex, which influences the invariant mass through the

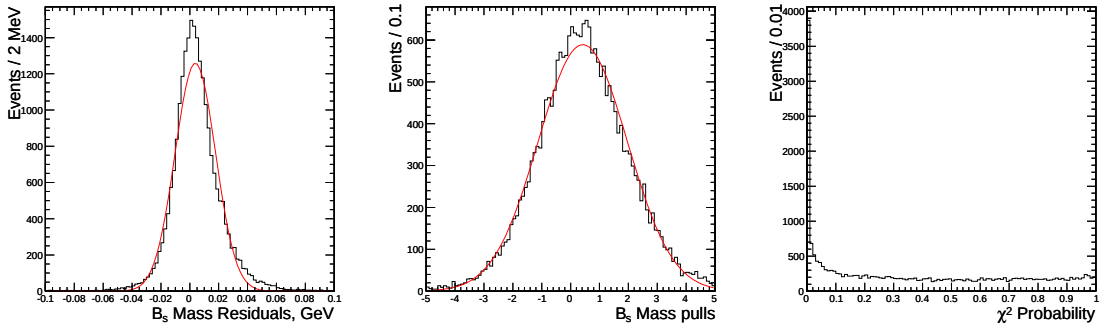

Figure 3.19: Distributions of the residuals (**left**) and pulls (**middle**) of the invariant mass and χ^2 probability (**right**) of the fit for the B_s^0 meson, reconstructed with a global strategy.

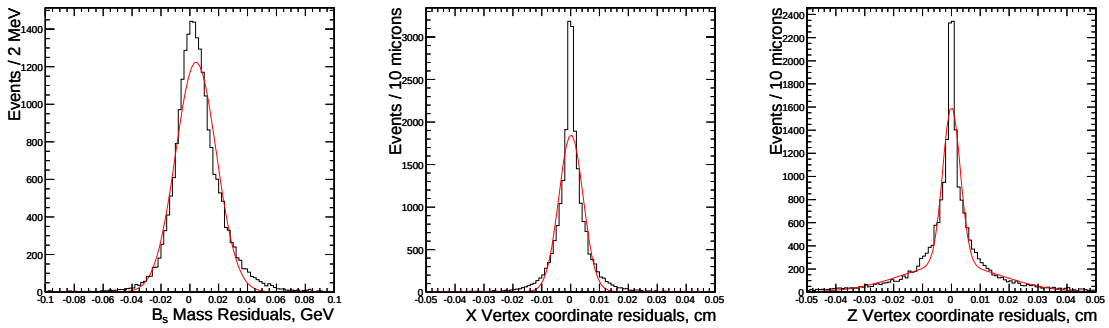

Figure 3.20: Distributions of the residuals of the invariant mass (**left**), x vertex coordinate (**middle**) and z vertex coordinate (**right**) of the B_s^0-meson, reconstructed with a global strategy with pointing constraint.

corresponding terms of the covariance matrix (see Sec. 3.4.5). This means that in the case of badly reconstructed events (where the B_s^0-meson momentum is very far from being aligned with the primary vertex), the mass can be significantly changed by the pointing constraint. Such events are very rare and their fit will have a large χ^2, which can be used as a rejection criterion. The distribution of the mass residuals have therefore large tails, however the Gaussian width of the core is very similar to the one obtained with a simple global fit (see Fig. 3.20).

The distributions of the residuals of the x and z coordinates of the reconstructed vertex become significantly non-Gaussian. While the core is much narrower with respect to both the Kalman filter and the simple global fit, the RMS is comparable to the Kalman filter, indicating more tails (see Fig. 3.20). Here the distributions are fitted with a superposition of two Gaussian function. The width of the core Gaussian is found to be around 42 μm for the x-coordinate residuals and around 30 μm for the z-coordinate.

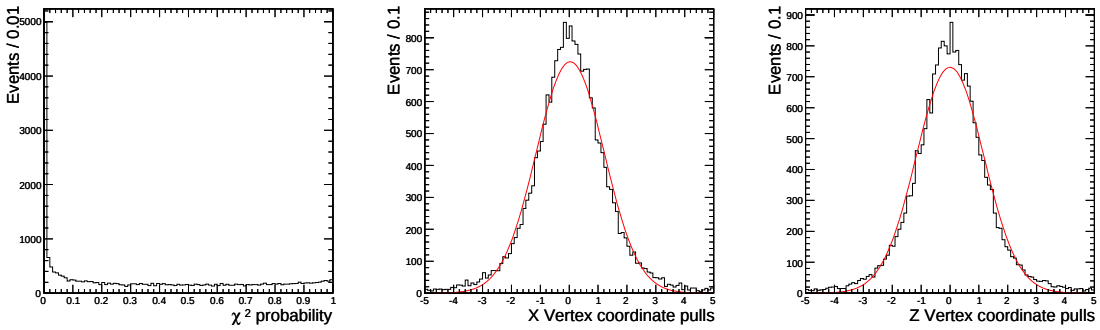

Figure 3.21: Distributions of the total χ^2 probability (**left**), x vertex coordinate pulls (**middle**) and z vertex coordinate pulls (**right**)for the Global fit with pointing constraint.

The vertex position errors are reasonably well estimated: in Fig. 3.21 the distributions of the x and z vertex coordinates pulls are presented. The distribution of the χ^2 probability (7 degrees of freedom) of the global fit with pointing constraint is presented in Fig. 3.21. The distribution is reasonably flat, however due to the discussed effects, the fraction of event with small probability increases significantly with respect to the Kalman filter and the global fit.

It can be noted that after application of the pointing constraint, the coverage on the mass of the B_s^0 meson degrades slightly with respect to the global fit without pointing (see Tab. 3.2). As it can be predicted from the Fig. 3.20, the central part of distributions of both x and z residuals become narrower and 50% coverage improves with respect to both Kalman and global strategy without pointing. The 90% and 95% coverages degrade with respect to the Kalman strategy, indicating more tails.

3.5.4 Sequential strategy

In Fig. 3.22 the distribution of the B_s mass residual for the sequential strategy is shown. The distribution has the same shape as in the global case, but the resolution is slightly worse. The distribution of mass pulls and the total χ^2 probability of the fit are presented in Fig. 3.22. The x and z vertex components resolutions and pulls are also very similar to the results of the Kalman strategy and global fit without pointing. Several other sequential strategies were also studied, e.g. individual reconstruction of both the J/ψ and ϕ mesons, and fitting them to the same vertex, which entails the propagation and the vertex fit of two neutral tracks etc. In all cases, the resolution on the B_s^0-meson mass was found to be very similar (within 3 MeV) once all constraints are applied, as is predicted by the factorization of constraints

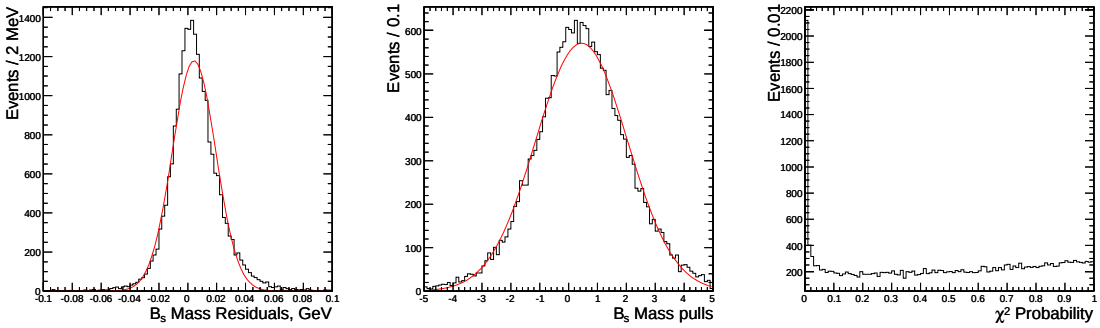

Figure 3.22: Distributions of the B_s^0 mass residuals (**left**), B_s^0 mass pulls (**middle**) and χ^2 probability of the fit(**right**) for the Sequential reconstruction.

theorem. Overall, the global strategy yields somewhat better results. The discrepancies observed between the different approaches come from the precision of the calculations. The global method involves less calculations than all other methods: only one vertex fit and no intermediary propagations are done.

3.5.5 Summary

As it was shown in the last sections, the use of constraint fitting during the reconstruction of the $B_s^0 \to (J/\psi)\phi \to \mu^+\mu^- K^+ K^-$ allows to improve the resolution on the reconstructed mass of the B_s^0 meson from approximately 34 MeV to approximately 14 MeV and removes the bias. Several global and sequential algorithms of constraint fitting were implemented and tested, yielding the same result within numerical precision. The further application of pointing the constraint allows to improve the distributions of residuals of x and z coordinates of secondary vertex. Distributions with the same RMS, but much narrower core, than in the case of Kalman filter are obtained.

Chapter 4

Data selection and analysis

Due to the large multiplicity of tracks in high energy pp collisions at LHC and a very high rate of the background events, the triggering and offline selection of the $B_s^0 \to (J/\psi)\phi \to \mu^+\mu^- K^+ K^-$ events represents a difficult and challenging task. I present here the the high level trigger and offline selection algorithms to be used during the low luminosity run of the LHC. The study was performed using a set of Monte Carlo simulated signal and background events. The reconstruction and selection of events was performed using the version 8.7.3 of ORCA (see Sec. 3.1 and [47]).

4.1 Monte Carlo generated samples

For the current study we have used samples of Monte Carlo generated signal and background events. The 200′000 signal $B_s^0 \to (J/\psi)\phi \to \mu^+\mu^- K^+ K^-$ events were generated with the SIMUB generator [43], which is especially written for this decay. Only the events with the following kinematic parameters were retained for further analysis:

$$\begin{aligned} p_t(\mu) &> 2 \text{ GeV}, \\ p_t(K) &> 0.5 \text{ GeV}, \\ |\eta(\mu, K)| &< 2.5, \end{aligned} \tag{4.1}$$

where p_t is the transverse momentum of a particle and η is its pseudorapidity.

The effective cross section for $B_s^0 \to (J/\psi)\phi \to \mu^+\mu^- K^+ K^-$ at LHC energies can be estimated in the following way:

$$\begin{aligned} \sigma(\text{signal}) = \; & 2 \cdot \sigma(b\bar{b}) \cdot \text{BR}(\bar{b} \to B_s^0) \cdot \text{BR}(B_s^0 \to (J/\psi)\phi) \\ & \cdot \text{BR}(J/\psi \to \mu^+\mu^-) \cdot \text{BR}(\phi \to K^+K^-) \cdot \epsilon_{\text{kine}}, \end{aligned} \tag{4.2}$$

where $\epsilon_{\text{kine}} = (5.81 \pm 0.04)\%$ [62] is the probability to pass the kinematic cuts (4.2), obtained with SIMUB generator and BR denotes branching fraction. The production cross section of the $b\bar{b}$ pairs at LHC is estimated to be $\sigma(b\bar{b}) \approx 500\ \mu$b (see Sec. 1.1). Assuming the following branching fractions for the individual decays [41],

$$\begin{aligned} \text{BR}(\bar{b} \to B_s^0) &= (10.7 \pm 1.1)\%, \\ \text{BR}(B_s^0 \to (J/\psi)\phi) &= (9.3 \pm 3.3) \cdot 10^{-4}, \\ \text{BR}(J/\psi \to \mu^+\mu^-) &= (5.88 \pm 0.10)\%, \\ \text{BR}(\phi \to K^+K^-) &= (49.1 \pm 0.6)\%, \end{aligned}$$

the total cross can be estimated as: $\sigma(\text{signal}) = 167 \pm 62$ pb. The error quoted is dominated by the uncertainties on the $\text{BR}(B_s^0 \to (J/\psi)\phi)$ and $\text{BR}(\bar{b} \to B_s^0)$ and does not include the errors on the estimate of the total $b\bar{b}$ production cross section at LHC. The values of the physical parameters used for the generation of the $B_s^0 \to (J/\psi)\phi$ Monte Carlo sample are presented in the Tab. 4.1 [1]. There the notation of physical observables follows the one used in Sec. 1.2.3.

As mentioned in Sec. 1.2, in the absence of mixing-induced CP violation, the heavy and light mass eigenstates of the B_s^0 meson are also CP eigenstates (CP-odd and CP-even respectively). As it is shown in the Sec. 1.2.3, the decay amplitude can be decomposed into three independent components, corresponding to the linear polarization states of final state mesons: CP-even $A_0(t)$ and $A_\parallel(t)$ and CP-odd $A_\perp(t)$. Since the amplitudes $A_0(t)$ and $A_\parallel(t)$ are CP-even, they would correspond to the decays of B_s^L and the CP-odd amplitude $A_\perp(t)$ would correspond to B_s^H decays. It can be seen therefore that in the current Monte Carlo sample, light (short living) and heavy (long living) mass eigenstates have the following fractions:

$$\begin{aligned} B_s^L \text{ (short living)}: &\quad (|A_0(0)|^2 + |A_\parallel(0)|^2)/\Gamma_s \quad 84\% \\ B_s^H \text{ (long living)}: &\quad |A_\perp(0)|^2/\Gamma_s \quad 16\% \end{aligned}$$

It should be mentioned that the natural width of ϕ meson (4.26 MeV) was not taken into account at the generator level. All selection cuts presented in following sections account for this issue. To account the pile-up of events in the CMS detector, each signal event was superimposed with a mean of 3.5 minimum bias events and several random dimuon combinations.

The distributions of the energy, transverse momentum, flight path in the detector frame, proper decay length and Lorentz factor $1/\beta\gamma = M(B_s^0)/p(B_s^0)$ of the generated B_s^0 mesons are presented in the Fig. 4.1 and 4.2. The mean energy of the B_s^0

Parameter	Value
$\tau_s = 1/\bar{\Gamma}_s$	$1.463 \cdot 10^{-12}$ s
τ_s^L (short)	$1.330 \cdot 10^{-12}$ s
τ_s^H (long)	$1.625 \cdot 10^{-12}$ s
Δm_s	10 ps^{-1}
$\lvert A_0(0)\rvert^2/\Gamma_s$	0.54
$\lvert A_\parallel(0)\rvert^2/\Gamma_s$	0.3
$\lvert A_\perp(0)\rvert^2/\Gamma_s$	0.16
δ_1	0
δ_2	π
ϕ_s	0.04

Table 4.1: Values of physics parameters used for generation of the $B_s^0 \to (J/\psi)\phi$ data sample with SIMUB generator.

mesons is about 24 GeV and the mean transverse momentum is about 12 GeV. The mean flight path of the B_s^0 meson in the detector frame is about 1.5 mm, the mean proper flight path is about 440 μm.

The distributions of the energy, transverse momentum, pseudorapidity and azimuthal angle of the generated final state muons and kaons are presented in Fig. 4.3 and 4.4 respectively. The final state muons have a mean energy of about 7 GeV and transverse momentum of about 4 GeV. The final state kaons have a mean energy of about 4 GeV and transverse momentum of about 2 GeV. The pictures illustrating the layout of trajectories for the typical signal events with and without pile-up can be found in Appendix C.

The background sample used for the current analysis consists of 200′000 $b \to (J/\psi)X$ inclusive events. It contains an admixture of b-flavoured hadrons (B_s^0, B_d^0, Λ_b), decaying to final states with a J/ψ resonance. The same kinematic cuts as in the case of signal are applied $p(\mu) > 2$ GeV, $|\eta(\mu)| < 2.5$. The effective cross section for this background sample can be estimated as:

$$\sigma(\text{background}) = 2 \cdot \sigma(b\bar{b}) \cdot \text{BR}(b \to J/\psi) \cdot \text{BR}(J/\psi \to \mu^+\mu^-) \cdot \epsilon'_{\text{kine}}, \qquad (4.3)$$

[1]The actual values of the frequency of the B_s^0 oscillation, lifetimes of heavy and light components and amplitudes were chosen according to [63] and references therein. The details of the current choice of parameters are provided in [64].

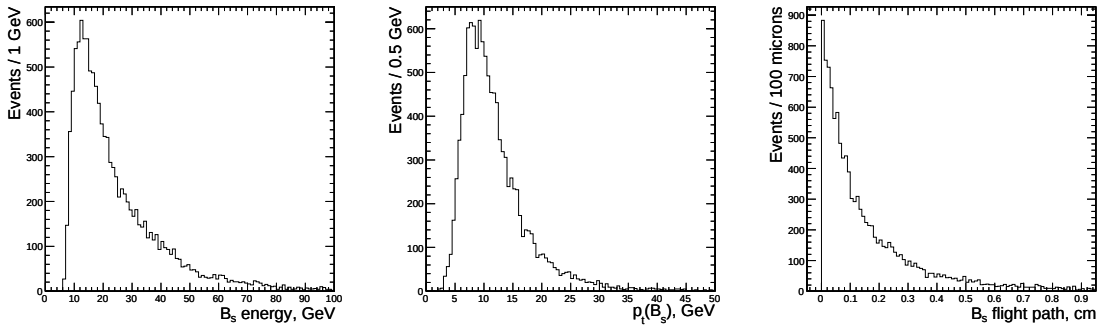

Figure 4.1: Distributions of the energy (**left**), transverse momentum (**middle**) and flight path in detector frame (**right**) of simulated B_s^0 mesons.

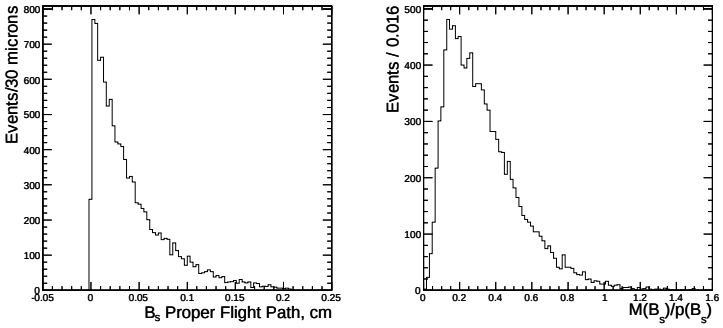

Figure 4.2: Distributions of the proper flight path (**left**), and m/p ratio (**right**) of simulated B_s^0 mesons.

where $\epsilon'_{\rm kine} = (7.53 \pm 0.04)$ % [62] is the probability to pass the kinematic cuts calculated with the SIMUB generator. Taking into account the experimentally measured values [41]:

$$\begin{aligned} \mathrm{BR}(b \to J/\psi) &= (1.16 \pm 0.10)\% \\ \mathrm{BR}(J/\psi \to \mu^+\mu^-) &= (5.88 \pm 0.10)\%, \end{aligned}$$

the cross section can be estimated as:

$$\sigma(\text{background}) = 51.4 \pm 4.8 \text{ nb}. \tag{4.4}$$

The background sample does not include the channel $B_d^0 \to (J/\psi)K^* \to \mu^+\mu^- K^+\pi^-$, which is considered to be an important source of background for both High Level Trigger and offline selections. A preliminary estimate (based on a private Monte Carlo production) of the influence of this channel on the High Level Trigger strategy can be found in [62].

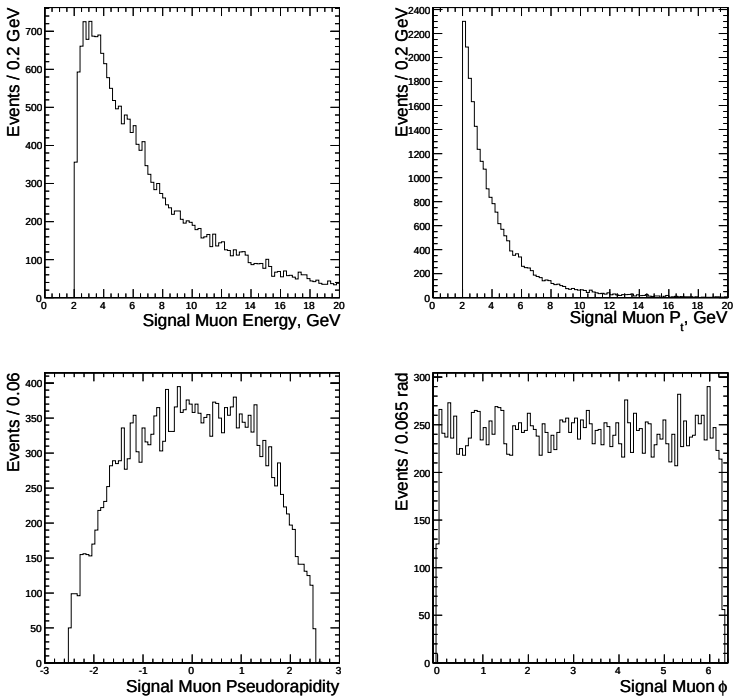

Figure 4.3: Distributions of the energy (**top left**), transverse momentum (**top right**), pseudo-rapidity (**bottom left**) and azimuthal angle (**bottom left**) of simulated final state muons.

Another important source of background is the prompt production of the J/ψ mesons. A preliminary study (based on a private Monte Carlo production) of this background channel at the High Level Trigger was performed in [62]. Some of selection cuts established in [62] will be used in the further discussion of the High Level Trigger. For all these samples, the response of the CMS detector was simulated with the dedicated OSCAR [44] simulation package (see Sec. 3.1).

4.2 Event triggering

As mentioned in Sec. 2.2.6, the CMS experiment uses a two-level trigger algorithm: a hardware-based Level-1 (L1) trigger and a software-based single stage High Level Trigger (HLT), running on a dedicated farm of commercial processors. The HLT reduces the output rate of the L1 trigger (100 kHz) to a value of approximately 100 Hz, limited by present storage capabilities. The bandwidth of 100 Hz should be shared between all physical channels of interest. In the current section, the HLT strategy for the selection of the $B_s^0 \to (J/\psi)\phi \to \mu^+\mu^- K^+ K^-$ events and its implementation in ORCA is discussed.

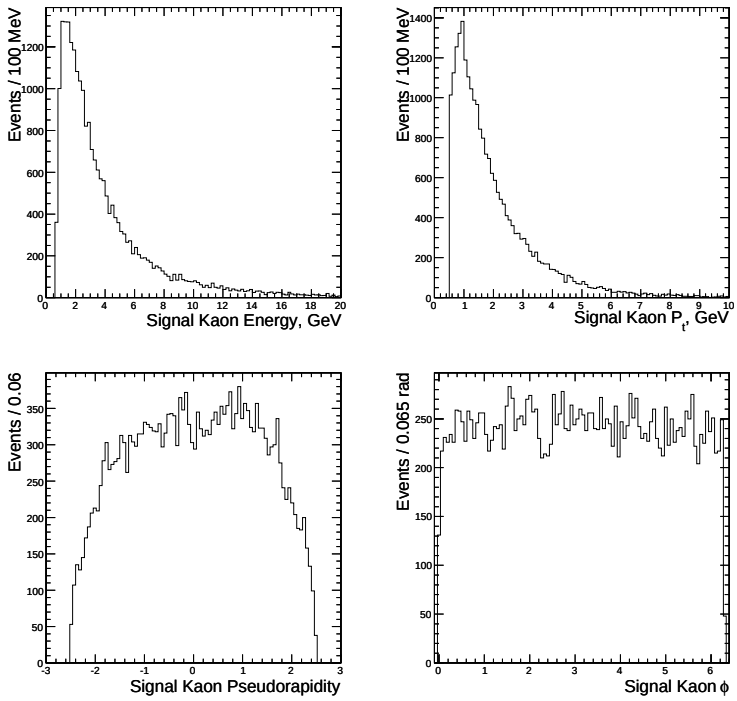

Figure 4.4: Distributions of the energy (**top left**), transverse momentum (**top right**), pseudorapidity (**bottom left**) and azimuthal angle (**bottom left**) of simulated final state kaons.

4.2.1 L1 dimuon trigger

The strategy of the $B_s^0 \to (J/\psi)\phi \to \mu^+\mu^- K^+K^-$ High Level Trigger is based on the Level-1 hardware dimuon trigger. This trigger reconstructs up to four muon candidates with a threshold on the transverse momentum of $p_t^\mu > 3$ GeV. It uses the Resistive Plate Chambers of the muon detector to identify and measure muon tracks with a pattern comparator logic. Muons are reconstructed from correlated patterns of hits in different stations. The transverse momentum, pseudorapidity and the azimuthal angle of trajectories are assigned via look-up tables.

The distribution of transverse momentum and pseudorapidity of signal muon tracks, selected by the dimuon trigger are presented in Fig. 4.5. By requesting at least two muons to be reconstructed by the dimuon trigger results in an efficiency of 38% with respect to the number of processed signal events. A problem in the software emulation of the hardware trigger results in the frequent misidentification of the charge of muons reconstructed in the end caps. Since two muons with opposite charge are requested, this problem decreases the selection efficiency to 28%. The efficiencies and rates of the signal and background events at the L1 dimuon trigger are presented in Tab. 4.2. Distribution of residuals of the transverse momentum

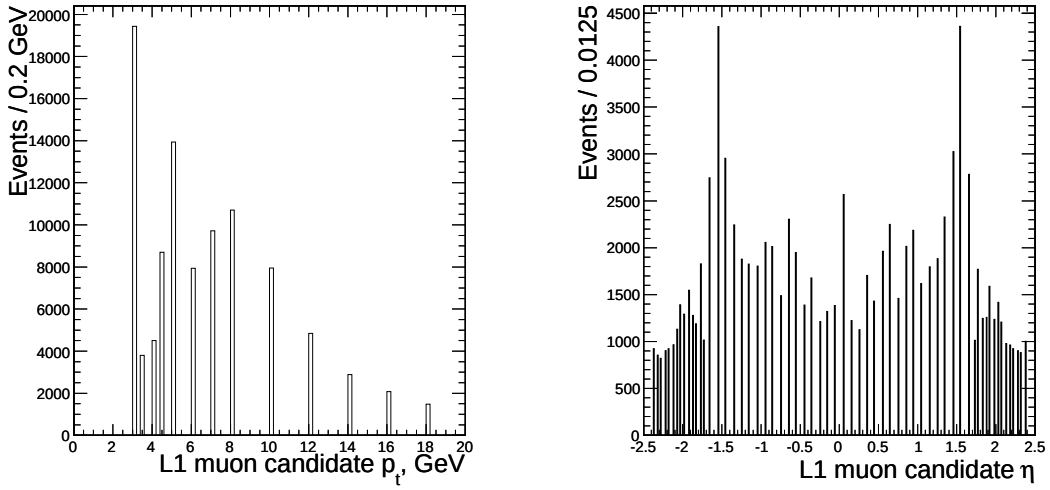

Figure 4.5: Distributions of transverse momentum (**left**) and pseudorapidity (**right**) of muon trajectories reconstructed with L1 dimuon trigger.

Channel	$B_s^0 \to (J/\psi)\phi$	$b \to (J/\psi)X$
L1 efficiency (> 1 muon)	$(38.20 \pm 0.14)\%$	$(33.2 \pm 0.13)\%$
L1 efficiency (opposite charge pair)	$(28.10 \pm 0.12)\%$	$(22.9 \pm 0.11)\%$
L1 rate (> 1 muon), Hz	0.12759	34.1296
L1 rate (opposite charge pair), Hz	0.09385	23.5412

Table 4.2: Efficiencies and rates of the L1 dimuon trigger with respect to signal and background.

and pseudorapidity of signal muons, reconstructed at the L1 dimuon trigger are presented in Fig. 4.6. The distribution of residuals of the transverse momentum is very broad since the dimuon trigger returns discrete values with very coarse binning. It can be seen that the mean of this distribution is shifted for approximately 1 GeV toward higher values. It is believed that this effect comes from the application of the p_t threshold of 3 GeV, mentioned above. All registered muons with the transverse momentum lower that this value are assigned with the transverse momentum of 3 GeV. Due to the small binning, the pseudorapidity of muons is well estimated, the Gaussian width of the distribution is about 0.06.

In Fig. 4.7 the distributions of the residuals of the azimuthal angle of positive and negative signal muons are presented. The distributions of residuals of azimuthal angle for positive and negative muons are shifted to the negative and positive side

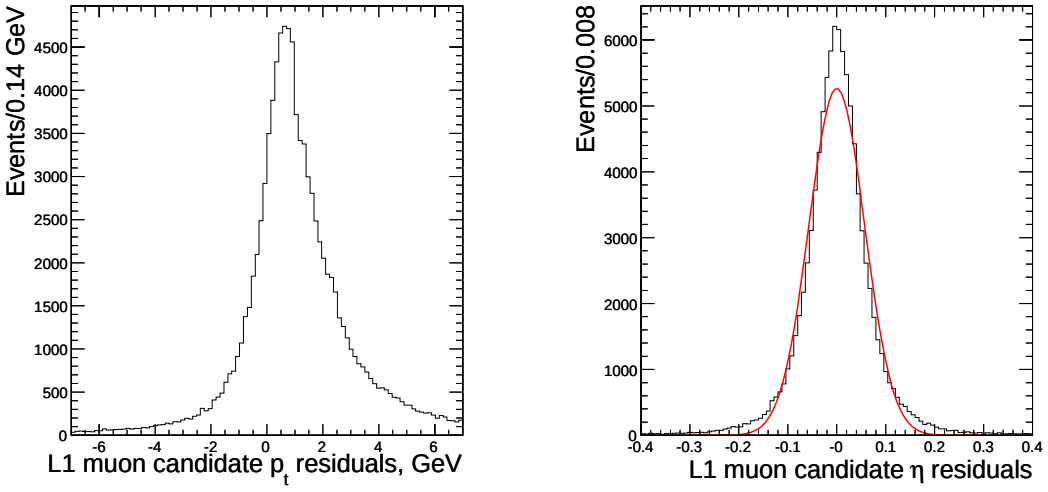

Figure 4.6: Distributions of residuals of the transverse momentum (**left**) and pseudorapidity (**right**) of muons reconstructed at L1 dimuon trigger.

respectively. This problem can be traced to the fact that at L1, the azimuthal angle is measured in the second muon station located in the return yoke. Since the magnetic field is of opposite polarity in the return yoke, the azimuthal angles of the muons at this point will be biased with respect to their values at the production vertex. To correct this bias, the fixed corrections of 0.4 rad and -0.4 rad are applied to the azimuthal angles of positive and negative muon candidates respectively. This ensures that this corrected angle can be used in a subsequent search in the HLT. The resulting distribution of residuals is presented in Fig. 4.7. The Gaussian sigma of the distribution is about 0.22 rad.

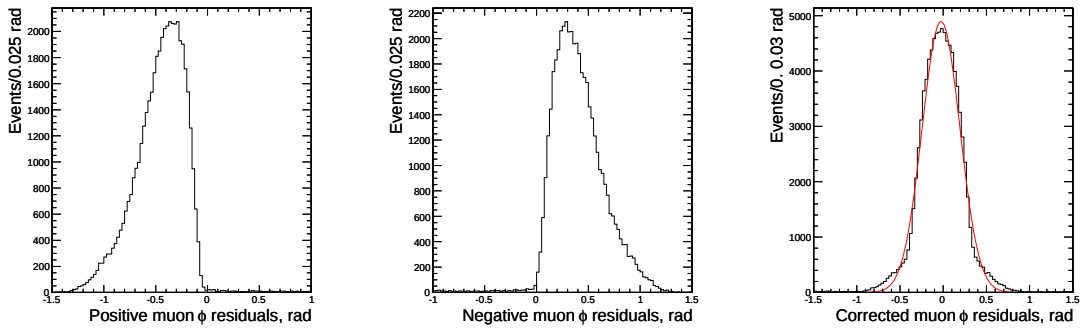

Figure 4.7: Distribution of residuals of the polar angle of muons, reconstructed at L1 dimuon trigger: **left:** positive muons without azimuthal correction, **middle:** negative muons without azimuthal correction, **right:** all muons with azimuthal corrections.

4.2.2 L2 J/ψ trigger

At this stage, the trajectories, corresponding to L1 muon candidates are reconstructed in the central tracker and J/ψ-meson candidates are selected. First the primary interaction vertex (PV) of the current event is detected. At the HLT, the search for the primary vertex is based on the information provided by the Pixel detector and only the longitudinal (z) coordinates are estimated. The transverse position of the primary vertex is constrained by the transverse size of the beam spot (around 15 μm in both x and y directions).

Primary vertex finding

In the current HLT strategy, the primary interaction vertices are reconstructed using so-called Divisive method [65]. The reconstruction relies on the collection of track segments reconstructed using only Pixel detector (so-called *pixel tracks*). At the initial stage, the pixel tracks are first ordered according to their longitudinal impact parameter. In this list, each group of pixel tracks separated from the next group by more than a predefined value z_{sep} is taken as a cluster. After rejecting the outliers from these clusters, the list of rejected tracks is scanned again to see if new clusters can be formed. The position of each cluster is taken as the average of the impact parameters of all tracks belonging to it. The lists of primary vertices thus reconstructed is ordered according to the sum of transverse momenta of the tracks.

The Divisive method reaches 78% vertex finding efficiency for the tagged primary vertex and 97% for the closest primary vertex [66][2]. The distribution of residuals of the z-coordinate of reconstructed primary vertices is presented in Fig. 4.8 (left). The Gaussian width of the distribution is about 77 μm. After the primary vertex candidates are reconstructed, three most probable of them are kept for further analysis.

Partial reconstruction of muon trajectories

The three selected primary vertex candidates are used to define the center of the so-called *rectangular* $(\eta - \phi)$ *tracking region* for the partial reconstruction of muon trajectories. The tracking regions are defined as follows (see Fig. 4.8 (right)):

- The base of the tracking region is defined by the position of the primary vertex candidate. The tolerance 1 cm is taken around the primary vertex.

[2]The efficiencies presented are calculated for the $B_s^0 \to (J/\psi)\phi \to \mu^+\mu^- K^+ K^-$ Monte Carlo generated events with the pile-up, corresponding to the low-luminosity run of the LHC. The tagged PV cluster is defined according to the sum of the transverse momenta of all tracks, belonging to the cluster (see [65] for more details).

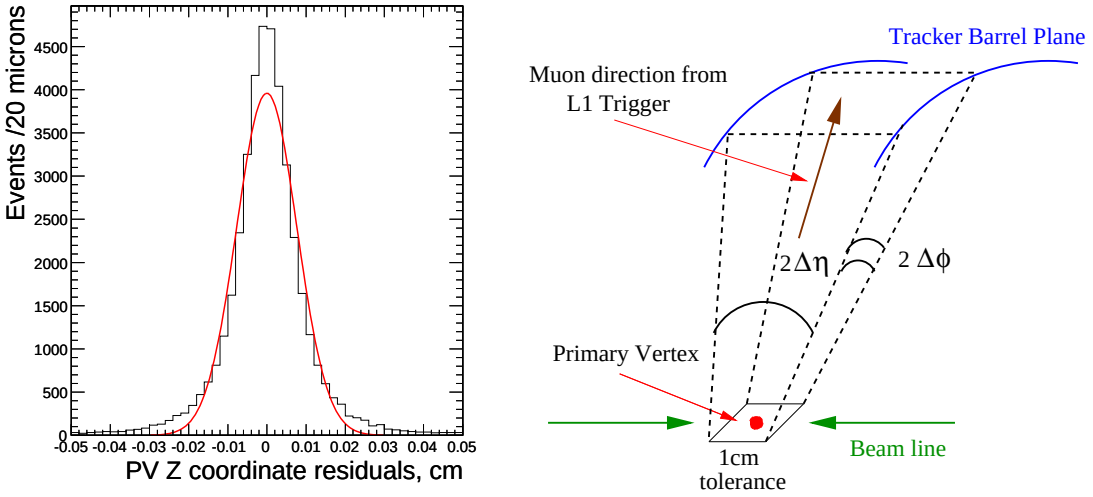

Figure 4.8: Distribution of residuals of the z-coordinate of the primary vertex, reconstructed with the Divisive method (**left**). Rectangular $\eta - \phi$ region for local track reconstruction (**right**).

- The direction of the region is defined by corrected parameters of the muon candidate reconstructed at the L1 (see Sec. 4.2.1).

- The definition of the tracking region is completed by defining the openings of the region in azimuthal angle and pseudorapidity (denoted hereafter as $\Delta\phi$ and $\Delta\eta$) with respect to direction of the L1 muon candidate. The values of $\Delta\eta$ and $\Delta\phi$ were chosen according to distribution of residuals between parameters of simulated trajectories of muons and parameters of muon candidates, reconstructed at L1: $\Delta\eta = 0.15$ and $\Delta\phi = 0.5$ rad.

After the tracking region is defined, all tracks with the transverse momentum above a threshold of 2 GeV are reconstructed in this region. In order to obtain a reasonable estimate of the track parameters, spending minimal time, the reconstruction of each successful trajectory stops after $5 - 6$ hits (the presence of one invalid hit per trajectory is allowed). Of those $2 - 3$ hits are provided by the Pixel detector and the rest by the Silicon Strip Tracker. In Fig. 4.9 the resolution of track parameters reconstructed with combinatorial approach as a function of number of hits, used in reconstruction is presented. It can be seen that the resolutions increases with number of hits and reaches asymptotic resolution obtained using the full tracker. It can also be noted, that the track reconstruction using 5 or 6 hits provide a reasonable estimate of track parameters with the resolution close to the one obtained using full CMS tracker.

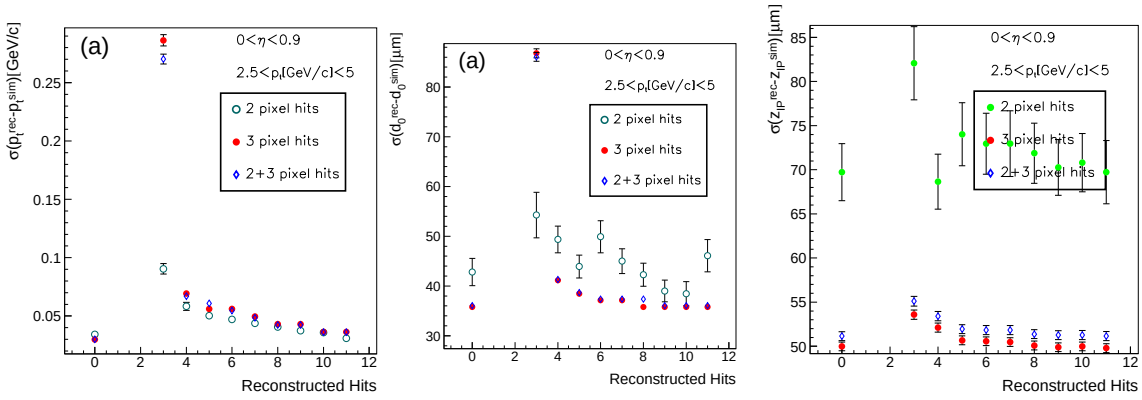

Figure 4.9: Resolution of the trajectory parameters as a function of number of hits, used in the reconstruction. **left**: transverse momentum, **middle:** transverse impact parameter, **right:** longitudinal impact parameter. "0 hits" indicates the full tracker reconstruction.

In the High Level Trigger strategy proposed in [62], a two-step partial track reconstruction was used. After the tracking region was defined, the hit triplets, compatible with this region were reconstructed in the Pixel detector. The reconstructed triplets were used then as seeds for combinatorial track reconstruction. The reconstruction was stopped after trajectory candidates were reaching the second (or third, in case invalid hit was present) surface of the Silicon Strip Detector.

It was found that this approach has one significant drawback: requesting each trajectory to contain three hits in the Pixel detector leads to considerable inefficiencies in partial track reconstruction. The efficiency of reconstruction of the single track drops below 80% [62], while as it was shown in Sec. 3.2, the efficiency close to 100% is achievable with the Combinatorial Track Finder in most of the coverage of the CMS Tracker. An important difference between these approaches is that the Combinatorial Track Finder does not require each trajectory to leave hits in all three surfaces of pixel detector, allowing therefore the use of pixel hit doublets. It was therefore decided to use the Combinatorial Track Finder in the current HLT strategy.

Selection of J/ψ candidates

For all track pairs of opposite charge thus reconstructed, the invariant mass is calculated with the assumption that all tracks are muons (Fig. 4.10). The resolution on the mass of the J/ψ-meson with the partial track reconstruction is about 54 MeV. Dimuon combinations with invariant mass within 150 MeV of the mean value of the reconstructed J/ψ peak are retained. For each oppositely J/ψ candidate the two muon tracks are fitted to a common vertex using a Kalman Vertex Fitter (c.f.

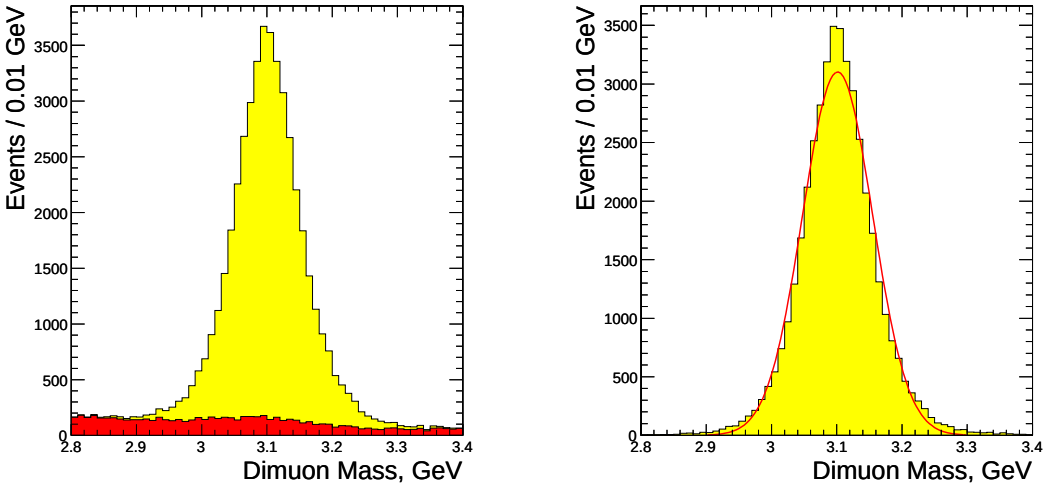

Figure 4.10: Distribution of invariant mass of selected dimuon combinations. **Left:** signal dimuons (in yellow) and combinatorial background (in red). **Right:** correct dimuon combinations only.

Sec. 3.3), and candidates for which the χ^2 of the vertex is above 10 (n.d.f = 1) are rejected. The transverse decay length L_t of each J/ψ candidate is calculated and its significance (L_t/σ_{L_t}, where σ_{L_t} is the reconstruction error) is required to be above 3. Finally, the momentum of the J/ψ candidate reconstructed at the secondary vertex is required to be aligned with the primary vertex in the transverse plane: $\cos\alpha > 0.9$, where α is the angle between the vector, pointing from primary to secondary vertex in the transverse plane and transverse momentum of the J/ψ meson reconstructed at the secondary vertex. The efficiencies of selection of signal and background events at different stages of the L2 J/ψ trigger are summarized in the table 4.3 [3].

4.2.3 L3 $B_s \to (J/\psi)\phi$ trigger

At the last stage of the High Level Trigger selection, the ϕ and B_s^0 meson candidates are reconstructed. The selection at L3 begins with a partial reconstruction of trajectories of kaon candidates. The tracking region is centered at the primary vertex of the J/ψ candidate and the direction is that of its momentum.

In Fig. 4.11 the distributions of the azimuthal angle and pseudorapidity between the J/ψ candidate and the simulated signal kaons are presented. These distributions define the opening angles of the tracking regions ($|\Delta\eta| < 0.9$ and $|\Delta\phi| < 0.9$).

[3] All the efficiencies presented are calculated with respect to the total number of events processed and include the efficiency of the L1 dimuon trigger.

Requirement	$B_s^0 \to (J/\psi)\phi$	$b \to (J/\psi)X$
L1 opposite charge muons	$(28.10 \pm 0.12)\%$	$(22.9 \pm 0.11)\%$
Primary vertex search	$(28.1 \pm 0.1)\%$	$(22.9 \pm 0.1)\%$
J/ψ mass requirement	$(23.0 \pm 0.1)\%$	$(17.67 \pm 0.09)\%$
Requirements on secondary vertex	$(20.09 \pm 0.09)\%$	$(14.49 \pm 0.08)\%$

Table 4.3: Efficiencies of selection of signal and background events at different stages of L2 J/ψ trigger.

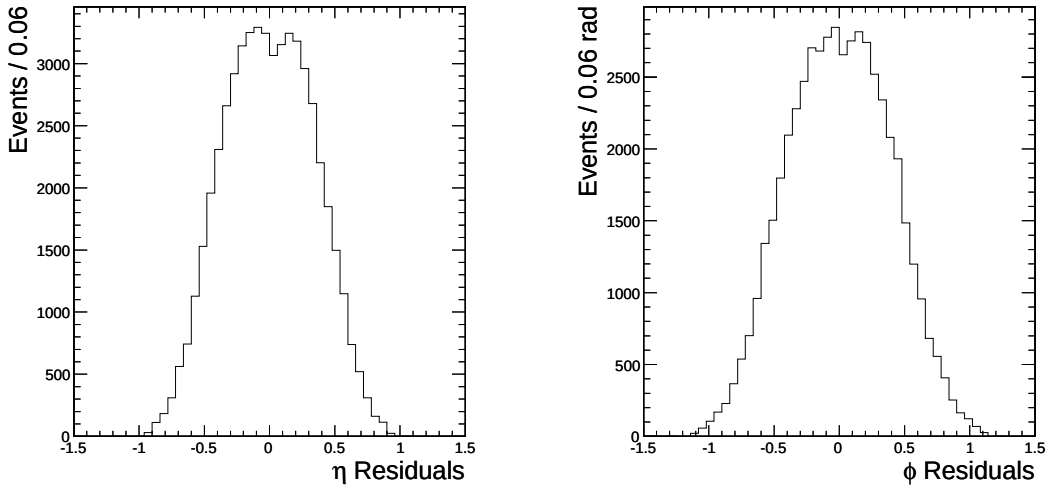

Figure 4.11: Distribution of residuals between the reconstructed parameters of the J/ψ meson and parameters of reconstructed kaons. **Left:** pseudorapidity η, **right:** azimuthal angle ϕ.

All trajectories with the transverse momentum above 0.8 GeV are reconstructed in the tracking regions. The maximal number of 6 hits (including one invalid hit) is allowed per reconstructed trajectory.

For all track pairs of opposite charge thus reconstructed, the invariant mass is calculated with the assumption that the reconstructed tracks are kaons (Fig. 4.12 left). The increase of number of combinatorial background events in the region of the ϕ peak is due to inefficiencies in the association of partially reconstructed tracks to simulated tracks. In the Fig. 4.12 (right) the distribution of invariant mass of kaon pairs associated with the signal is presented. The resolution on the mass of ϕ meson is of approximately 2.5 MeV.

As it was mentioned in the Sec. 4.1, the natural width of the ϕ meson was not taken into account at the generator level. In order to account for this issue, the ϕ

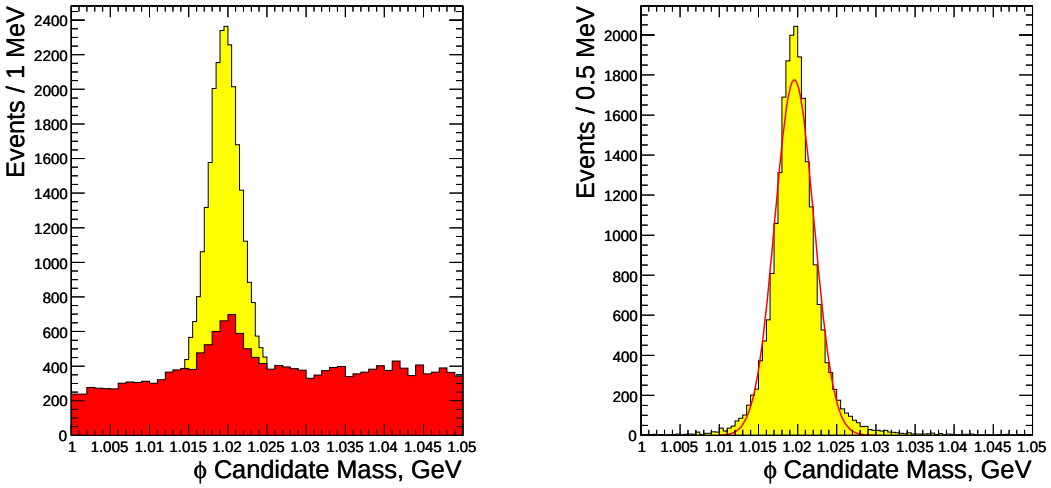

Figure 4.12: Distribution of the invariant mass of ϕ candidates. **Left:** correct combinations (in yellow) and combinatorial background (in red). **Right:** correct combinations only.

candidates with invariant mass within 20 MeV of the mean value of the reconstructed peak are retained.

Selected ϕ candidates are combined with dimuon candidates reconstructed at L2 and the invariant mass of four-track combinations is calculated. The distribution of invariant mass of four-particle candidates is presented in Fig. 4.13. The increase of the number of combinatorial background events in the region of the B_s^0 peak (see Fig. 4.13 left) is due to association inefficiencies mentioned above. The resolution on the B_s^0 mass with partial track reconstruction is found to be around 63 MeV. The four track candidates with invariant mass within 190 MeV of the mean value of the reconstructed B_s^0 peak are selected for further analysis.

For each successful $(\mu^+\mu^-K^+K^-)$ combination the secondary vertex is fitted with the Kalman Filter algorithm. The same requirements as those made on the secondary vertex of J/ψ candidates are applied again to the B_s^0. The distribution of invariant mass of selected combinations after all the cuts is presented in Fig. 4.14. The mass peak in the combinatorial background can be attributed to the same misassociation problem described above. The total efficiencies and rates of the High Level Trigger with respect to signal and background events are discussed in the next section.

4.2.4 Summary

The efficiencies and event rates of the High Level Trigger strategy described above are presented in the Table 4.4. The event rates for both signal and $b \to (J/\psi)X$

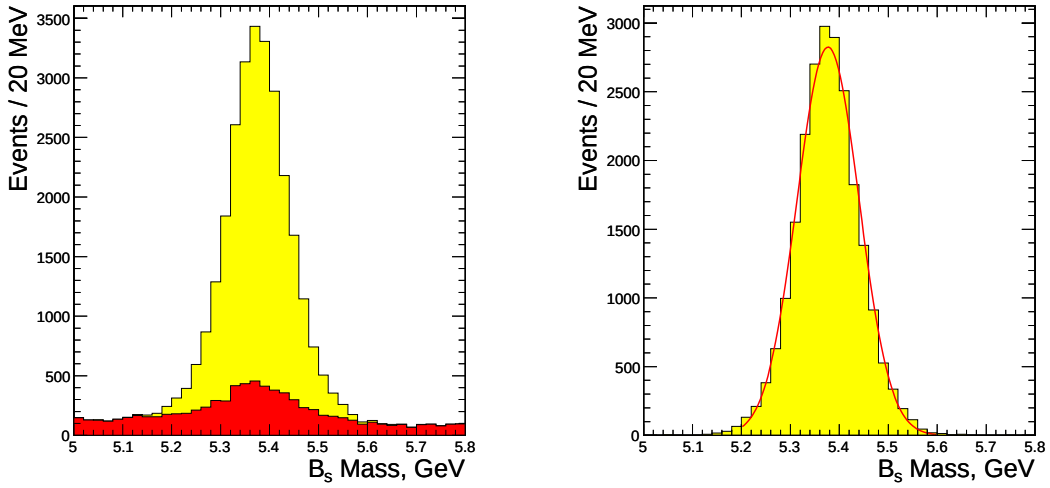

Figure 4.13: Distribution of the invariant mass of selected ($\mu^+\mu^-K^+K^-$) candidates. **Left:** correct combinations (in yellow) and combinatorial background (in red). **Right:** correct combinations only.

background events are of the order of $\mathcal{O}(10^{-2})$ Hz, which is much smaller than the maximum allowed HLT output rate of 100 Hz. The study performed in [62] shows that the rates of the background channels not considered in this study (such as prompt J/ψ for instance) will be even smaller.

After two to three years of operation in the low luminosity mode, the CMS experiment will accumulate around 30 fb^{-1} of data. Assuming the High Level Trigger strategy discussed above, some $508'014 \pm 188'631$ of $B_s^0 \to (J/\psi)\phi \to \mu^+\mu^-K^+K^-$ decays could be written on the tape. The error quoted includes the statistical error of selection and dominated by the errors on the estimated cross section.

With respect to the selection presented in [62], the strategy presented in the

Channel	$B_s^0 \to (J/\psi)\phi$	$b \to (J/\psi)X$
Events Processed	183000	187000
Events Selected	18553 ± 129	91 ± 9
Selection Efficiency	$(10.14 \pm 0.07)\%$	$(4.87 \pm 0.51) \cdot 10^{-4}$
Expected Cross Sections (nb)	0.167 ± 0.062	51.4 ± 4.8
Event Rates (Hz)	$(3.387 \pm 1.26) \cdot 10^{-2}$	$(5.006 \pm 0.702) \cdot 10^{-2}$

Table 4.4: Efficiencies and rates of the trigger selection for signal and background events.

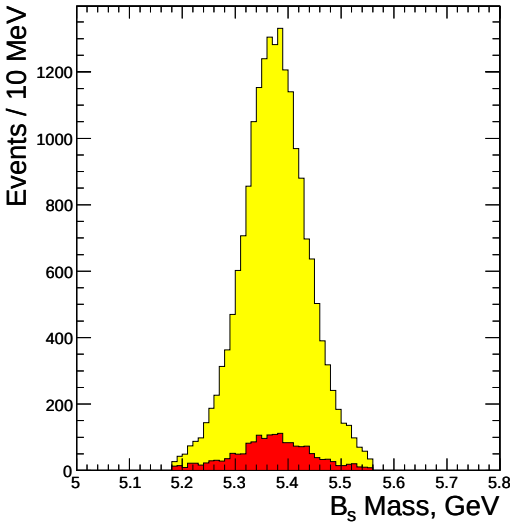

Figure 4.14: Distribution of the invariant mass of $(\mu^+\mu^- K^+K^-)$ candidates after all HLT cuts. Correct combinations (in yellow) and combinatorial background (in red).

previous pages would improve the efficiency of selection of signal events from $5.3 \pm 0.1\%$ to $10.14 \pm 0.07\%$. This increase is mostly due to the fact that in presented strategy the full combinatorial approach to the track reconstruction is used and trajectories are not restricted to have hits in all three surfaces of the Pixel detector.

While this increases also the selection efficiency of the $b \to (J/\psi)X$ background by some 25% (from $(3.9 \pm 0.7) \cdot 10^{-4}$ to $(4.866 \pm 0.510) \cdot 10^{-4}$), the overall signal to background ratio is still significantly improved:

$$\left(\frac{R(S)}{R(B)}\right)_{\text{previous}} = 0.458\ , \quad \left(\frac{R(S)}{R(B)}\right)_{\text{new}} = 0.6766,$$

where R is the event rate of the corresponding channel. Preliminary studies shows that the background level at HLT could still be reduced. For this the following options should be studied:

- Due to the small natural width of the J/ψ resonance, the invariant mass of two muons could be replaced with the world-average mass of the J/ψ meson during the reconstruction of the B_s^0 candidates at L3. According to the study presented in [40] this may significantly reduce the width of the reconstructed distribution of the B_s^0 mass. Consequently, a tighter cut on the invariant mass of reconstructed B_s^0 candidates could be applied. Optionally, a full Kinematic Fit could also be done. The latter possibility depends much on the CPU performance of the algorithm chosen for the kinematic fit.

- The background level appears to be very sensitive to the transverse momentum threshold of reconstructed kaon candidates and angular size of the tracking region in which the kaon candidates are searched. The background level can still be lowered, tuning this quantities accordingly. However, the present choice of these values seems to be the most reasonable, according to the signal over background ratio.

4.3 Offline selection

In this section the offline selection strategy of the $B_s^0 \to (J/\psi)\phi \to \mu^+\mu^- K^+ K^-$ events is presented. The current approach consists in the use of the muon chambers for the identification and reconstruction of muon candidates and a combinatorial search of the kaon candidates in the narrow cone around the direction of the reconstructed J/ψ meson. The selection is completed with the full kinematic fit of the B_s^0 decay vertex. All selection efficiencies quoted hereafter are calculated with respect to the total number of processed events and include both HLT and offline cuts.

4.3.1 Muon reconstruction

Currently two methods of muon reconstruction are implemented in ORCA. In the first (*L3MuonReconstructor*), the reconstruction starts from a seed given by the L1 muon trigger. The muon chambers compatible with the seed are identified and the trajectory is reconstructed in the muon detector using a Kalman filter technique. At the next stage of the reconstruction, the hits in the inner tracker are included: the tracking region is defined by the direction of the muon candidate reconstructed in the muon chambers and all the trajectories in the region are reconstructed using the combinatorial Kalman filter approach discussed in Sec. 3.2. At the last stage a new fit of all trajectory candidates, including the information from both tracker and muon chambers is performed. The resulting set of reconstructed tracks is cleaned, using the total χ^2 of the last fit as rejection criterion. Since the L3 Muon Reconstructor uses the output of the L1 trigger to produce muon seeds, this strategy is not efficient for the reconstruction of muons with low transverse momentum, such as those from the decay $B_s^0 \to J/\psi \to \mu^+\mu^- K^+ K^-$ (the L1 p_t threshold for dimuons at low luminosity is set at 3 GeV).

Another approach to the reconstruction of muon trajectories is provided with so-called *GlobalMuonReconstructor*. Contrary to the L3MuonReconstructor, this algorithm uses muon track segments reconstructed in muon chambers to create the

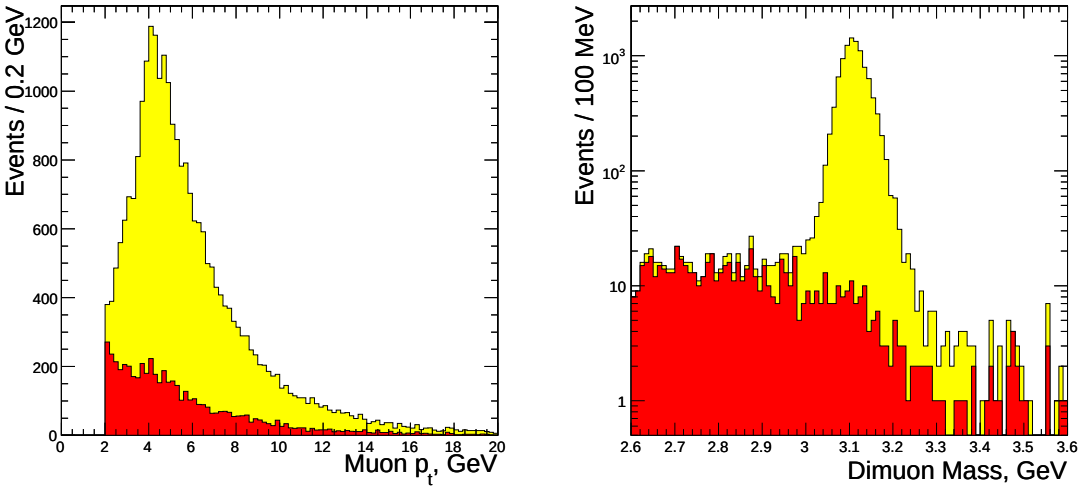

Figure 4.15: Left: Distribution of transverse momentum of muons reconstructed with combined strategy: signal muons (in yellow), muons from the pile-Up and combinatorial background (in red). **Right:** Distribution of the invariant mass of reconstructed muon pairs: correct combinations (yellow), pile-Up and combinatorial background (red).

trajectory seeds. The rest of the reconstruction strategy is completely analogous to the one used in the L3 Muon Reconstructor. This algorithm allows the reconstruction of muons with transverse momenta below 3 GeV.

In order to recover the reconstruction efficiency of muons with low p_t, the following reconstruction strategy is used: the results of both L3 and Global muon reconstruction are combined. The resulting set of trajectories is cleaned according to the number of shared hits. A cut of $p_t > 2$ GeV is applied on the transverse momentum of reconstructed muons. The resulting efficiency to reconstruct at least two muons in the triggered signal events is around 73%. The distribution of transverse momentum of the reconstructed muons is presented in Fig. 4.15 (left). It can be seen that muons with transverse momenta below 3 GeV represent a significant fraction of total number selected muons. The muon mass is then assigned to the reconstructed trajectories and the invariant mass of all oppositely charged dimuon combinations is calculated. The distribution of invariant mass of dimuon combinations is presented in Fig. 4.15 (right). The peak of the J/ψ meson is clearly seen and the level of the combinatorial background is negligible. The distribution of invariant mass of the dimuon candidates, associated with the simulated J/ψ is presented in Fig. 4.16. The mass peak of the J/ψ meson is centered around 3.112 GeV. The experimental resolution for the mass of the J/ψ-meson is estimated to be around 31 MeV (the standard deviation of the Gaussian fit quoted). The dimuon combinations with in-

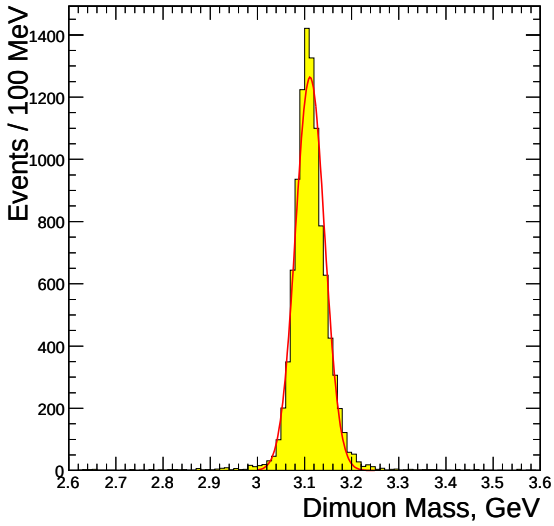

Figure 4.16: Distribution of invariant mass of signal dimuon combinations.

variant mass lying in 4σ region around the mean value of the reconstructed J/ψ peak are selected for further analysis.

4.3.2 Identification of kaons

The kaon candidates for the offline reconstruction of the ϕ mesons, coming from the $B_s^0 \to (J/\psi)\phi$ decay are reconstructed using the combinatorial approach. At the first stage, all the tracks within a cone of $\Delta R = \sqrt{\Delta\eta^2 + \Delta\phi^2} < 2$, where η is pseudorapidity and ϕ is azimuthal angle are fully reconstructed in the Tracker. The kaon mass is assigned to the reconstructed tracks and the invariant mass of all oppositely charged pairs is calculated. The distribution of invariant mass of reconstructed ϕ candidates is presented in Fig. 4.17 (left). In Fig. 4.17 (right), the distribution of invariant mass of ϕ candidates associated with the simulated ϕ mesons is presented. The mass peak of the ϕ meson is centered around 1.02 GeV. The resolution on the mass of the reconstructed ϕ meson was found to be approximately 1.7 MeV. As mentioned above, the natural width of the ϕ meson was not taken into account at the generator level, therefore the distributions presented in Fig. 4.17 account for detector resolution only. The ϕ candidates with invariant mass within 12 MeV around the mean of the reconstructed ϕ peak are selected for further analysis.

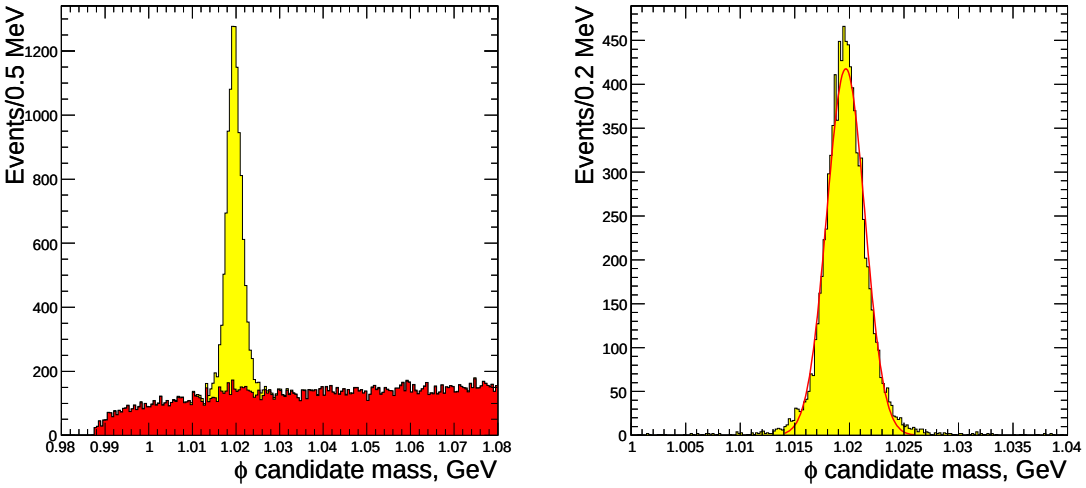

Figure 4.17: Distribution of invariant mass of reconstructed (K^+K^-) candidates. **Left:** all combinations, **right:** combinations associated with signal.

4.3.3 Reconstruction of the B_s meson parameters

After the reconstruction of J/ψ and ϕ candidates is performed the B_s^0 candidates are reconstructed through the kinematic fit, where the invariant mass of two muons is constrained to be equal to the world-average mass of the J/ψ meson. The kinematic fit is performed using the Global reconstruction strategy (c.f. Sec. 3.4). The distribution of the invariant mass of the B_s^0 candidates thus reconstructed is presented in Fig. 4.18. In Fig. 4.19 the distribution of mass of reconstructed B_s^0 candidates is presented as a function of the χ^2 probability of the kinematic fit. It can be seen that in the B_s^0 mass peak, the χ^2 probability of the candidates is flat with a large peak at low probability. This peak can be attributed to a large extend to non-Gaussian tails in the distribution of the measurement errors.

For most of the candidates belonging to the combinatorial background, the χ^2 probability is close to 0. The χ^2 probability of the candidates is therefore required to be above $5{\cdot}10^{-4}$. This requirement significantly reduces the number of background events while affecting minimally the signal.

The distributions of the invariant mass of the reconstructed B_s^0 candidates is presented in Fig. 4.20 (left). The combinatorial background decreased because of the χ^2 probability cut, while the signal peak stay preserved. In Fig. 4.20 (right) the mass distribution of signal B_s^0 candidates is presented. The mean of the B_s^0 peak is of 5.373 GeV and the resolution is about 13.6 MeV (standard deviation of the Gaussian fit quoted). The B_s^0 candidates with invariant mass lying in the region

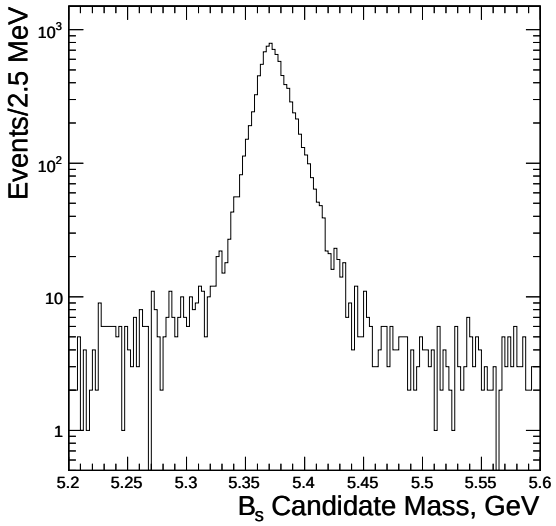

Figure 4.18: Distribution of invariant mass of the reconstructed B_s^0 candidates.

$|\Delta m(B_s^0)| < 67$ MeV are selected for further analysis. The joint efficiencies of the High Level Trigger and offline selection with respect to signal and background events are discussed in the Sec. 4.3.5.

The distributions of residuals of x and z coordinates of the B_s^0 decay vertex reconstructed with the kinematic fit is presented in Fig. 4.21. The resolution of about 54 μm is obtained for the x coordinate of the secondary vertex. The distribution of residuals of the z coordinate of the secondary vertex is highly non-Gaussian, as mentioned in the Sec. 3.5.2. The distribution has a Gaussian core with sigma of about 48 μm and significant tails.

Finally, the cut on the angle between the transverse momentum of the B_s^0 candidate and the transverse direction of its flight path (denoted hereafter as $\alpha_\perp$), already applied at the HLT (c.f. Sec. 4.2.2 and 4.2.3) is applied again: $|\cos\alpha_\perp| > 0.9$. In addition to removing the combinatorial background, this cut removes also a significant fraction of badly reconstructed events. The distribution of the absolute value of $\cos\alpha_\perp$ is presented in Fig. 4.22.

4.3.4 Primary vertex search

The offline reconstruction of the $B_s^0 \to (J/\psi)\phi \to \mu^+\mu^- K^+ K^-$ events is completed with identification of the primary vertex. The reconstruction of the primary vertex of the interaction is performed with the Principal Vertex Finder using Adaptive Vertex Fitter discussed in the Sec. 3.3.2. The distributions of residuals of x and z

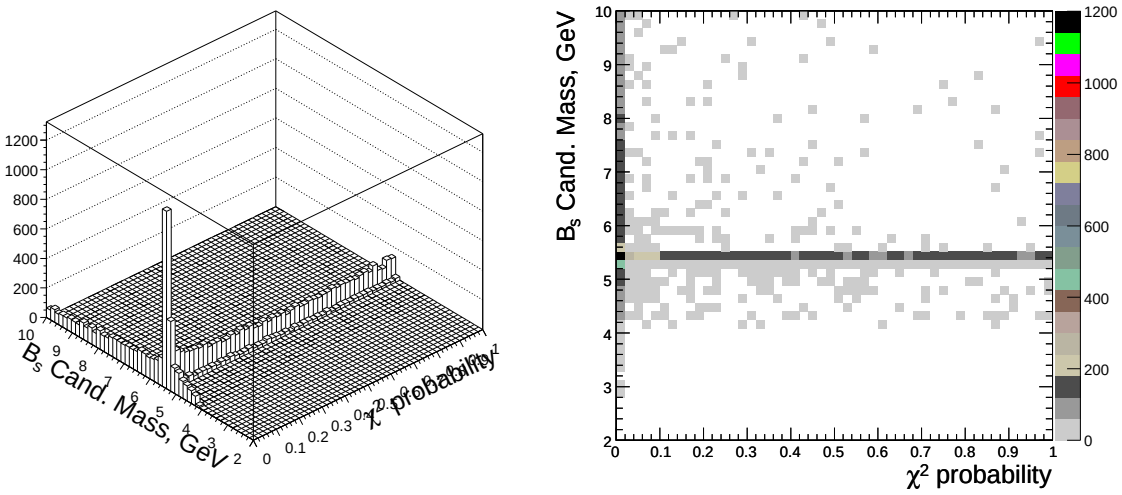

Figure 4.19: Distribution of invariant mass of reconstructed B_s^0 candidates vs the χ^2 probability of the fit.

coordinate of reconstructed primary vertex are presented in Fig. 4.23. The x and z coordinates of the primary vertex are reconstructed with resolutions of 33 μm and 45 μm respectively. The efficiencies of the offline selection cuts with respect to signal and background events are presented in the Tab. 4.5.

4.3.5 Summary

The selection efficiencies of the complete reconstruction chain, including the High Level Trigger and offline selection together with event yields are presented in the tables 4.6 (signal events) and 4.7 (background). After accumulating 30 fb^{-1} of data, $242'383 \pm 87'411$ signal events can be reconstructed in the CMS detector, using the strategy presented above. As in case of the HLT, the error on the total number of events is dominated by the estimated error on the total cross section.

The number of combinatorial background events is found to be insignificant comparing to the signal. According to the study [62], the prompt J/ψ background events are also insignificant. The dominant contribution to the background becomes therefore from $b \to (J/\psi)X$ events: $41'634 \pm 18'535$ reconstructed events for 30 fb^{-1} of collected data. Due to the limited statistics (only 5 events are reconstructed with full selection chain), this estimate suffers from large statistical errors. A sample of background events several times larger that the present one is needed to obtain a stable estimate.

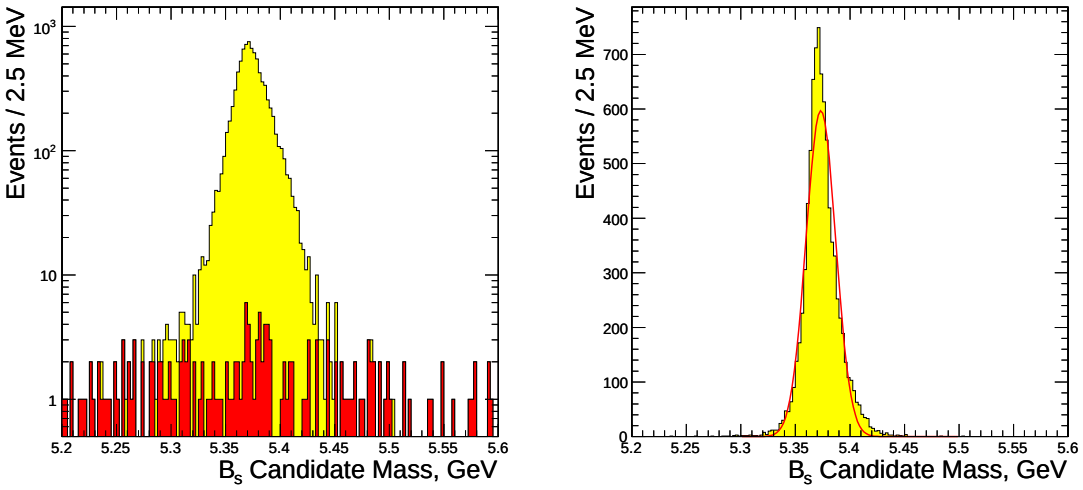

Figure 4.20: Distribution invariant of mass of reconstructed B_s^0 candidates after the χ^2 probability cut. **Left:** signal (in yellow) and combinatorial background (in red). **Right:** signal only.

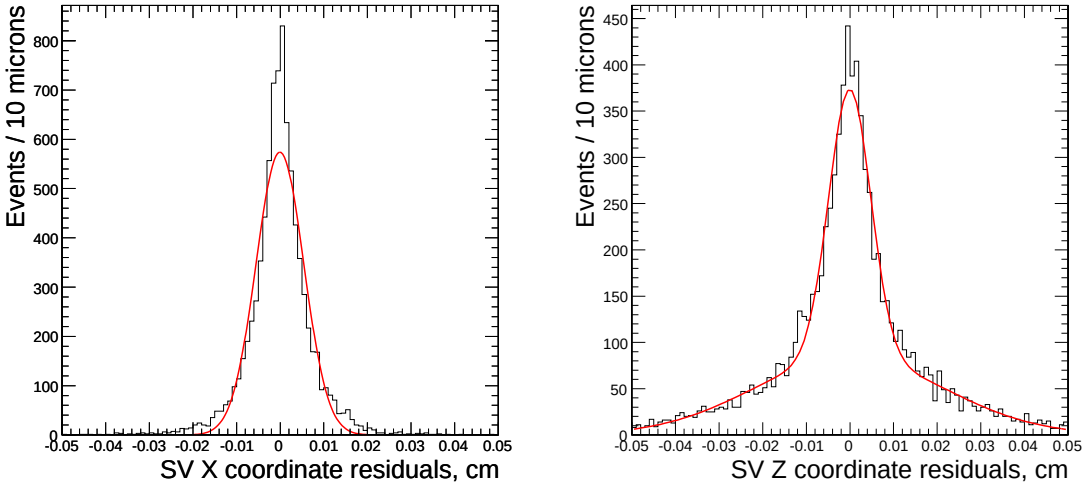

Figure 4.21: Distribution of residual of x (**left**) and z (**right**) coordinates of the reconstructed secondary vertex.

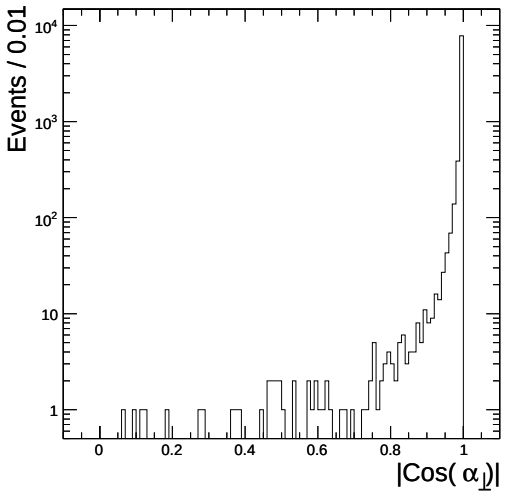

Figure 4.22: Distribution of the absolute value of cosine of angle between the transverse momentum of B_s^0 meson and transverse direction of its flight path.

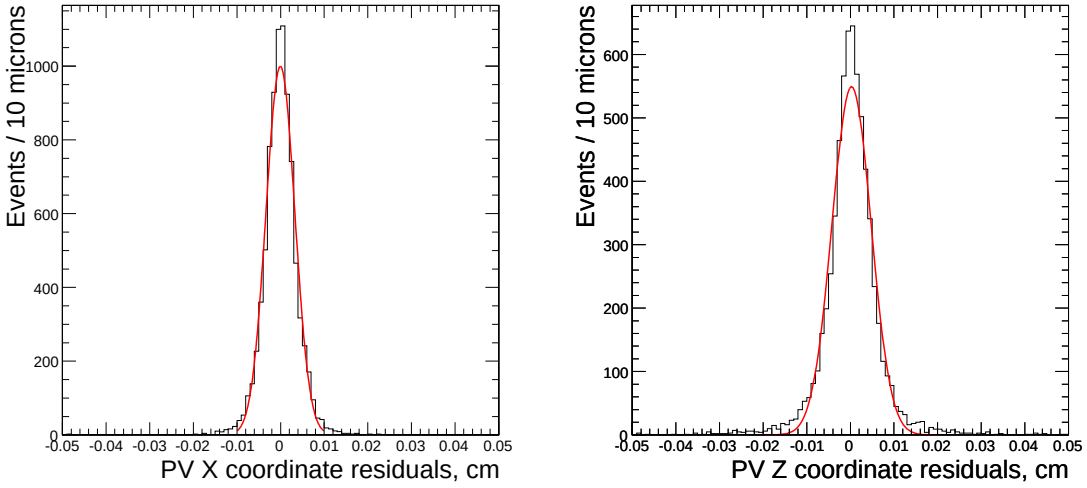

Figure 4.23: Distribution of residual of x (**left**) and z (**right**) coordinates of the reconstructed primary vertex.

Selection stage	$B_s^0 \to (J/\psi)\phi$	$b \to (J/\psi)X$
High Level Trigger	$(10.14 \pm 0.07)\%$	$(4.87 \pm 0.51) \cdot 10^{-4}$
Muon pair search	$(8.89 \pm 0.07)\%$	$(4.21 \pm 0.47) \cdot 10^{-4}$
Muon p_t requirement	$(7.40 \pm 0.06)\%$	$(3.04 \pm 0.40) \cdot 10^{-4}$
ϕ candidate found	$(5.49 \pm 0.05)\%$	$(1.49 \pm 0.28) \cdot 10^{-4}$
χ^2 probability requirement	$(5.04 \pm 0.05)\%$	$(1.22 \pm 0.25) \cdot 10^{-4}$
Primary vertex search	$(4.99 \pm 0.05)\%$	$(1.17 \pm 0.25) \cdot 10^{-4}$
B_s^0 mass requirement	$(4.87 \pm 0.05)\%$	$(2.7 \pm 1.2) \cdot 10^{-5}$

Table 4.5: Efficiencies of the offline selection cuts with respect to signal and background events.

Channel	$B_s^0 \to (J/\psi)\phi$	
Events Processed	174725	
Events Selected	8520	
Association	Signal	Comb. Background
N. of Associated	8453	67
Selection Efficiency	$(4.84 \pm 0.05)\%$	$(3.8 \pm 0.47) \cdot 10^{-4}$
Cross Section (nb)	0.167 ± 0.0602	
Event yield (30 fb^{-1})	$242'383 \pm 87411$	$7'638 \pm 730$

Table 4.6: Efficiencies and event yields of the HLT+offline selection chain with respect to the $B_s^0 \to (J/\psi)\phi \to \mu^+\mu^- K^+ K^-$ events.

Channel	$b \to (J/\psi)X$
Events Processed	$187'750$
Events Selected	5
Selection Efficiency	$(2.7 \pm 1.2) \cdot 10^{-5}$
Cross Section (nb)	51.4 ± 4.8
Event yield (30 fb^{-1})	$41'634 \pm 18'505$

Table 4.7: Efficiencies and event yields of the HLT+offline selection chain with respect to the $b \to (J/\psi)X$ background.

Chapter 5

Results and discussion

The aim of the current study is the measurement of the mean proper decay length of the B_s^0 meson and decay lengths of heavy and light mass eigenstates τ^H and τ^L with the CMS detector. In this chapter, the resolution on the proper decay length of the B_s^0 meson and the possibility of distinguishing between proper decay lengths of its heavy and light mass eigenstates are discussed. The current analysis is based on the sample of 8520 $B_s^0 \to (J/\psi)\phi \to \mu^+\mu^- K^+ K^-$ events, selected by the High Level Trigger and offline selection (c.f. Ch.4).

5.1 The resolution on the proper decay length of the B_s^0 meson

The calculation of the proper decay length of the B_s^0 meson starts with the reconstruction of its production and decay vertices (see Sec. 4.3). The flight paths of the B_s^0 meson in the laboratory frame is then calculated in three dimensions and in the transverse plane:

$$\begin{aligned} L &= \sqrt{(x_{\rm pri} - x_{\rm sec})^2 + (y_{\rm pri} - y_{\rm sec})^2 + (z_{\rm pri} - z_{\rm sec})^2}, \\ L_\perp &= \sqrt{(x_{\rm pri} - x_{\rm sec})^2 + (y_{\rm pri} - y_{\rm sec})^2}, \end{aligned}$$

where $(x_{\rm pri}, y_{\rm pri}, z_{\rm pri})$ and $(x_{\rm sec}, y_{\rm sec}, z_{\rm sec})$ are the coordinates of reconstructed primary and secondary vertices, respectively.

Since the detector resolution is finite, the uncertainty in the primary and secondary vertices may result in negative decay lengths. For the same reason, the momentum

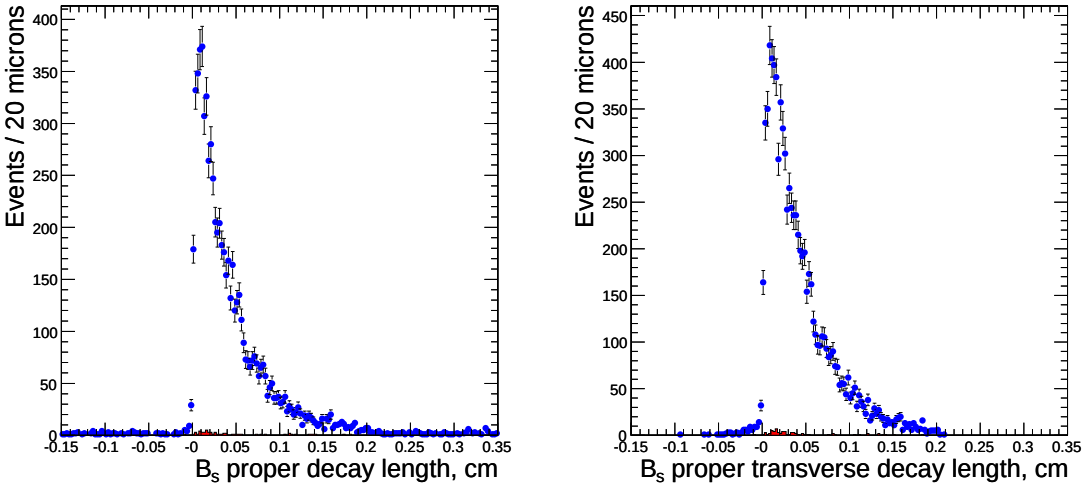

Figure 5.1: The distribution of proper decay length ($c\tau$) of reconstructed B_s^0 candidates: **Left:** in three dimensions, **right:** in the transverse plane. **Blue:** all events, **red:** combinatorial background.

of the B_s^0 may point towards the primary vertex in which case the flight path is counted negative [1].

The proper decay length ($c\tau$ and $c\tau_\perp$) of the B_s^0 meson is calculated multiplying the value of the flight path by a Lorentz factor:

$$c\tau = L/\beta_1\gamma_1 = L\frac{m}{p}, \qquad c\tau_\perp = L_\perp/\beta_2\gamma_2 = L_\perp\frac{m}{p_t} \tag{5.1}$$

where m, p and p_t are the reconstructed mass, momentum and transverse momentum of the B_s^0. The distributions of the proper decay length of the B_s^0 meson, calculated in three dimensions (denoted hereafter as *three dimensional proper decay length distribution*) and transverse plane (denoted hereafter as *transverse proper decay length distribution*) are presented in Fig. 5.1.

It can be seen that the transverse distribution of proper decay length does not contain entries with the decay lengths bigger than 2000 μm. This is due to the cut on the proper decay length of the B_s^0 applied at the generator level for technical reasons[2]. However, the three dimensional distribution has long tails. This can be explained with the presence of the non-Gaussian tails in the distribution of the z-coordinate of reconstructed primary and secondary vertices (see Fig. 4.21 (right) and 4.23 (right) for reference).

[1] This applies equally to the flight paths calculated in three dimensions and in the transverse plane. In the latter case, the direction of transverse momentum of the B_s^0 is compared to the direction of the transverse flight path.

[2] As the presence of the contributions with bigger decay lengths is important for analysis (see below), this cut will be removed in the next data production.

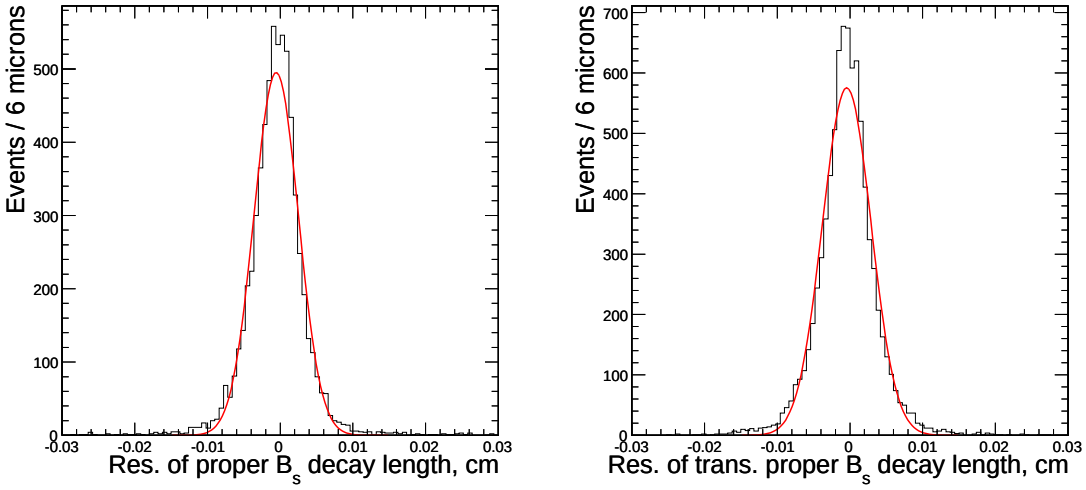

Figure 5.2: Distributions of residuals of reconstructed proper decay length ($c\tau$) of the B_s^0 meson: **left:** in three dimensions, **right:** in the transverse plane.

In Fig. 5.2 the distributions of residuals of the proper decay length of the reconstructed B_s^0 candidates associated with the simulated B_s^0 mesons are presented. The distributions are fitted with the Gaussian function, yielding a standard deviations of approximately 30 μm for the three dimensional distribution and 33.6 μm for the transverse distribution. These values correspond to the resolutions on the proper lifetime τ of approximately 102 fs and 112 fs respectively.

A mentioned in the Ch. 3, the present lower limit of the frequency of the B_s^0 oscillation is 14.4 ps^{-1} [6]. In the case the actual frequency is close to this limit, the period of oscillation correspond to the proper flight path of approximately $L^{\mathrm{pr}} = 130\mu$m. It can be therefore concluded that in this case the $B_s^0 - \bar{B}_s^0$ oscillations could be observed directly with the CMS detector. However, as mentioned in Sec. 1.2, the recent experimental results [7] show that the oscillation frequency is much higher: around 125 ps^{-1} [3]. In this case the direct observation of the $B_s^0 - \bar{B}_s^0$ oscillations will not be possible at CMS.

The distributions of pulls of the proper decay length of the B_s^0 candidates associated with the simulated B_s^0 mesons are presented in Fig. 5.3. The distributions of pulls are fitted with Gaussian function, yielding standard deviations of 1.354 for three dimensional and 1.236 for the transverse distributions respectively, indicating that errors are underestimated. This is mainly due to the errors on the reconstructed mass and coordinates of the secondary vertex, which are used (c.f. Sec. 3.5).

[3] As mentioned in Sec. 1.2, this measurement suffers from large uncertainties and should be reconfirmed with higher statistics and possibly other measurements.

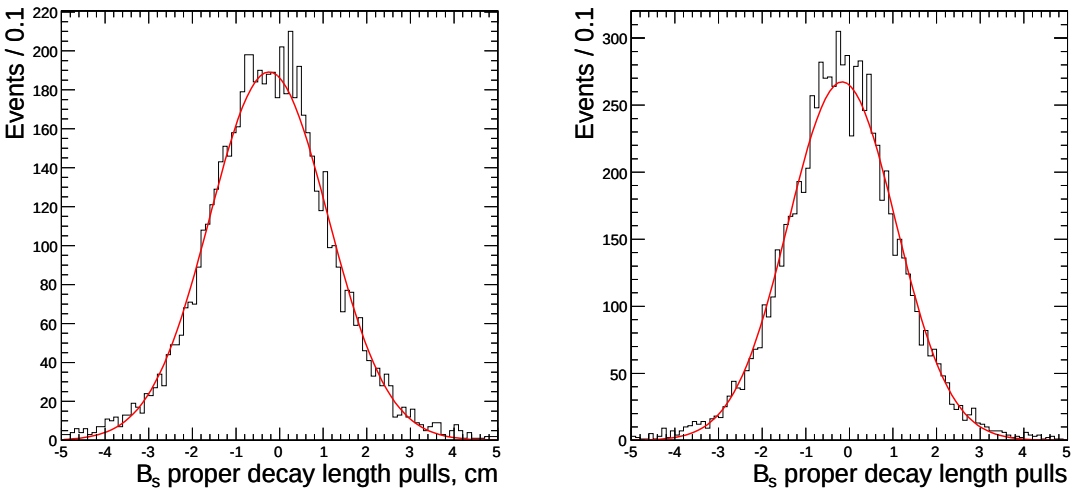

Figure 5.3: Distributions of pulls of reconstructed proper decay length ($c\tau$) of the B_s^0 meson: **left:** in three dimensions, **right:** in the transverse plane.

5.2 The Likelihood analysis

To estimate the possibility of the measurement of the proper decay length of the B_s^0 meson, a likelihood fit [14] of the distributions of the proper decay length was performed. Both binned and unbinned likelihood fits were performed.

The probability density functions (p.d.f.) used for the likelihood analysis are presented in the Appendix B. Two different p.d.f., aimed to model experimental distributions of proper decay length were considered:

First, a single exponential function describing the decay of B_s^0 meson, convoluted with a Gaussian p.d.f. describing the detector resolution was used to approximate the decay length distributions (*single exponent fit*). The slope of the exponential decay and the standard deviation of the Gaussian function were taken as free parameters to be determined in the fit.

The single exponent fit does not describe correctly the distributions of the proper decay lengths of the B_s^0 meson. Since the lifetimes of the heavy and light mass eigenstates of the B_s^0 meson are different, the reconstructed distributions should be described with the double exponent fit. In the present Monte Carlo, the lifetime values of $\tau_s^{\mathrm{L}} = 1.330 \cdot 10^{-12}$ s and $\tau_s^{\mathrm{H}} = 1.625 \cdot 10^{-12}$ s were used (see Sec. 4.1) at the generator level. However, the intensity of the B_s^0 decay with longer lifetime is much smaller than the one for shorter lifetime (light mass eigenstate). In the current Monte Carlo data sample these intensities were set to 16% and 84% respectively.

The single exponent fit may therefore provide a broad estimate of experimental resolution and also allows to test the quality of the fit.

At the second stage, the distributions of the proper decay length were described with the p.d.f., representing a sum of two exponentials convoluted with a gaussian function. (*double exponent fit*). The slopes of exponentials, the standard deviation of the Gaussian function and the fraction of decays with longer decay length (heavy mass eigenstate) were taken as free parameters to be estimated during the fit.

The double exponent model describes data more precisely. When analyzing the real data, an expected distribution of the background should be added. Such a distribution represents usually sum of a Gaussian p.d.f., modeling the prompt background and several exponential decays, describing the backgrounds with significant lifetime. In addition, the p.d.f should be convoluted with a calculated acceptance function of selection cuts. Indeed, the significance cut could remove short living events.

In order to ensure the correctness of the fitting procedure and to test the accuracy of measurement of parameters with likelihood fit, a dedicated study using the simplified fully controlled Monte Carlo was performed. Distributions of proper decay length of heavy and light mass eigenstates of B_s^0 meson were generated with lifetimes equal to those used for production of $B_s^0 \to (J/\psi)\phi \to \mu^+\mu^- K^+ K^-$ data sample ($c\tau^{\text{Heavy}} = 487.0$ μm and $c\tau^{\text{Light}} = 398.6$ μm). These distributions were weighted by the expected fractions and convoluted with a Gaussian function modeling the detector resolution. The standard deviation of this Gaussian function was chosen to be 29 μm. The results of both fits and of their application to the reconstructed distributions of proper decay length are presented in next two sections.

5.2.1 Single exponent fit

At the initial stage, the single exponent fit was verified on the special simplified Monte Carlo sample consisting of a single exponential convoluted with the Gaussian p.d.f. Then the single exponent fit was applied to the double exponent simplified Monte Carlo discussed above. An unbinned likelihood fit was performed, taking the slope of the exponential decay and the standard deviation of the Gaussian function as free parameters to be estimated during the fit. The result of such a test performed on statistics of 10′000 events are presented in the Table 5.1.

The value of the standard deviation of the Gaussian is reconstructed correctly without significant bias. However, as can be expected the presence of 16% fraction of long-living component biases significantly the measurement of the proper decay

	Proper decay length $c\tau$ (μm)		Gaussian St. Dev. (μm)
Generated	$c\tau^{\text{Heavy}} = 487.0$	$c\tau^{\text{Light}} = 398.6$	29
Reconstructed	418.221 ± 6.05		28.5 ± 1.5

Table 5.1: Results of the validation study of the single exponent fit.

length. The measured values are constantly shifted by a mean of 5% to 6% with respect to the dominant contribution (short-living component).

At the second stage, the single exponent fit was used to study reconstructed distributions of proper decay length of the B_s^0 meson. The following fits were performed:

- **Binned likelihood fit:** single exponent fit of the binned distributions of proper decay length. A bin size of 25 μm was selected. The slope of the exponential decay and the standard deviation of the Gaussian function were determined during the fit.

- **Unbinned likelihood fit with fixed Gaussian standard deviation:** single exponent fit of the unbinned distributions of proper decay length. The values of the standard deviation of the Gaussian function were fixed to be equal to the resolutions obtained from the distributions of residuals in Sec. 5.1. The slope of the exponential decay was determined during the fit.

- **Unbinned likelihood fit with running Gaussian standard deviation:** single exponent fit of unbinned distributions of proper decay length. The values of the standard deviation of the Gaussian function were taken to be equal to the reconstructed error of each measurement. These errors were scaled with a fixed correction, making the standard deviation of the distribution of pulls to be equal to 1 (c.f. Sec. 5.1).

- **Full unbinned likelihood fit:** single exponent fit of the unbinned distributions of proper decay length. A slope of the exponential decay and a standard deviation of the Gaussian function were determined during the fit.

In Fig. 5.4 an example of binned single exponent fit of the proper decay length distributions is presented. Results of the application of single exponent fit to the distributions of reconstructed proper decay length are summarized in Tab. 5.2 and 5.3. It can be noted that the results of all fits are consistent with each other. The

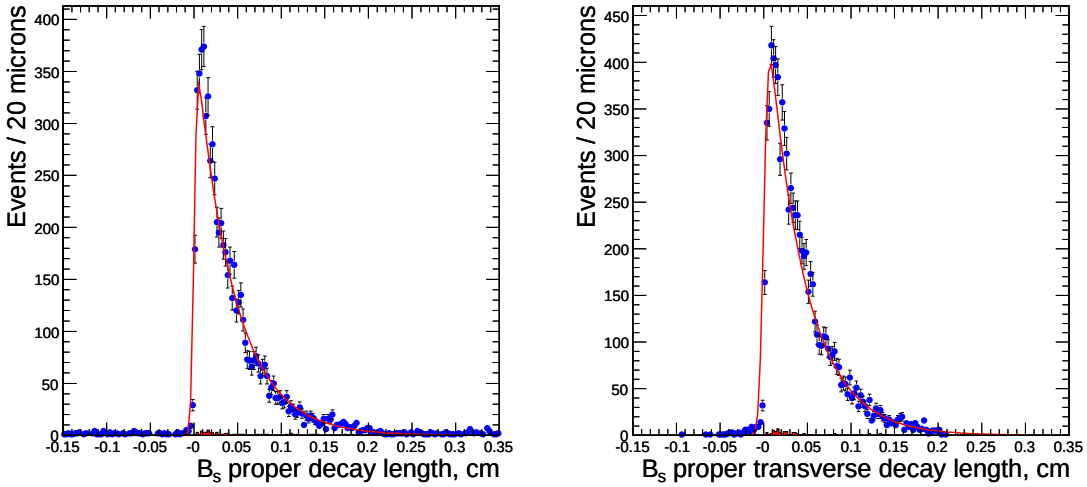

Figure 5.4: Distributions of the proper decay length of the B_s^0 meson (**Left:** in three dimensions, **Right:** in transverse plane), fitted with unbinned likelihood method using the single exponent p.d.f.

estimated values of the proper decay length are 8% to 10% bigger than the decay length of the dominant contribution (light mass eigenstate, $c\tau^{Light} = 398.6$ μm).

In case of three dimensional distribution, estimates of the detector resolution are consistent with measurement presented in the Sec. 5.1. However, for the transverse distribution of the proper decay length, the estimates of detector resolution are shifted by approximately 8 μm toward higher values.

Taking into account results of validation tests and likelihood fits of reconstructed distributions of proper decay length, it can be concluded that the single exponent model does not describe correctly these distributions and more complex model should be used.

5.2.2 Double exponent fit

The validation of the double exponent fit was performed on the same toy-Monte Carlo sample as was used for the single exponent fit. An example of the double exponent fit of the simulated distribution of the proper decay length is presented in Fig. 5.5.

First, the fraction of heavy mass eigenstates was fixed to 16% and, standard deviation of the Gaussian and the values of proper lifetimes of the two mass eigenstates were determined during the fit. In order to include the negative tail of the distribution of the proper decay length, the lower bound of the fit region was selected to

Strategy	$c\tau$ (μm)	σ μm
Binned Likelihood	433.743 ± 5.391	28.499 ± 1.283
Unbinned Likelihood (σ fixed)	433.670 ± 8.750	30.6
Unbinned Likelihood (running σ)	432.962 ± 7.617	——
Unbinned Likelihood (full)	433.739 ± 7.644	27.67 ± 1.775

Table 5.2: Results of the single exponent likelihood fit of distribution of the proper decay length of the B_s^0 meson reconstructed in three dimensions. The fit was performed on 6828 events selected in the range -0.015 cm $< c\tau <$ 0.3 cm.

Strategy	$c\tau$ (μm)	σ μm
Binned Likelihood	427.065 ± 2.715	41.863 ± 1.488
Unbinned Likelihood (σ fixed)	427.65 ± 6.739	33.6
Unbinned Likelihood (running σ)	426.079 ± 7.489	——
Unbinned Likelihood (full)	426.925 ± 6.741	41.484 ± 2.087

Table 5.3: Results of the single exponent likelihood fit of distribution of the proper decay length of the B_s^0 meson reconstructed in transverse plane. The fit was performed on 8479 events selected in the range -0.015 cm $< c\tau <$ 0.3 cm.

be -0.01 cm [4]. The upper bound of the fit region was set to 0.3 cm, which allows to include most of events in the positive tail of the distribution. The upper bound of 0.2 cm, corresponding to the technical cut on the generator level (see Sec. 5.1) was also tested. Some of results of this validation study for different statistics are presented in Tab. 5.4 and 5.5.

It can be seen that the proper decay lengths of the components can be estimated with statistics of about 10000 events, however the measurements on this statistics suffer from large uncertainties. The bigger statistics makes this measurement much more precise.

It was also noted that accuracy of estimation of proper decay lengths strongly depends on the data sample selected for analysis. The likelihood is unable to make a correct estimate if a significant fraction of the positive tail of a distribution was not included in the analyzed data sample. The latter can be explained with the fact

[4] In the real data this lower bound is usually selected at 0 μm, since a significant fraction of events in the negative tails is due to the prompt background.

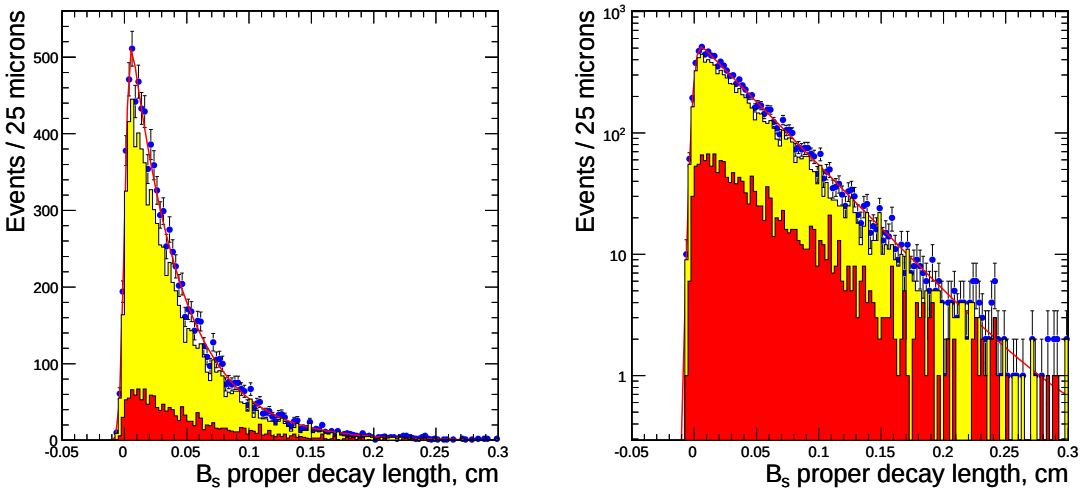

Figure 5.5: The distribution of proper decay length for Monte Carlo validation sample of 10000 events. **In red:** heavy mass eigenstate. **In yellow:** light mass eigenstate. **Blue dots:** both components together. **Red curve:** double exponent fit.

Fit	Interval (N.of Ev.)	$c\tau^{\text{Heavy}}$ (μm)	$c\tau^{\text{Light}}$ (μm)	σ (μm)
Binned	$[-0.015; 0.3]$ (9996)	not determined	414.874 ± 5.074	29.461 ± 10.888
Unbinned	$[-0.015; 0.3]$ (9996)	517.279 ± 99.605	400.024 ± 24.230	28.542 ± 15.142
Unbinned	$[-0.015; 0.2]$ (9911)	416.476 ± 171.384	415.740 ± 34.054	28.544 ± 15.143

Table 5.4: Results of the validation of double exponent fit on the Monte Carlo generated sample of 10000 events.

that the contribution of heavy (long living) component is much bigger in the right tail than the center of the distribution. The right tail should therefore be always included in a data sample to analyze.

Next, the values of proper decay lengths of heavy and light components, and the fraction of the heavy mass eigenstates were determined during the fit. The data samples with statistics up to 10^6 events were tested. It was shown that if the fractions of the the components are to be determined during the fit, there is no sensitivity to any of the parameters. This fact indicates that in the present model the fraction of heavy mass eigenstate are too small to be estimated from the distribution of proper decay length[5]. Since the real values of the fractions of heavy

[5]However, the application of discussed fit is possible if the fraction of heavy mass eigenstates is bigger. For instance, in the non-physical case with 50% contribution of heavy mass eigenstate, the fit returns correct values.

Fit	Interval (N.of Ev.)	$c\tau^{\text{Heavy}}$ (μm)	$c\tau^{\text{Light}}$ (μm)	σ (μm)
Unbinned	$[-0.015; 0.3]$ (99930)	482.926 ± 26.719	398.975 ± 7.425	29.469 ± 0.483
Unbinned	$[-0.015; 0.2]$ (99164)	410.892 ± 60.475	410.728 ± 1.163	29.468 ± 0.483

Table 5.5: Results of the validation of double exponent fit on the Monte Carlo generated sample of 100000 events.

and light mass eigenstates are unknown, the double-exponent fit can not be applied to the real data. The prospects for estimation of these quantities with alternative methods are presented in the next section.

5.3 Prospects for further analysis

As it can be concluded from the previous two sections, the values of proper decay lengths of heavy and light mass eigenstates of the B_s^0 meson and their fractions in $B_s^0 \to (J/\psi)\phi \to \mu^+\mu^- K^+ K^-$ decay can not be estimated from the distribution of the proper decay length. No sensitivity to the these parameters was observed at any statistics.

An alternative method is provided with the likelihood fit of the angular distributions of the final state components. The properties of the angular analysis are briefly discussed in Sec. 1.2.3. A possible set of three angles (ψ, θ, ϕ), suitable for description of the kinematics of the final state is introduced in Appendix B. The general form of the differential decay rate $d\Gamma(t)/d\cos\Theta d\phi d\cos\psi$ is given by the Eq. (A.1).

By integrating over the angles ϕ and $\cos\psi$, the one-angle distribution $d\Gamma(t)/d\cos\Theta$ can be obtained. According to [18], the general form of this distribution is:

$$\frac{d\Gamma(t)}{d\cos\theta} \propto (|A_0(t)|^2 + |A_\parallel(t)|^2)\frac{3}{8}(1+\cos^2\theta) + |A_\perp(t)|^2\frac{3}{4}\sin^2\theta, \qquad (5.2)$$

where $|A_0(t)|^2$, $|A_\parallel(t)|^2$ and $|A_\perp|^2$ are the time evolutions of physical observables, defined in Tab. A.1. For an untagged data sample the time evolution of these physical observables are [18]:

$$\begin{aligned} |A_0(t)|^2 &\propto |A_0(0)|^2 e^{-\Gamma_L t}, \\ |A_\parallel(t)|^2 &\propto |A_\parallel(0)|^2 e^{-\Gamma_L t}, \\ |A_\perp(t)|^2 &\propto |A_\perp(0)|^2 e^{-\Gamma_H t}. \end{aligned}$$

The one-angle distribution (5.2) then simplifies to

$$\frac{d\Gamma(t)}{d\cos\theta} \propto (|A_0(0)|^2 + |A_\parallel(0)|^2)e^{-\Gamma_L t}\frac{3}{8}(1+\cos^2\theta) + |A_\perp(0)|^2 e^{-\Gamma_H t}\frac{3}{4}\sin^2\theta.$$

Being convoluted with the resolution and acceptance functions of angle θ, the latter function can be used as the p.d.f. for a likelihood fit of a reconstructed $d\Gamma(t)/d\cos\theta$ distribution. Since the angular dependencies of heavy and light mass eigenstates in Eq. (5.3) differ significantly, the estimation of their parameters should be possible. The widths and rates of heavy and light mass eigenstates should be then regarded as free parameters to be estimated during the fit.

Conclusion

The prospects of reconstruction and analysis of $B_s^0 \to (J/\psi)\phi \to \mu^+\mu^- K^+ K^-$ events with the CMS detector at LHC detector were studied. The emphasis was given to the reconstruction and fitting techniques suitable for online and offline reconstruction of $B_s^0 \to (J/\psi)\phi$ events.

During the present study a major contribution was made to the development, implementation and testing of the Kalman Filter for vertex reconstruction. Due to its high performance, this algorithm became the base method for the vertex reconstruction in CMS. The resolutions of 44.1 μm and of 53.4 μm were achieved for the transverse and longitudinal coordinates of the primary $B_s^0 \to (J/\psi)\phi$ vertex respectively. The resolutions on transverse and longitudinal coordinates of secondary $B_s^0 \to (J/\psi)\phi$ vertex were found to be 54.8 μm and 73.8 μm respectively.

A kinematic fit and decay chain reconstruction library was developed and implemented in the framework of CMS reconstruction program. This library allows the reconstruction of decay chain from final state to decayed particle according to user-provided decay model. Constrained refit of tracks and vertices is performed via Least Mean Squares minimization with Lagrange multipliers. The possibility of testing physical hypothesis was provided. Due to the application of kinematic constraints, the experimental resolution on the mass of B_s^0 meson improved from 34 MeV to approximately 14 MeV.

Both High Level Trigger (HLT) and offline selection strategies for $B_s^0 \to (J/\psi)\phi \to \mu^+\mu^- K^+ K^-$ decay channel were devised. The rates of the CMS High Level Trigger are estimated as $(3.4 \pm 1.3) \cdot 10^{-2}$ Hz for the signal and $(5.0 \pm 0.7) \cdot 10^{-2}$ Hz for the background events. The HLT signal event yield for 30 fb^{-1} is estimated to be $(5.1 \pm 1.9) \cdot 10^5$.

After the offline selection, some $242'400 \pm 87'400$ signal events would be reconstructed along with the background of $41'600 \pm 18'500$ events. The resolution on the proper decay length ($c\tau$) of the B_s^0 meson is found to be approximately 30 μm. It is concluded that this resolution allows the direct observation of the $B_s^0 - \bar{B}_s^0$ oscillations if the actual oscillation frequency is close to its present lower limit (14.4 ps^{-1}).

Finally, the possibility of measurement of the proper decay lengths of heavy and light mass eigenstates of the B_s^0 meson from the distribution of the proper decay length was studied. The strategy for the maximum likelihood analysis of the distributions of the proper decay length of the B_s^0 meson was developed and tested on the dedicated simplified fully controlled Monte Carlo sample. It was shown that

the efficient reconstruction of proper decay lengths of heavy and light mass eigenstates of the B_s^0 meson is not possible with this method. However, the measurement of these decay lengths is possible from the angular distributions of the final state components. The prospects for this measurement are given.

Appendix A

Differential decay rates for the $B_s^0 \to (J/\psi)\phi \to \mu^+\mu^- K^+ K^-$ samples

The time evolutions of the physical observables $|A_0(t)|^2$, $|A_\parallel(t)|^2$, $A_\perp(t)|^2$, $\Re(A_0^*(t)A_\parallel(t))$, $\Im(A_\parallel^*(t)A_\perp(t))$ and $\Im(A_0^*(t)A_\perp(t))$ is presented in Table A.1 [18]. There δ_1 and δ_2 are the CP conserving strong phases and $\delta\phi = 2\lambda^2\eta$ is the CP-violating weak phase. The rest of the notation is identical to the one used in the Sec. 1.2.

For the initially tagged B_s^0 meson, one obtains the following time dependence of the differential decay rate:

$$\begin{aligned}\frac{d^3\Gamma[B_s^0 \to (J/\psi)\phi \to \mu^+\mu^- K^+K^-]}{d\cos\theta d\varphi d\cos\psi} \propto \frac{9}{32\pi}[2|A_0(t)|^2\cos^2\psi(1-\sin^2\theta\cos^2\varphi) \\ +\sin^2\psi\{|A_\parallel(t)|^2(1-\sin^2\theta\sin^2\varphi)+|A_\perp(t)|^2\sin^2\theta - \Im(A_\parallel^*(t)A_\perp(t))\sin 2\theta\sin\varphi\} \\ +\frac{1}{\sqrt{2}}\sin 2\psi\{\Re(A_0^*(t)A_\parallel(t))\sin^2\theta\sin 2\varphi + \Im(A_0^*(t)A_\perp(t))\sin 2\theta\cos\varphi\}], \qquad \text{(A.1)}\end{aligned}$$

and similarly for the $\bar{B}_s^0 \to (J/\psi)\phi \to \mu^+\mu^- K^+K^-$ decay. Here the variables θ, φ and ψ are the angles describing the kinematics of the final state products, defined as follows [17] (see Fig. A.1):

- The x axis is taken in the direction of flight of ϕ in J/ψ rest frame, the z-axis is perpendicular to the decay plane $\phi \to K^+K^-$ and the y-axis is chosen such that the projection of the momentum of K^+ on it is positive: $p_y(K^+) \geq 0$.

- The coordinates (θ, φ) describe the direction of momentum of μ^+ in the J/ψ rest frame and ψ is the angle made by $p(K^+)$ with the x axis in the ϕ rest frame.

Observable	Time Evolution
$\|A_0(t)\|^2 =$	$\|A_0(0)\|^2 \left[e^{-\Gamma_L t} - e^{\bar{\Gamma} t} \sin(\Delta m t)\delta\phi\right]$
$\|A_\parallel(t)\|^2 =$	$\|A_\parallel(0)\|^2 \left[e^{-\Gamma_L t} - e^{\bar{\Gamma} t} \sin(\Delta m t)\delta\phi\right]$
$\|A_\perp(t)\|^2 =$	$\|A_\perp(0)\|^2 \left[e^{-\Gamma_H t} - e^{\bar{\Gamma} t} \sin(\Delta m t)\delta\phi\right]$
$\Re(A_0^*(t)A_\parallel(t)) =$	$\|A_0(0)\|\|A_\parallel(0)\| \cos(\delta_2 - \delta_1) \left[e^{-\Gamma_L t} - e^{-\bar{\Gamma} t} \sin(\Delta m t)\delta\phi\right]$
$\Im(A_\parallel^*(t)A_\perp(t)) =$	$\|A_\parallel(0)\|\|A_\perp(0)\| \left[e^{-\bar{\Gamma} t} \sin(\delta_1 - \Delta m t) + \frac{1}{2}\left(e^{-\Gamma_H t} - e^{-\Gamma_L t}\right) \cos(\delta_1)\delta\phi\right]$
$\Im(A_0^*(t)A_\perp(t)) =$	$\|A_0(0)\|\|A_\perp(0)\| \left[e^{-\bar{\Gamma} t} \sin(\delta_2 - \Delta m t) + \frac{1}{2}\left(e^{-\Gamma_H t} - e^{-\Gamma_L t}\right) \cos(\delta_2)\delta\phi\right]$

Table A.1: Time evolution of the decay $B_s^0 \to (J/\psi)\phi \to \mu^+\mu^- K^+K^-$ of an initially pure B_s^0 meson.

In case of the untagged decay, the time dependence of the differential decay rate for $f = (J/\psi)\phi \to \mu^+\mu^- K^+K^-$ reads:

$$\begin{aligned}
\frac{d^3\Gamma[f(t)]}{d\cos\theta d\varphi d\cos\psi} \propto \frac{9}{32\pi}[2|A_0(0)|^2 e^{-\Gamma_L t}\cos^2\psi(1-\sin^2\theta\cos^2\varphi) \\
+\sin^2\psi\{|A_\parallel(0)|^2 e^{-\Gamma_L t}(1-\sin^2\theta\sin^2\varphi) + |A_\perp(0)|^2 e^{-\Gamma_H t}\sin^2\theta\} \\
+\frac{1}{\sqrt{2}}\sin 2\psi\{|A_0(0)||A_\parallel(0)|\cos(\delta_2-\delta_1)e^{-\Gamma_L t}\sin^2\theta\sin 2\varphi\} \\
+\{\frac{1}{\sqrt{2}}|A_0(0)||A_\perp(0)|\cos\delta_2\sin 2\psi\sin 2\theta\cos\varphi - |A_\parallel(0)||A_\perp(0)|\cos\delta_1\sin^2\psi\sin 2\theta\sin\varphi\} \\
\times\frac{1}{2}(e^{-\Gamma_H t} - e^{-\Gamma_L t})\delta\phi]. \qquad \text{(A.2)}
\end{aligned}$$

It can be noted that both tagged and untagged differential decay rates provide a possibility to extract Γ_H, Γ_L and $\bar{\Gamma}$, while the extraction of Δm_s always requires tagging. In both cases, the Wolfenstein parameter η is contained in the measurable CP-violating weak phase $\delta\phi = 2\lambda^2\eta$, which is introduced through interference between $B_s^0 - \bar{B}_s^0$ mixing and decay processes. Notably, in case of the tagged decay rate, the weak phase is contained inside the time dependence of the observables (1.19), while in the untagged case, the last term of the decay rate (A.2) is simply proportional to $\delta\phi$:

$$\propto \frac{1}{2}(e^{-\Gamma_H t} - e^{-\Gamma_L t})\delta\phi. \qquad \text{(A.3)}$$

In case of the B_s^0 system, the difference between the widths of the heavy and light mass eigenstates Γ_H and Γ_L is expected to be $\mathcal{O}(20\ \%)$. Consequently, one may expect to observe the effect of mixing-induced CP violation, studying the time evolution of the untagged decay rate in the $B_s^0 \to (J/\psi)\phi \to \mu^+\mu^- K^+K^-$ decay channel.

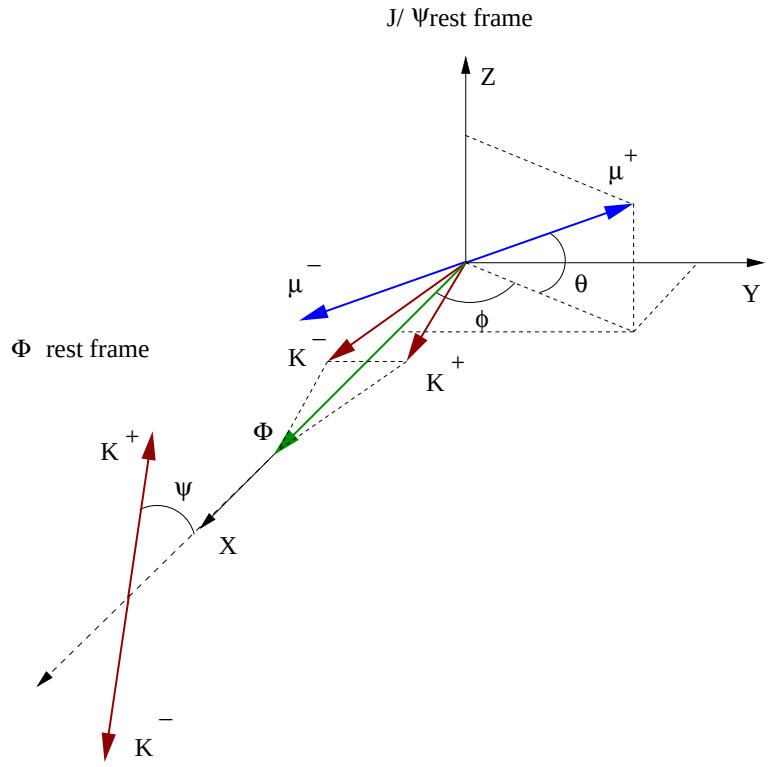

Figure A.1: Definition of the angles, describing the kinematics of the final state particles in the $B_s^0 \to (J/\psi)\phi \to \mu^+\mu^- K^+ K^-$ decay.

Appendix B

Likelihood functions for the B_s^0 lifetime distribution

While distribution of the lifetime is indeed described by an exponential law, the observed distribution is smeared by the resolution of the detector. The resolution of the detector can be described by a Gaussian distribution and the measured distribution of the lifetime is obtained by convoluting the exponential with this Gaussian. The single exponential lifetime distribution convoluted with the gaussian detector resolution results in the following probability density function:

$$\begin{aligned}\mathbf{p.d.f.}^{\text{single}}(\lambda,\sigma;t) &= \int_0^\infty \frac{\lambda}{\sigma\sqrt{2\pi}} e^{-\lambda x} e^{-\frac{(t-x)^2}{2\sigma^2}} dx \\ &= \frac{\lambda}{2} e^{-t\lambda} e^{\frac{(\lambda\sigma)^2}{2}} \left\{ 1 + \text{Erf}\left[\frac{t}{\sigma\sqrt{2}} - \frac{\lambda\sigma}{\sqrt{2}} \right] \right\}, \end{aligned} \tag{B.1}$$

where λ and σ represent the decay slope and the detector resolution respectively, t is the lifetime (can be negative due to the detector resolution), and $\text{Erf}(x)$ is a tabulated error function, defined as:

$$\text{Erf}(x) = \frac{2}{\sqrt{\pi}} \int_0^x e^{-z^2} dz. \tag{B.2}$$

As measured proper lifetimes are usually restricted, the p.d.f. has to be normalized in the interval between lower and upper bounds of the measurement $[t^{\min}, t^{\max}]$:

$$\mathbf{p.d.f.}^{\text{single}}_{\text{NORM}}(\lambda,\sigma;t) = \frac{\mathbf{p.d.f.}^{\text{single}}(\lambda,\sigma;t)}{\int_{t^{\min}}^{t^{\max}} \mathbf{p.d.f.}^{\text{single}}(\lambda,\sigma;t) dt}. \tag{B.3}$$

In case two decays with the same final state and significantly different lifetimes (for instance, $B_s^{0\ \text{Heavy}}$ and $B_s^{0\ \text{Light}}$ decays) are present in the selected sample, a sum

of two exponential decays, convoluted with a gaussian detector resolution can be used as p.d.f.:

$$\mathbf{p.d.f.}^{\text{double}}(\lambda_1, \lambda_2, \sigma; t) = \int_0^\infty \frac{1}{\sigma\sqrt{2\pi}}(\lambda_1 e^{-\lambda_1 x} + \lambda_2 e^{-\lambda_2 x}) e^{-\frac{(t-x)^2}{2\sigma^2}} dx. \tag{B.4}$$

Here λ_1 and λ_2 denote the decay slopes, and σ is the resolution of the detector. The calculation of this integral is fully analogous to the (B.1), however the normalization requires more care. The integral (B.4) factorizes in two parts, corresponding to two independent decays with different lifetimes:

$$\mathbf{p.d.f.}^{\text{double}}(\lambda_1, \lambda_2, \sigma; t) = \mathbf{p.d.f.}_1^{\text{single}}(\lambda_1, \sigma; t) + \mathbf{p.d.f.}_2^{\text{single}}(\lambda_2, \sigma; t),$$

and the normalized joint p.d.f. then reads:

$$\begin{aligned} &\mathbf{p.d.f.}_{NORM}^{\text{double}}(\lambda_1, \lambda_2, \sigma; t) \\ &\quad = \frac{A_1 \cdot \mathbf{p.d.f.}_1^{\text{single}}(\lambda_1, \sigma; t) + (1 - A_1) \cdot \mathbf{p.d.f.}_2^{\text{single}}(\lambda_2, \sigma; t)}{A_1 \cdot \int_{t^{\min}}^{t^{\max}} \mathbf{p.d.f.}_1^{\text{single}}(\lambda_1, \sigma; t)dt + (1 - A_1) \cdot \int_{t^{\min}}^{t^{\max}} \mathbf{p.d.f.}_2^{\text{single}}(\lambda_2, \sigma; t)dt} \end{aligned} \tag{B.5}$$

where A_1 is a relative fraction of decays with lifetimes $\frac{1}{\lambda_1}$. In case a significant background level is expected, the estimated distributions of the background events should be added to the probability density functions (B.1) and (B.4).

Appendix C

Event display of the $B_s^0 \to (J/\psi)\phi \to \mu^+\mu^- K^+ K^-$ sample

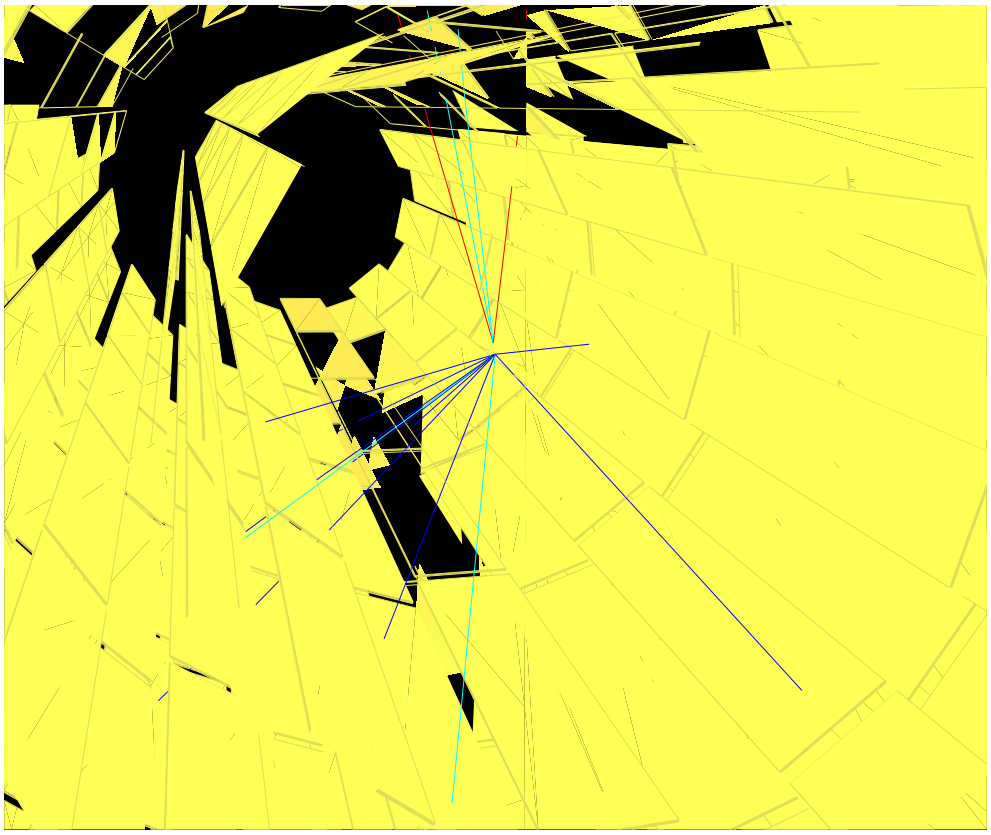

Figure C.1: Typical layout of the $B_s^0 \to (J/\psi)\phi \to \mu^+\mu^- K^+ K^-$ signal event in the CMS detector. **In yellow:** the inner surface of the CMS Pixel detector. **Red trajectories:** signal muons. **Blue-green trajectories:** signal kaons. **Other trajectories:** hadrons, following the fragmentation of the second b-quark.

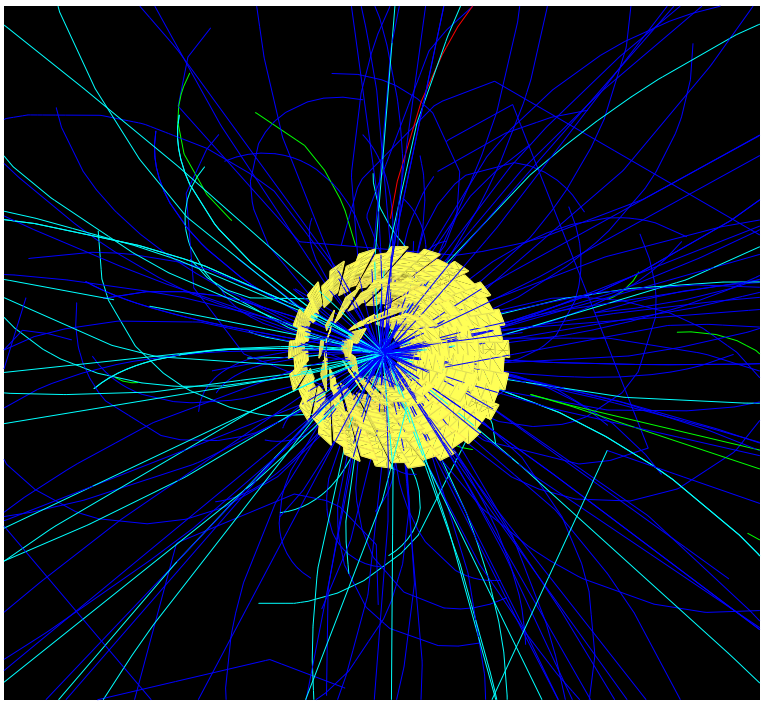

Figure C.2: Typical layout of the $B_s^0 \to (J/\psi)\phi \to \mu^+\mu^- K^+ K^-$ event superimposed with several pile-up events in the CMS detector (transverse view). **In yellow:** the barrel part of the CMS Pixel detector.

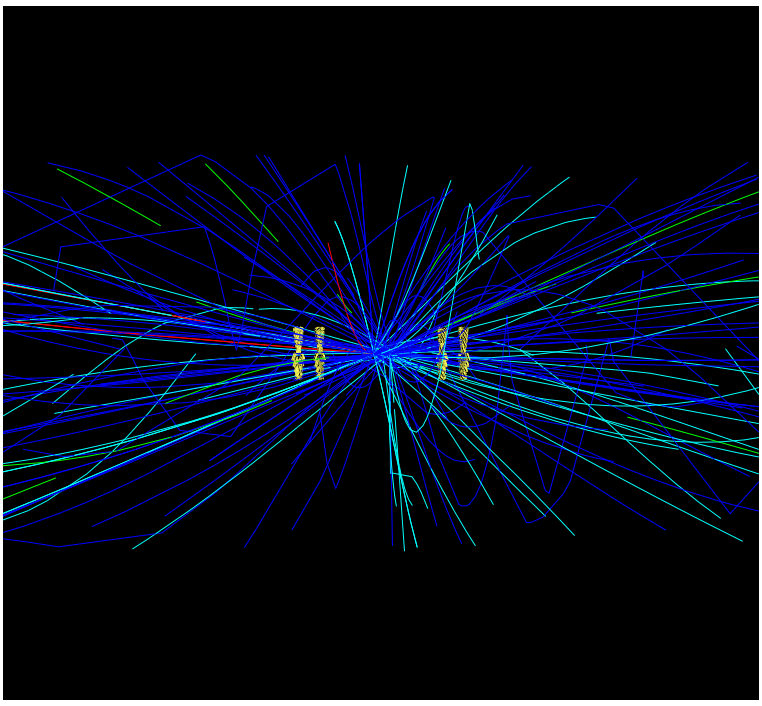

Figure C.3: Same as in Fig. C.2 (longitudinal view). **In yellow:** the end caps of the CMS Pixel detector.

References

[1] G. Altarelli, G. Parisi, "Asymptotic freedom in parton language," *Nucl. Phys. B* **126** (1977) 298.

[2] S. Alekhin et al., "QCD," in *Proceedings of the Workshop on Standard Model Physics (and more) at the LHC*, CERN 2000-004. 2000.

[3] J. Baines et al., "B Production," in *Proceedings of the Workshop on Standard Model Physics (and more) at the LHC*, CERN 2000-004. 2000.

[4] B.L. Combridge, "Associated production of heavy flavour states in pp and $p\bar{p}$ interactions: some QCD Estimates," *Nucl. Phys. B* **151** (1979) 429.

[5] J. Baines et al., "B Decays," in *Proceedings of the Workshop on Standard Model Physics (and more) at the LHC*, CERN 2000-004. 2000.

[6] Particle Data Group, "$B^0 - \bar{B}^0$ Mixing," *Phys. Lett. B* **592** (2004), no. 1-4, 762.

[7] CDF Collaboration, "Time-Dependent Analysis of $B_s \to J/\psi\phi$ and $B_d \to J/\psi K^{*0}$ Decays and a Lifetime Difference in the B_s System." **URL:** *http://www-cdf.fnal.gov/physics/new/bottom/040708.blessed-dgog-bsjpsiphi*, 2004. CDF Note 7115.

[8] M. Kobayashi, T. Maskawa, "CP-Violation in the Renormalizable Theory of Weak Interaction," *Prog. Theor. Phys.* **49** (1973), no. 2, 652.

[9] Particle Data Group, "The Cabibbo-Cobayashi-Moskawa Quark-Mixing Matrix," *Phys. Lett. B* **592** (2004), no. 1-4, 130.

[10] L. Wolfenstein, "Parametrization of the Kobayashi-Maskawa Matrix," *Phys. Rev. Lett.* **51** (1983), no. 21, 1945.

[11] Cecilia Jarlskog and Raymond Stora, "Unitarity Polygons and CP-Violation Areas and Phases in the Standard Electroweak Model," *Phys. Lett. B* **208** (1988), no. 2, 268.

[12] J. Charles et al. (CKMfitter working group). **URL:** *http://www.slac.stanford.edu/xorg/ckmfitter/ckm_results_ichep04.html*, 2004. Presented at ICHEP 2004, Beijing.

[13] A.J. Buras and M. Linder, *Heavy Flavours II*. World Scientific Publishing, 1998.

[14] A.G. Frodesen, O. Skjeggestad and H. Tøfte, *Probability and Statistics in Particle Physics*. Universitetsforlaget, 1979.

[15] I. Dunietz, "$B_s - \bar{B}_s$ mixing, CP violation, and extraction of CKM phases from untagged B_s data samples," *Phys. Rev. D* **52** (1995), no. 5, 3048.

[16] R. Fleischer, I. Dunietz, "CP violation and CKM phases from angular distributions for B_s decays into admixtures of CP eigenstates," *Phys. Rev. D* **55** (1997), no. 1, 259.

[17] A.S. Dighe et al., "Angular distributions and lifetime differences in $B_s \to J/\psi\phi$ decays," *Phys. Lett. B* **369** (1996) 144.

[18] A. Dighe, I. Dunietz, R. Fleischer, "Extracting CKM phases and $B_s - \bar{B}_s$ mixing parameters from angular distributions of non-leptonic B decays," *Eur. Phys. J. C* **6** (1999) 648.

[19] LHC Collaboration , "LHC Design Report." **URL:** *http://ab-div.web.cern.ch/ab-div/Publications/LHC-DesignReport.html*.

[20] *CMS Technical proposal*. 2004. CERN-LHCC-94-38; LHCC-P-1.

[21] *ATLAS Technical Proposal*. 2004. CERN/LHCC/94-43;LHCC/P2.

[22] *LHCB Technical Proposal*. 1998. CERN/LHCC 98-4.

[23] *Total Cross Section, Elastic Scattering and Diffractive Dissociation at the LHC* . 1999. CERN/LHCC 99-7.

[24] *ALICE Technical Proposal*. 1995. CERN/LHCC 95-71.

[25] *CMS TDR 6.1: The Trigger and Data Acquisition project, Volume I. The Level-1 Trigger*. 2000. CERN/LHCC 2000-038.

[26] F. Abe et al. (CDF Collaboration), "Evidence for top quark production in $\bar{p}p$ collisions at $\sqrt{s} = 1.8$ TeV," *Phys. Rev. D.* **50** (1994), no. 5, 2966.

[27] S. Abachi et al. (D0 Collaboration), "Observation of the Top Quark," *Phys. Rev. Lett.* **74** (1995), no. 14, 2632.

[28] *CMS Tracker Technical Design Report*. 1998. CERN/LHCC 98-6.

[29] *Addendum to the CMS Tracker TDR by the CMS Collaboration*. 2002. CERN/LHCC 2000-016.

[30] *CMS ECAL Technical Design Report*. 1997. CERN/LHCC 97-33.

[31] *CMS HCAL Technical Design Report*. 1997. CERN/LHCC 97-31.

[32] M. Swartz, "A Detailed Simulation of the CMS Pixel Sensor." CMS Note 2002/027, 2002.

[33] A. Dorokhov et al., "Test of silicon sensors for the CMS pixel detector," *Nucl. Instr. and Meth. in Phys. Res. A* **530** (2004) 71.

[34] C. Amsler et al., "A high resolution silicon beam telescope," *Nucl. Instr. and Meth. A* **480** (2002) 501.

[35] Y. Allkofer et al., "Design and performance of the silicon sensors for the CMS barrel pixel detector." Preprint for Elsevier Science in preparation, 2005.

[36] A. Dorokhov, *Performance of Radiation Hard Pixel Sensors for CMS Experiment*. PhD thesis, Physik-Institut Universität Zürich, 2005.

[37] S. Sguazzoni, "The CMS Si-Strip Tracker." CMS CR 2004/060, Presented at ICATPP 2003, Como, October 6-10 2003, 2004.

[38] *CMS Muon Technical Design Report*. 1997. CERN/LHCC 97-32.

[39] S. Lacaprara, "The CMS Muon System: Physics Performance." CMS CR 2003/025, Presented at VI Symposium on LHC Physics and Detectors at Fermilab, 2003.

[40] *CMS TDR 6.2: The Trigger and Data Acquisition project, Volume II. Data Acquisition and High-Level Trigger*. 2000. CERN/LHCC 2000-026.

[41] Particle Data Group, "Meson Particle Listing," *Phys. Lett. B* **592** (2004), no. 1-4, 166.

[42] T. Sjöstrand., "Pythia- the Lund Monte Carlo Event Generator." **URL:** *http://www.thep.lu.se/ torbjorn/Pythia.html*, 2005.

[43] A. Belkov, S. Shulga, "Studies of angular correlations in the decays $B_s^0 \to J/\psi\phi$ by using the SIMUB generator," *Comp. Phys. Comm.* **156** (2004) 221.

[44] S. Abdoulline et al., "An Object-Oriented Simulation Program for CMS," in *Proc. Conf. on Computing in High-Energy Physics CHEP 2004, Interlaken Switzerland*. 2004.

[45] CMS Collaboration, "Object Oriented Simulation for CMS Analysis and Reconstruction.." **URL:** *http://cmsdoc.cern.ch/oscar*, 2005.

[46] S. Agostinelli et al., "Geant4: a simulation toolkit," *Nucl. Instr. and Meth. A* **506** (2003) 250.

[47] CMS Collaboration, "CMS OO Reconstruction." **URL:** *http://cmsdoc.cern.ch/orca/*, 2005.

[48] R. Frühwirth, M. Regler et al., *Data analysis techniques for high-energy physics experiments*. Cambridge University Press, 2000.

[49] W. Adam et al., "Reconstruction of Electrons with the Gaussian-Sum Filter in the CMS Tracker at the LHC." CMS Note 2005/001, 2005.

[50] T. Speer, K. Prokofiev, R. Frühwirth, "Vertex fitting with the Kalman filter formalism in the ORCA reconstruction program." CMS IN 2003/008, 2003.

[51] R. Frühwirth et al., "Vertex reconstruction and track bundling at the LEP collider using robust algorithms," *Comp. Phys. Comm.* **96** (1996) 189.

[52] P. Billoir and S. Qian, "Fast vertex fitting with a local parametrization of tracks," *Nucl.Instr. and Meth. in Phys. Res. A* **311** (1992) 139.

[53] V. Karimäki, "Effective Vertex Fitting." CMS Note 1997/051, 2005.

[54] T. Speer et al., "Vertex Fitting." CMS Note in preparation, 2005.

[55] W. Waltenberger, *Development of Vertex Finding and Vertex Fitting Algorithms for CMS*. PhD thesis, Technischen Universität Wien, 2005.

[56] R. Frühwirth, T. Speer, "A Gaussian Sum Filter for Vertex Reconstruction." CMS IN AN 2003/006, 2003.

[57] P. Avery, "Applied Fitting Theory VI: Formulas for Kinematic Fitting." CBX 98-37; **URL:** *http://www.phys.ufl.edu/ avery/fitting.html*, 1998.

[58] K. Prokofiev, Th. Speer, "A kinematic fit and decay chain reconstruction library." CMS IN 2004/020, 2004.

[59] K. Prokofiev, Th. Speer, "A kinematic fit and a decay chain reconstruction library." Proc. CHEP 2004, Interlaken, Switzerland , 2004.

[60] P. Avery, "Applied Fitting Theory I: General Least Squares Fitting Theory." CBX 98-37; **URL:** *http://www.phys.ufl.edu/ avery/fitting.html*, 1998.

[61] P. Avery, "Applied Fitting Theory VII: Building Virtual Particles." CBX 98-38; **URL:** *http://www.phys.ufl.edu/ avery/fitting.html*, 1998.

[62] N. Magini, *Measurement of $\Delta\Gamma_s$ in the $B_s^0 \to J/\psi\phi$ decay with the CMS detector*. PhD thesis, Univesità degli Studi di Firenze. Dipartimento di Fisica, 2005.

[63] Hai-Yang Cheng, "Hadronic weak decays of heavy mesons and nonfactorization.," *Z. für Physik C* **69** (1996) 647.

[64] A.Belkov, S. Shulga, "Studies of angular correlations in the decays $B_s^0 \to J/\psi\phi$ by using SIMUB generator.," *Comp. Phys. Comm.* **156** (2004) 221.

[65] S. Cucciarelli et al., "Track Parameter Evaluation and Primary Vertex Finding with the Pixel Detector." CMS Note 2003/026, 2003.

[66] S. Cucciarelli et al., "Update on Primary Vertex Finding with Pixel." Presentation given at CMS Vertex Reconstruction meeting at CERN, 2005.